

CONFIGURATION DESIGN AND
OPTIMIZATION OF VTOL UAV USING A
SIMULATION BASED APPROACH

ALEXANDER LIOU, '26

SUBMITTED TO THE
DEPARTMENT OF MECHANICAL AND AEROSPACE ENGINEERING
PRINCETON UNIVERSITY
IN PARTIAL FULFILLMENT OF THE REQUIREMENTS OF
UNDERGRADUATE INDEPENDENT WORK.

FINAL REPORT

APRIL 29, 2025

LUIGI MARTINELLI
AIMEE WISSA
MAE 340D
91 PAGES
ADVISER COPY

© Copyright by Alexander Liou, 2025.
All Rights Reserved

I pledge my honor that this paper represents my own work in accordance
with University regulations.

Alexander Liou

Alexander Liou

Abstract

In this one-semester junior independent work project, a vertical takeoff and landing unmanned aerial vehicle configuration is designed using simulation and modeling software including SUAVE, OpenVSP, XFLR5, OpenAeroStruct, XROTOR, other Python resources, and Siemens NX. The process is organized into three primary phases that cover increasing levels of fidelity in analysis. Beginning with mission requirements, the process led from low fidelity physical modeling for weight and battery capacity estimate to simulation with SUAVE and modeling with OpenVSP, to optimization of design parameters and more. As fidelity increased, off-the-shelf components were analyzed and selected for high efficiency characteristics. A highly iterative and nonlinear approach provided valuable learning experience on the development cycle of an aircraft with unique requirements.

Contents

| | |
|---|-----------|
| Abstract | iii |
| List of Tables | vi |
| List of Figures | vii |
| 1 Introduction | 1 |
| 1.1 Junior Independent Work Project Goals | 1 |
| 1.2 Tool Descriptions | 1 |
| 1.3 Mission Requirements | 2 |
| 1.4 Configurations Explored | 3 |
| 2 VTOL MK2 Iteration 1 | 8 |
| 2.1 Iteration Goals | 8 |
| 2.2 Aircraft Weight Estimation | 8 |
| 2.2.1 Theory: Low Fidelity Physical Modeling for Weight . . | 8 |
| 2.2.2 Theory: Low Fidelity Physical Design Space | 12 |
| 2.2.3 Weight Estimation Results | 13 |
| 2.3 Design Space Diagram | 14 |
| 2.3.1 Theory: Power Balancing for Maneuvers | 14 |
| 2.3.2 Design Space Results | 15 |
| 2.4 First Pass Vehicle Component Sizing | 18 |
| 2.5 SUAVE Basic Implementation | 21 |
| 2.6 SUAVE Results | 24 |
| 2.7 Comparison of Configurations | 24 |
| 3 VTOL MK2 Iteration 2 | 28 |
| 3.1 Iteration Goals | 28 |
| 3.2 Iteration 2 Weight, Battery, and Design Space | 28 |
| 3.3 Iteration 2 SUAVE Analysis | 29 |
| 3.4 Airfoil Selection | 34 |
| 3.4.1 Airfoil Candidates | 34 |
| 3.4.2 XFLR5 and XFOIL Analyses | 34 |
| 3.5 Tail Optimizer | 36 |
| 4 VTOL MK2 Iteration 3 | 38 |
| 4.1 Iteration Goals | 38 |
| 4.2 Weight and Battery Updated Estimate | 38 |
| 4.3 Energy Network Component Selection | 39 |

| | | |
|----------|---|-----------|
| 4.3.1 | Propeller and Motor Selection | 39 |
| 4.3.2 | Battery Selection | 47 |
| 4.4 | SUAVE Optimization and Major Planform Changes | 48 |
| 4.4.1 | Final Tail Configuration | 51 |
| 4.5 | OpenAeroStruct Drag Minimization | 52 |
| 4.6 | Final Configuration SUAVE Results | 54 |
| 4.6.1 | Stability and Center of Mass | 59 |
| 4.6.2 | Iteration Comparison | 62 |
| 5 | VTOL MK2 Mechanical Design | 64 |
| 5.1 | Wing | 64 |
| 5.1.1 | Tiltrotor Mechanism | 65 |
| 5.1.2 | Spar Design | 67 |
| 5.2 | Fuselage | 69 |
| 5.3 | Tail | 71 |
| 5.4 | Control Surfaces | 71 |
| 5.5 | Avionics | 73 |
| 6 | Conclusion | 75 |
| 6.1 | Future Work | 75 |
| A | | 80 |

List of Tables

| | | |
|-----|--|----|
| 1.1 | Aircraft Requirements | 3 |
| 2.1 | Iteration 1 Key Component Parameters | 20 |
| 2.2 | Iteration 1 Key Tail Parameters | 20 |
| 2.3 | Iteration 1 Propeller Parameters | 22 |
| 3.1 | Iteration 2 Weights and Battery Capacity | 29 |
| 3.2 | Airfoil Options | 35 |
| 4.1 | Propeller Speed Approximation | 40 |
| 4.2 | Propeller Selection Table | 45 |
| 4.3 | Motor Selection Table | 46 |
| 4.4 | Iteration 3 Tail Parameters | 52 |
| 4.5 | OpenAeroStruct Twist Distribution | 53 |
| 4.6 | Iteration Aerodynamics Comparison | 62 |
| 5.1 | Ruddervader Deflection Table | 74 |
| 5.2 | Aileron Deflection Table | 74 |

List of Figures

| | | |
|------|---|----|
| 1.1 | Planform Sketches 1 | 5 |
| 1.2 | Planform Sketches 2 | 6 |
| 1.3 | Planform Sketches 3 | 7 |
| 2.1 | Takeoff Weight Estimation V1 | 13 |
| 2.2 | Battery Capacity Estimation V1 | 14 |
| 2.3 | Design Space Diagram V1 | 16 |
| 2.4 | Design Space Diagram V2 | 17 |
| 2.5 | Efficiency of a Wing Example NACA 2412 | 18 |
| 2.6 | Efficiency of a Wing Example Eppler 205 | 19 |
| 2.7 | Tail Volume Coefficients | 20 |
| 2.8 | Iteration 1 Configuration Sketch | 21 |
| 2.9 | Iteration 1 Propeller Geometry | 23 |
| 2.10 | Iteration 1 Aerodynamic Forces | 24 |
| 2.11 | Iteration 1 Aerodynamic Coefficients | 25 |
| 2.12 | Iteration 1 Velocities | 25 |
| 2.13 | Iteration 1 Battery Conditions | 25 |
| 2.14 | Iteration 1 Disc Power Loading | 26 |
| 2.15 | Iteration 1 Electric Motor Performance | 26 |
| 2.16 | Iteration 1 Flight Conditions | 26 |
| 2.17 | Iteration 1 Propeller Performance | 27 |
| 3.1 | Takeoff Weight Estimation V2 | 29 |
| 3.2 | Battery Capacity Estimation V2 | 30 |
| 3.3 | Iteration 2 Aerodynamic Forces | 30 |
| 3.4 | Iteration 2 Aerodynamic Coefficients | 31 |
| 3.5 | Iteration 2 Velocities | 31 |
| 3.6 | Iteration 2 Battery Conditions for Cruise Segment | 32 |
| 3.7 | Iteration 2 Disc Power Loading | 32 |
| 3.8 | Iteration 2 Electric Motor Performance | 33 |
| 3.9 | Iteration 2 Flight Conditions | 33 |
| 3.10 | Iteration 2 Propeller Performance | 34 |
| 3.11 | Airfoil Lift Curves | 35 |
| 3.12 | Airfoil Efficiencies | 36 |
| 3.13 | Tail Lever Arm Drag Minimum | 37 |
| 4.1 | All Motor Efficiencies | 41 |

| | | |
|------|---|----|
| 4.2 | All Motor Torques | 42 |
| 4.3 | Example Propeller Efficiency Plot | 43 |
| 4.4 | Example Propeller Thrust Plot | 44 |
| 4.5 | Example Propeller Power Plot | 44 |
| 4.6 | Motor Cruise Efficiency | 47 |
| 4.7 | XROTOR Model of Selected Propeller | 48 |
| 4.8 | C_L Optimization, Entire Aircraft | 50 |
| 4.9 | C_L Optimization, Wing Only | 50 |
| 4.10 | C_L Optimization, Wing Only refined | 51 |
| 4.11 | Taper Ratio Optimization | 51 |
| 4.12 | Twist Comparison | 53 |
| 4.13 | Optimized Twist Wing | 53 |
| 4.14 | Optimized Twist Wing Side | 54 |
| 4.15 | Iteration 3 Aerodynamic Forces | 55 |
| 4.16 | Iteration 3 Aerodynamic Coefficients | 56 |
| 4.17 | Iteration 3 Velocities | 56 |
| 4.18 | Iteration 3 Battery Conditions for Cruise | 57 |
| 4.19 | Iteration 3 Disc Power Loading | 57 |
| 4.20 | Iteration 3 Electric Motor Performance | 58 |
| 4.21 | Iteration 3 Flight Conditions | 58 |
| 4.22 | Iteration 3 Propeller Performance | 59 |
| 4.23 | Final Configuration Iso View | 59 |
| 4.24 | Final Configuration Side View | 60 |
| 4.25 | Final Configuration Top View | 60 |
| 4.26 | Final Configuration Front View | 60 |
| 4.27 | Stability Plot | 61 |
| 4.28 | OpenVSP Drag Polar | 63 |
| 5.1 | CAD Cruise Configuration | 64 |
| 5.2 | CAD Hover Configuration | 65 |
| 5.3 | CAD Front View | 65 |
| 5.4 | Wing CAD | 66 |
| 5.5 | Fuselage and Wing Junction CAD | 66 |
| 5.6 | Wing Junction CAD | 66 |
| 5.7 | Wing Junction CAD | 66 |
| 5.8 | Tiltrotor Mechanism Hover CAD | 67 |
| 5.9 | Tiltrotor Mechanism Cruise CAD | 68 |
| 5.10 | Tiltrotor Clearance CAD | 68 |
| 5.11 | Spar Design CAD | 69 |
| 5.12 | Wingbox and Boom Clamp CAD | 70 |
| 5.13 | Boom Clamp | 70 |
| 5.14 | Fuselage CAD | 71 |
| 5.15 | Rear Port CAD | 71 |
| 5.16 | Tail Clamp CAD | 72 |

| | | |
|------|---------------------------------|----|
| 5.17 | Tail Top View CAD | 72 |
| 5.18 | Aileron Sizing | 73 |
| 5.19 | Ruddervator Sizing | 73 |
| 5.20 | Aileron Control Servo | 73 |
| 6.1 | BWB Concept | 76 |
| 6.2 | BWB Front | 76 |
| 6.3 | BWB Top | 77 |
| 6.4 | BWB Side | 78 |

Chapter 1

Introduction

1.1 Junior Independent Work Project Goals

During this one-semester Junior Independent work, an original design of a vertical takeoff and landing (VTOL) unmanned aerial vehicle (UAV) was designed through a process of iterative configuration analysis, detailed component sizing and selection, and detailed mechanical design. The emphasis of this project was on learning new tools and procedures for the analysis and low-fidelity optimization of an airframe for a defined mission, with the intent to learn from the design cycle and implement a more complete, higher fidelity cycle during the year-long senior thesis. Furthermore, this project served as a good challenge of practical engineering skills, especially with the added option to complete the build of the UAV. At the beginning of the one-semester project, however, it was quite well understood that there would likely not be enough time to fully complete the build and electronics before the semester ended. Prior work has been conducted to build a 3D-printed UAV by the author, with the aircraft designated as MK1. Thus, the aircraft developed in this project will be referred to as VTOL MK2.

1.2 Tool Descriptions

Throughout this project, various design and analysis tools were employed. For most applications, Python was utilized for plotting and calculations of models derived by hand. Spreadsheets provided a convenient way of storing data from iterative design cycles.

SUAVE, an open-source Python library built by Stanford's Aerodpace Design Lab, is a conceptual aircraft design, analysis, and optimization tool with built-in features that allow users to construct a model of an aircraft and directly analyze them for flight performance and optimize them for desired objectives. SUAVE features an array of aerodynamic analysis tools, with the simplest being a built-in vortex lattice method solver for determining the forces on lifting surfaces. Thus, SUAVE was the primary design tool utilized for

aerodynamic analysis, especially because it does so over the entirety of a user-defined aircraft mission. With the ability to adapt to unconventional designs, SUAVE provides a useful platform from which to base concept designs off of.

In conjunction with SUAVE, NASA's OpenVSP (Vehicle Sketch Pad) interfaces with SUAVE and operates as a standalone software enabling visualization and rapid geometric modeling of aircraft with pre-constructed parametrized components. OpenVSP was used extensively to visualize designs, create baseline configuration concepts, and run individual flight analysis calculations using its internal flow solvers built into VSPAero, included in the package. VSP also features a Python interface that allowed reading and writing an aircraft file directly from SUAVE, which was extremely convenient for lofting bodies for mechanical design. OpenVSP's aerodynamic analysis tools include a parasitic drag calculator, vortex lattice method analysis, and panel method analysis for solving inviscid potential flow around the target geometry.

In addition to these tools, airfoil selection was done using XFLR5, a software that includes a GUI and utilizes XFOIL for direct airfoil analysis. Thus, XFLR5 provided an accessible method of comparing a variety of airfoils with each other for performance. Furthermore, XFLR5 contains a 3D panel method wing analysis tool, which utilizes the aerodynamic lift and drag polar data computed by the XFOIL wrapper to determine the lift distribution on a 3D wing.

Another Python library that was implemented is OpenAeroStruct from MDO Lab at University of Michigan. With a focus on optimization of aerodynamic structures with the capability to factor in structural concerns, OpenAeroStruct was implemented to optimize a single-point design of the aircraft wing to minimize drag.

Finally, Siemens NX was utilized as the primary CAD software of this project, as it has robust project management and is extremely versatile with the modeling tools it has to offer.

1.3 Mission Requirements

This aircraft was designed with a search and rescue mission or intelligence, surveillance, and reconnaissance mission as the driving design goal. Thus, high endurance and range were desired. In order to keep the aircraft within reasonable weight and size constraints, however, the requirements could not be so demanding as a military-grade product. Furthermore, government constraints on UAVs put an altitude constraint of 400 feet on the design. An example mission was imagined, in which the aircraft would survey the entirety of a remote open space preserve, which was determined to be of equivalent size to a park near the author's hometown, El Corte de Madera Creek Open Space Preserve. The UAV payload was then defined as a camera package (visible or infrared) that was allotted 0.5 kg. With an open space for payload, other objects of similar weights, such as an individual first aid kit, are alternative

options. Based on a measurement of the target mission park area on a map, the aircraft would traverse a 2.5 mile by 2.5 mile square area. Assuming compliance with government regulation of a 400 ft altitude, a camera package with a wide 90 degree coverage area would visualize a strip of land approximately 800 ft in width. Thus, 13.2 passes are required to traverse 2.5 miles of strips laid side by side with 2.5 mile lengths. Thus, the total distance traveled by the UAV would be approximately fifteen 2.5 mile passes including a return flight to origin, putting its range at 37.5 miles. Thus, the UAV range was set as 40 miles for a buffer. With little area for a clean takeoff in a wooded area, vertical takeoff and landing was a desired trait, adding a design challenge. As for endurance, it was decided that a longer endurance with lower velocity was a more valuable trait than high speed and low loiter time, as the aircraft would be able to hover near a target location or point of interest, such as a lost individual. Thus, endurance was decided to be 60 minutes, which is a reasonable value for long range radio-controlled UAVs. With the endurance and range requirements, the cruise speed was determined to be 40 miles per hour, or 17.88 meters per second. A turn radius of 28m yields a 10s full circle sustained turn at cruise velocity.

The mission was broken into multiple segments, including a hover and climb segment, forward flight climb segment, cruise segment, descent segment, and a hover descent segment. The initial hover segment was an ascent to 10 meter altitude vertically at 2 meters per second, at which point the aircraft transitions to forward flight. Since the cruise altitude was 400 feet, the climb velocity was determined by a 15 degree climb gradient, resulting in a 4.6 meter per second altitude ascent rate. The descent included a 0.5 meter per second altitude drop to 10 meters, at which transition to hover would be initiated. A 30 second hover followed, and a vertical descent at 2 meters per second finished the mission. A table of aircraft requirements is thus given in Table 1.1 summarizes the overarching aircraft requirements driving design.

Table 1.1: Aircraft Requirements

| | |
|----------------------------|-------|
| Range (m) | 64374 |
| Endurance (s) | 3600 |
| Altitude (ft) | 400 |
| Cruise speed (m/s) | 17.88 |
| Turn Radius, Sustained (m) | 28 |
| Vertical Climb Speed (m/s) | 4.6 |
| Payload Capacity (kg) | 0.5 |

1.4 Configurations Explored

Due to the requirement that the aircraft be able to vertically takeoff and land, hovering with the aircraft longitudinal axis of the aircraft pointing forward or upward is required. These two configuration types may be known as lift-

cruise and tailsitter, respectively. As the name implies, the lift-cruise aircraft lifts vertically and transitions to forward flight without changing pitch angle significantly. The tailsitter orients itself at a 90 degree pitch for hovering in order to vector its thrust downward, and then pitches down to level flight for transition to forward cruise. The advantage of the tailsitter aircraft is that all forward thrust-producing actuators are able to contribute to hover thrust and cruise thrust. With the lift-cruise configuration, rotors would need to tilt or vector their thrust differently in order to be useful in both regimes. Alternatively, dedicated rotors may be used for lift while dedicated propellers produce thrust in cruise. The latter option produces additional drag in the form of unused rotors while in cruise. Whether it be tiltrotor or separate lifting and cruising actuators, the lift-cruise configuration is mechanically more complex than the tailsitter configuration generally speaking. On the other hand, the tailsitter requires a control algorithm to transition through a large stall angle, turning mechanical simplicity into control complexity.

Control simplicity was a significant factor in this one-semester project, as there would not be enough time to fully develop a control system for a complex aircraft. The favored configuration in this project was a three-propeller aircraft with two front tilting propellers used in lift and cruise, and a rear fixed rotor contributing to hover lift only. Figure 1.1 lists this configuration as the first on the page, where two tractor propellers (circles) tilt forward (orange ellipses) to produce thrust in cruise. Servo motors control the angle of the tiltrotors, while the rear circular propeller remains fixed pointing upward and turns off during cruise phase. The conventional configuration that was chosen as the focus of the project combines the control simplicity of a lift-cruise aircraft with the mechanical efficiency of a tiltrotor. As a tricopter with 2 out of 3 propellers contributing to cruise thrust, minimal additional drag is incurred compared to a conventional aircraft. In hover, the tricopter configuration makes control simpler. It should be noted that in hover mode, yaw control is achieved by vectoring the tiltrotors to produce a yawing moment.

For the tailsitter configurations considered, Figures 1.2 and 1.3 show flying wing or blended wing body aircraft which are naturally suitable as tailsitter aircraft due to their overall aspect ratio. These configurations either have four propellers distributed for stability like a quadcopter or two propellers blowing over the wing control surfaces to vector thrust for control in hover. One configuration considered was a ducted fan at the rear with thrust vectoring. With these configurations, higher efficiency was expected, but the control problem becomes much more difficult. With a conventional aircraft, stability margins increase significantly.

Ultimately, the conventional configuration with tricopter motor layout was focused upon during this semester due to its simplicity over a flying wing or blended wing body in terms of control. Since off-the-shelf components are used for this build, more advanced custom control is planned to be implemented as future work for a Senior Thesis project. Early on in the configuration design,

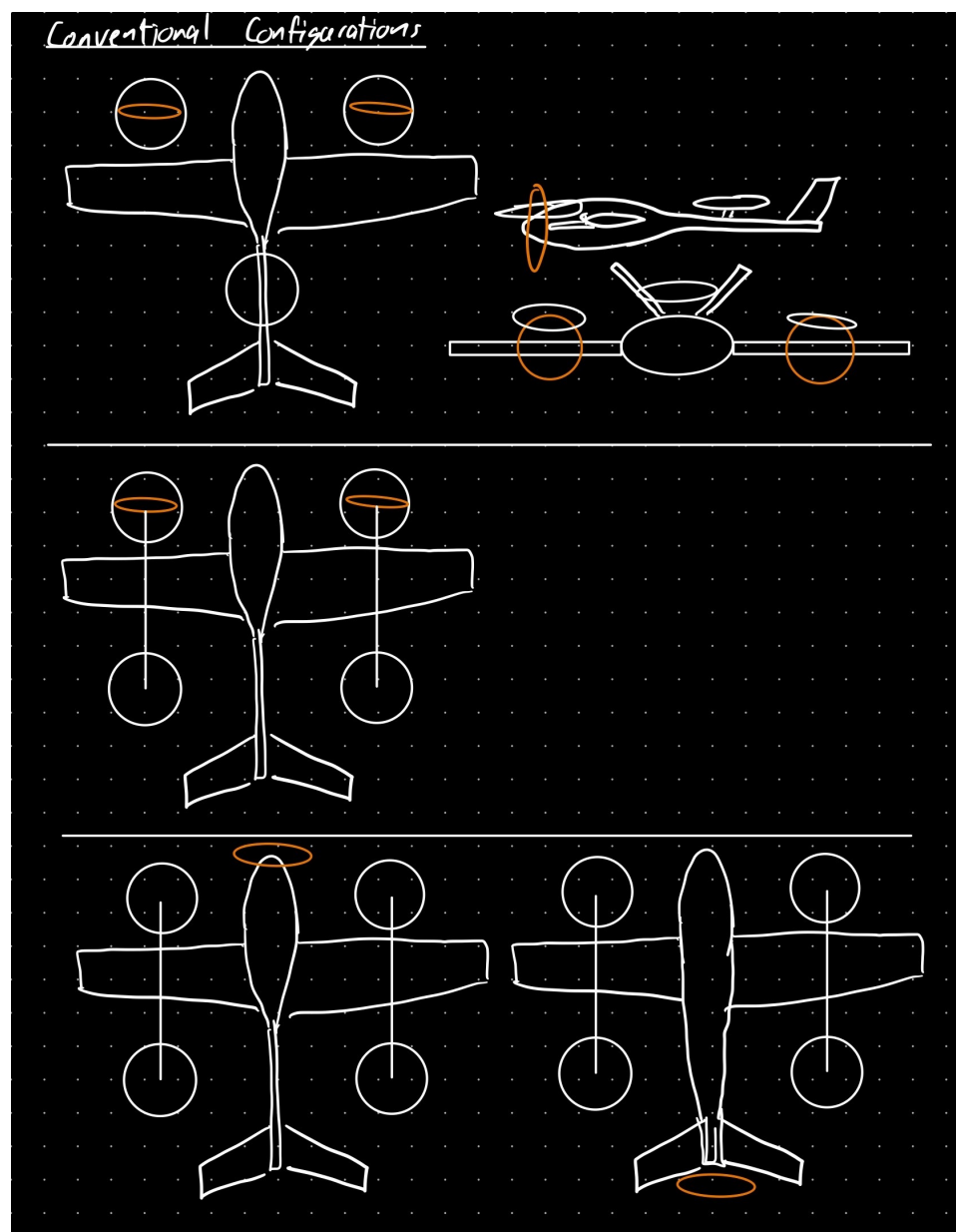


Figure 1.1: Rough Sketch of Conventional Planforms and Propulsion Ideas

a V-tail was selected over a conventional tail due to a lower parasitic drag. Due to the requirement for a rear lift rotor, the fuselage tapers to a thin boom mounting the tail.

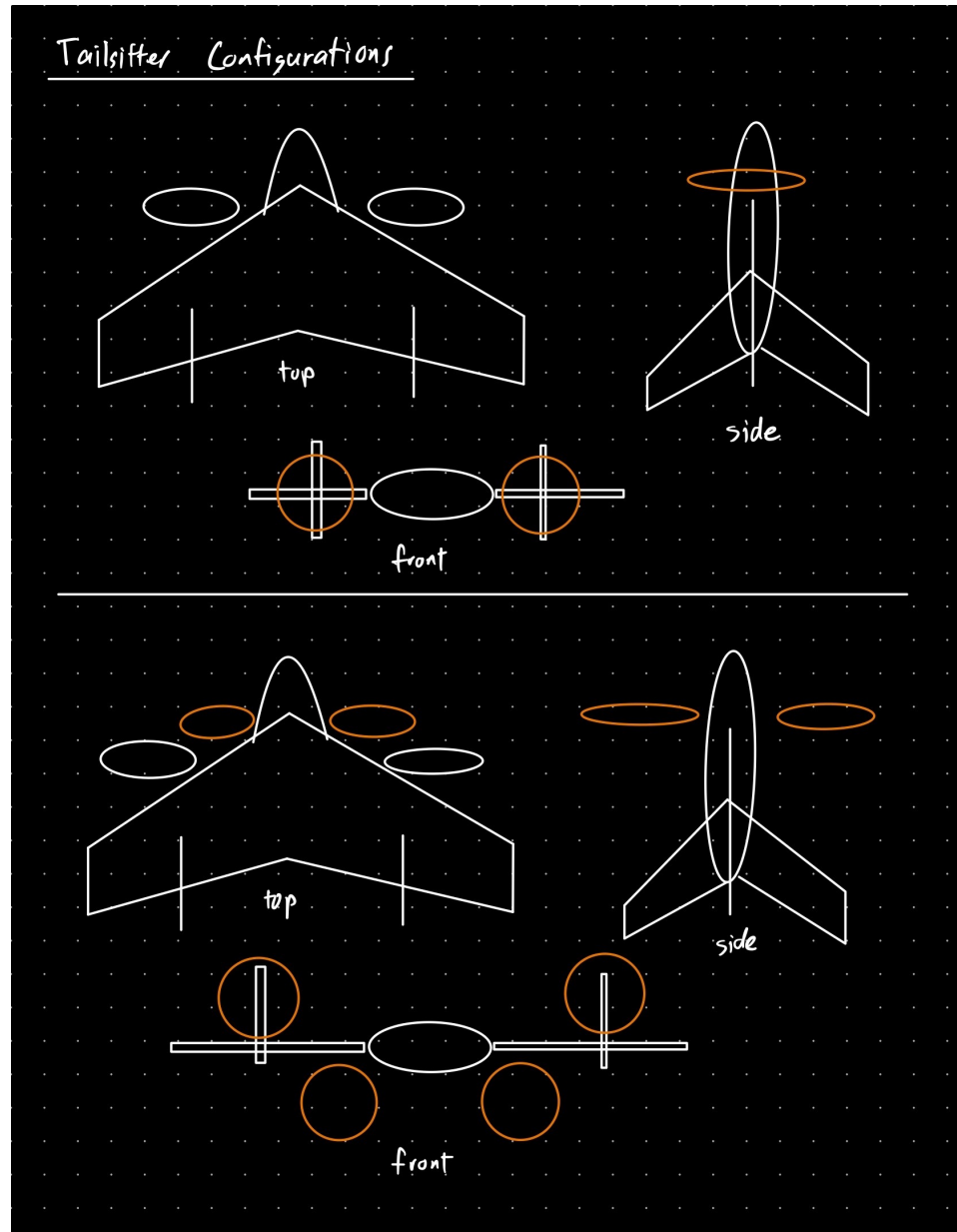


Figure 1.2: Rough Sketch of Tailsitter Planforms and Propulsion Ideas

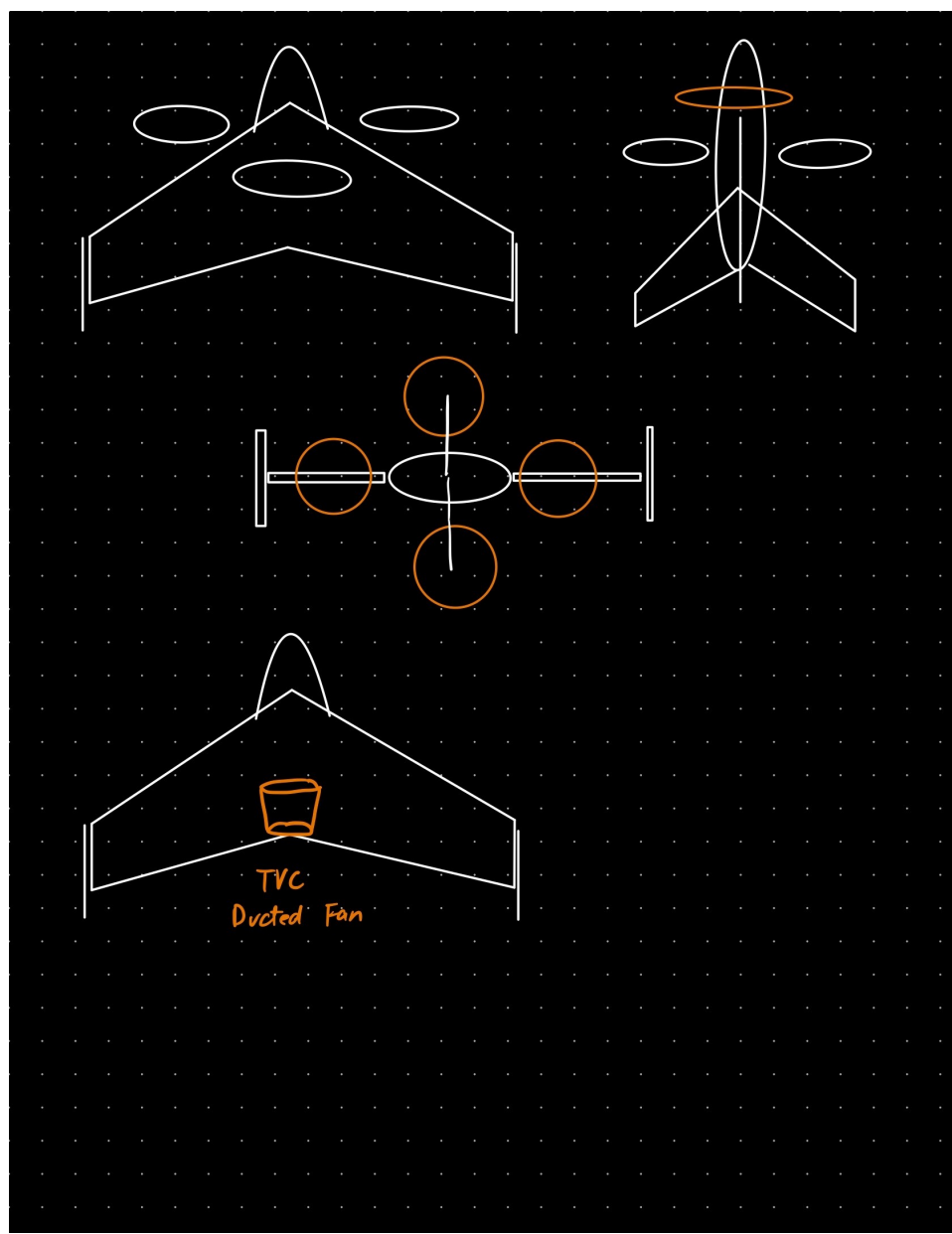


Figure 1.3: Rough Sketch of Additional Tailsitter Planforms and Propulsion Ideas

Chapter 2

VTOL MK2 Iteration 1

2.1 Iteration Goals

In the first aircraft iteration, rough sizing is conducted via low fidelity, simple physical modeling with some empirical approximations based on existing aircraft. The goal is to create a starting point from which analysis will lead to more accurate iterations of aircraft. This method is a quick way to begin configuration design without investing too many resources into high fidelity modeling early on, when designs are extremely fluid.

2.2 Aircraft Weight Estimation

2.2.1 Theory: Low Fidelity Physical Modeling for Weight

The method of battery mass fraction was employed in order to compute the estimated weight of the UAV. This method uses simple point mass dynamics to compute the required battery and aircraft weight iteratively, using physical models and energy or power balancing. Daniel Raymer's *Aircraft Design* specifies some essential equations in its chapter about electric aircraft, some of which were adapted for this project. The first objective is to maximum takeoff weight, W_0 , which is constant at all times for an electric aircraft. W_0 is simply the gravitational constant times the takeoff mass, which is comprised of multiple components:

$$m_0 = m_e + m_b + m_p, \quad (2.2.1)$$

where m_e , m_b , and m_p are empty mass, battery mass, and payload mass, in kilograms, proportional to their weight counterparts W_0 , W_e , and W_p . Equation 2.2.1 can be rearranged as the following:

$$m_0 = m_p + \frac{m_b}{m_0}m_0 + \frac{m_e}{m_0}m_0 \quad (2.2.2)$$

$$m_0 = \frac{m_p}{1 + \frac{m_b}{m_0} + \frac{m_e}{m_0}} \quad (2.2.3)$$

From equation 2.2.3, it is observed that when the payload mass is known, two dimensionless parameters dictate the takeoff weight: empty weight fraction $\frac{m_e}{m_0}$ and battery mass fraction $\frac{m_b}{m_0}$. Battery mass fraction (BMF) is computed for a given set of flight performance requirements that dictate the mission, similar to how fuel weight fraction is a parameter in designing aircraft that use liquid fuel. BMF represents the proportional weight of an aircraft battery to its takeoff weight. The empty weight fraction, on the other hand, is often approximated in the early stages of conceptual design with a semi-empirical curve fit to existing designs of similar characteristics. There exist curve fits for aircraft of different classes, but no existing literature suggested an accurate model for VTOL electric UAV's specifically.

Battery mass fraction for the aircraft mission is the sum of BMF for each mission segment. For the cruise condition, the simple physical model of the definition of energy is utilized:

$$E = \frac{E_{bat}}{P_{used}} = \frac{m_b E_{sb} \eta_s}{P_{used}}, \quad (2.2.4)$$

which states that endurance E (seconds) is equal to the total useful energy available by the battery E_{bat} divided by the power used in cruise P_{used} . The total useful energy of the battery is simply the mass of the battery m_b multiplied by the battery specific energy density E_{sb} multiplied by the efficiency of the entire energy network system, η_s . E_{sb} is a unit measuring the energy of the battery per unit mass of battery. The efficiency of the system comes from the product of the efficiency of the battery to motor shaft η_{b2s} and efficiency of the propeller η_p . For steady state level flight, useful power is simply the mechanical rate of work done by the propeller on the air, and total power used is related via η_p :

$$P_{used} \eta_p = TV = DV = \frac{W_0}{\frac{L}{D}} V = \frac{mg}{\frac{L}{D}} V, \quad (2.2.5)$$

where T is thrust force, which in cruise is equal to drag force D at velocity V . g is the gravitational constant on earth's surface. One might observe that power used is a function of the critical aerodynamic parameter of lift to drag ratio, $\frac{L}{D}$.

Combining equations 2.2.4 and 2.2.5 yields the following equations for endurance in seconds and range R in meters, which are functions of battery mass fraction:

$$E = \frac{L}{D} \frac{E_{sb} \eta_{b2s} \eta_p}{gV} \frac{m_b}{m_0} \quad (2.2.6)$$

$$R = \frac{L}{D} \frac{E_{sb} \eta_{b2s} \eta_p}{g} \frac{m_b}{m_0} \quad (2.2.7)$$

rewritten to solve for BMF:

$$\text{BMF} = \frac{m_b}{m_0} = \frac{EVg}{E_{sb}\eta_{b2s}\eta_p \frac{L}{D}} \quad (2.2.8)$$

For the climb section of the mission, the battery mass fraction was computed with a simple physical model of a point mass. In steady climb, doing a force balance on the aircraft yields $T = D + W_0\sin(\gamma)$, where γ represents climb angle. This can be rearranged into the following, also derived in Daniel Raymer's *Aircraft Design* [4]:

$$\frac{T}{W_0} = \frac{1}{\frac{L}{D_{climb}}} + \frac{V_v}{V}, \quad (2.2.9)$$

where V_v represents vertical velocity. $\frac{V_v}{V}$ is the ratio of vertical to absolute velocity, or simply the Sin of γ . This can be rearranged as the following:

$$V_v = \eta_s \frac{P}{W} - \frac{V}{\frac{L}{D_{climb}}} \quad (2.2.10)$$

From here, the BMF of climb was computed as the required battery energy in terms of battery mass and E_{sb} , where E_{climb} is the total energy required for the climb segment:

$$\text{BMF} = \frac{E_{climb}}{E_{sb}m_0} = \frac{P_{climb}t_{climb}}{E_{sb}\eta_s m_0} = \frac{\Delta h}{V_v} \frac{\frac{P}{W_0}_{climb}g}{\eta_s E_{sb}} \quad (2.2.11)$$

where Δh is the total altitude gain during climb. Furthermore, an approximation provided by aircraft design class for $\frac{L}{D_{climb}}$ was utilized, where $\frac{L}{D_{climb}} = 0.866 \frac{L}{D_{cruise}}$, by empirical curve fitting. Now, the only additional parameter required to compute BMF was the power to weight ratio of climb, $\frac{P}{W_0}_{climb}$, obtained from the design space diagram provided in future sections.

To approximate lift to drag ratio of the aircraft, a parabolic drag polar was assumed, where $C_D = C_{D0} + K_2 C_L^2$, and $K_2 = \frac{1}{\pi e AR}$, derived from the definition of induced drag for a 3 dimensional wing for small angles of attack, in which the lift vector tilts rearward as a result of induced downwash. AR represents the aspect ratio of the wing, defined as span squared over reference area $\frac{b^2}{S}$. Thus, the optimal lift to drag ratio $\frac{L}{D_{max}}$ is obtained by dividing C_L by the polar of C_D , taking the partial with respect to C_L , and setting the expression to 0. Solving this for C_L results in the following:

$$C_{L,max} \frac{L}{D} = \sqrt{\frac{C_{D0}}{K_2}} \quad (2.2.12)$$

$$\frac{L}{D_{max}} = \sqrt{\frac{1}{K_2 C_{D0}}} \quad (2.2.13)$$

When using $\frac{L}{D}$ in the physical models, an empirical correction factor of 0.94 is

applied to obtain a more realistic lift to drag ratio.

Finally, the last major contributor to the battery mass is the hover climb segment of the mission, during which the UAV rises vertically with no forward velocity. From Chapter 21 in Raymer's *Aircraft Design*, rotor momentum theory is useful in deriving the power required to hover. A rotor thrusting air downward with inflow velocity of 0, downwash velocity V_2 , and velocity at the plane of the rotor disk V_1 does work at the rate $P = TV_1 = \dot{m}\Delta VV_1 = \rho V_1^2 S_r V_2$, where S_r is total rotor disk area. Setting this equal to the kinetic energy gain of the flow per unit time results in the following:

$$\rho V_1^2 S_r V_2 = \frac{1}{2} \dot{m} V_2^2 = \frac{1}{2} \rho V_1 S_r V_2^2 \quad (2.2.14)$$

which yields $V_1 = \frac{V_2}{2}$ and $T = 2\rho V_1^2 S_r$, so that

$$V_1 = \sqrt{\frac{T}{2S\rho}} \quad (2.2.15)$$

Then, power in terms of thrust is

$$P = T \sqrt{\frac{T}{2\rho S_r}} \quad (2.2.16)$$

The actual power required includes a factor known as measure of merit, which represents the efficiency of the rotor and ranges from 0.6 to 0.8. Finally, the power required of the battery factors in this measure of merit M and system efficiency η_s

$$P_b = \frac{T}{\eta_s M} \sqrt{\frac{T}{2\rho S_r}} \quad (2.2.17)$$

As for battery mass fraction of the hover segment, the power is simply multiplied by the amount of time hovering and climbing. A modified version of this was implemented, where an added term for potential energy gain is added given a climb velocity V_v :

$$P_b = \frac{W}{\eta_s M} \sqrt{\frac{W}{2\rho S_r}} + W_0 V_v \quad (2.2.18)$$

For the descent and landing phases, it was assumed that BMF would be minimal, as the aircraft could glide down or draw minimal power from the battery upon descent. Thus, landing BMF was left as a minimal value of 0.03 from historical examples. The final BMF was computed as the sum of all mission segment BMF values.

2.2.2 Theory: Low Fidelity Physical Design Space

The battery mass fraction method was implemented in a custom Python script that iteratively guesses takeoff weight W_0 , computes the battery mass fraction for the mission, and then computes an expected takeoff weight based on the following expressions. Equation 2.2.3 is rearranged to show empty weight in terms of battery weight and empty weight fraction:

$$W_0 = \frac{W_b + W_p}{1 - \frac{W_e}{W_0}} \quad (2.2.19)$$

For the first pass, some other similar UAVs were analyzed for their empty weight fractions. Four aircraft, the atomRC Swordfish, Flightory Stallion, OMP ZMO Pro, and Hee Wing T1, featured battery mass fractions which ranged from 0.55 to 0.6. Thus, the first pass weight estimation assumed an empty mass fraction of 0.55.

Furthermore, it can be seen in equation 2.2.13 that parasitic drag coefficient C_{D0} is critical in determining efficiency. Thus, a simple model was created in OpenVSP with the approximate dimensions of a similar off-the-shelf aircraft like those listed above, and the parasitic drag was recorded as 0.023 from OpenVSP's drag calculator. Measure of merit was assumed to be conservatively low, at 0.6.

While these values provide a good first pass starting point for the sizing of the aircraft, the models were updated in further iterations, covered in Chapters 3 and 4. Furthermore, the hover power requirement was initially guessed but then iterated upon based on the results of the next section, where the design space is defined.

The Python script first loops through a range of empty weight fractions and a range of aspect ratios and finally a range of takeoff weight guesses. Each time this triple-nested loop runs, it calls a function to compute takeoff weight. The function then loops over the following procedure: while the iteration number is less than 1000 and the convergence of weight computation is greater than 1%, compute battery mass fraction of the mission, compute W_0 based on equation 2.2.19, and calculate the percent change from the previous value of W_0 , taken as the convergence. Finally, store the value of W_0 to use as the "previous value" for the next loop iteration. At the end of this AR , empty weight fraction, and initial guess datapoint, the function returns the converged value of W_0 . In the loop that called the weight calculation function, the computed value of W_0 that is closest to its initial guess is taken as the data point for a specific aspect ratio and empty weight fraction. The result is a plot that represents the effect of aspect ratio and empty weight fraction (denoted S) on the takeoff weight. Furthermore, battery capacity in milliamp hours was computed based on the battery mass fraction and takeoff weight, yielding a capacity for each weight estimate. The battery capacity was divided by the "useful" proportion, which is approximately 0.75, since for a LiPo battery, 15 to 25% of battery capacity

cannot be used without damaging it.

For details of the script, see "aircraft_weight.py" in the codebase listed in Appendix A. For the first pass approximation of the cruise condition, efficiencies were optimistic, with η_{b2s} being 0.97 and η_p being 0.8 based on the NACA 640 report, which shows optimal propeller design, with peak efficiencies around 0.8. These values were later updated to be more accurate after higher fidelity models were run in iteration 2. In later iterations, it was realized that these efficiencies were much too high, and they were adjusted accordingly.

2.2.3 Weight Estimation Results

The takeoff weight estimation and battery capacity estimation were done through the following plots:

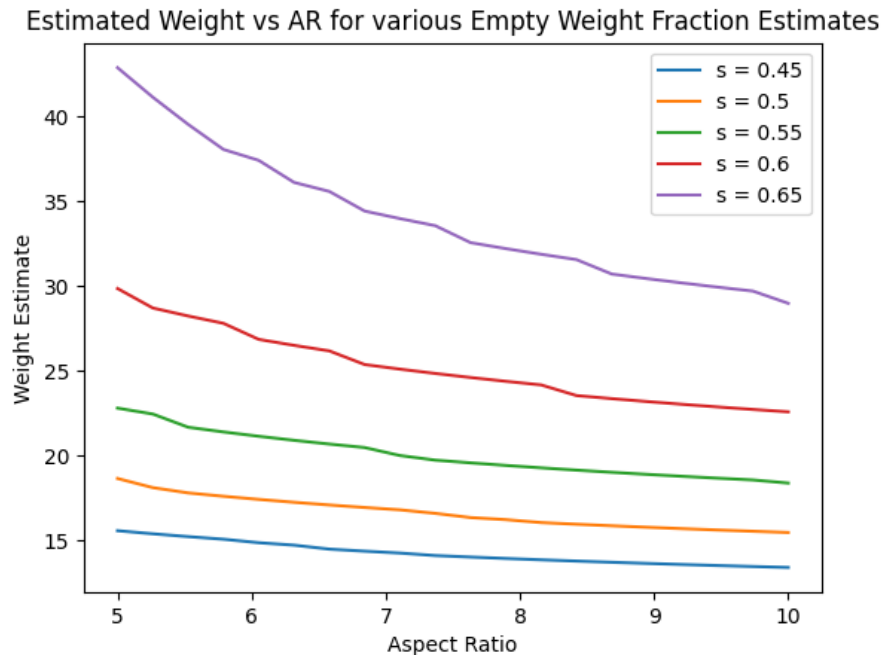


Figure 2.1: Takeoff Weight Estimation vs Aspect Ratio for various Empty Weight Fraction

For the first iteration of the aircraft configuration, it was concluded that an aspect ratio of 6 would be targeted, as this provided a reasonable span for a hand-carried UAV. This justification will be explained in the component sizing section. The empty weight fraction was chosen to be somewhat lenient and err on the side of a heavier airframe. This allows additional weight to be allocated in the design phase to structural components. With an initial value of $S = 0.6$ and an aspect ratio of 6, the first iteration weight estimation is 27 Newtons, or 2.7 kg. The first iteration battery capacity is slightly over 3500 mAh.

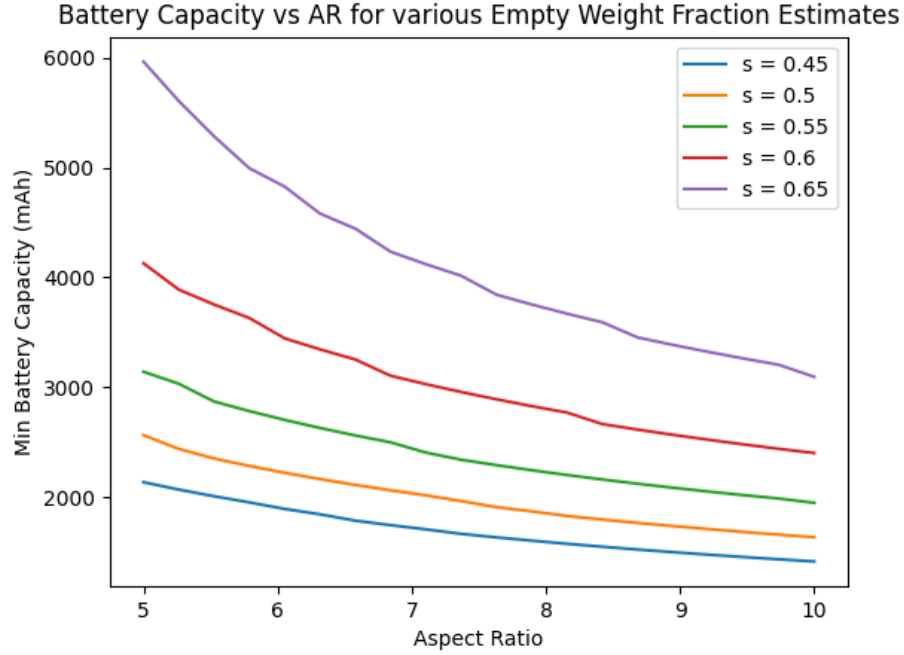


Figure 2.2: Battery Capacity Estimation vs Aspect Ratio for various Empty Weight Fraction

2.3 Design Space Diagram

2.3.1 Theory: Power Balancing for Maneuvers

The design space diagram plots power to weight ratio versus wing loading, and shows curves that bound the design space from maneuvers like steady level flight, sustained turn, hover and climb, and stalling.

The fundamental energy balance behind the design space is that power available by the propellers minus power required to overcome drag (excess power) must be equal to the rate of change in energy of the mechanical system, all normalized by weight W :

$$\frac{P_a}{W} - \frac{P_r}{W} = \frac{d}{dt}\left(h + \frac{V^2}{2g}\right), \quad (2.3.1)$$

where h is altitude. This can be rewritten as the following:

$$\frac{W}{P_a} = \frac{1}{\frac{DV}{W} + \frac{d}{dt}\left(h + \frac{V^2}{2g}\right)} \quad (2.3.2)$$

This is written with a substitute for the parabolic drag polar assumption and $C_L = \frac{nW}{qS}$, where n is the load factor and q is dynamic pressure, such that lift is related to weight by $L = nW$ and $q = \frac{1}{2}\rho V^2$.

$$\frac{W}{P_a} = \frac{1}{\frac{VqS(k_2C_L^2+C_{D0})}{\frac{W}{S}} + \frac{d}{dt}\left(h + \frac{V^2}{2g}\right)} = \frac{1}{\frac{VqS(\frac{1}{\pi eAR}(\frac{nW}{qS})^2+C_{D0})}{\frac{W}{S}} + \frac{d}{dt}\left(h + \frac{V^2}{2g}\right)}$$

(2.3.3)

It is now clear that power loading $\frac{P_a}{W}$ is a function of wing loading $\frac{W}{S}$. For each aircraft maneuver, this equation is altered to produce a curve on the design space restricting aircraft wing loading and setting requirements for power.

Recall that $K_2 = \frac{1}{\pi e A R}$.

For steady level flight, time derivatives go to zero, and the load factor is 1, resulting in the following:

$$\frac{W}{P_a} = \frac{\frac{W}{S}}{Vq(K_2(\frac{W}{S}\frac{1}{q})^2 + C_{D0})} \quad (2.3.4)$$

For a steady climb, vertical climb is included, with $\frac{dh}{dt} = V_v$.

$$\frac{W}{P_a} = \frac{1}{\frac{Vq(K_2(\frac{W}{S}\frac{1}{q})^2 + C_{D0})}{\frac{W}{S}} + \frac{dh}{dt}} \quad (2.3.5)$$

For a constant speed level turn, there is no altitude change, but load factor is that of a perfectly banked turn with no sideslip. For a perfectly banked turn, the load factor is as follows:

$$n = \sqrt{1 + (\frac{V\dot{\psi}}{g})^2} \quad (2.3.6)$$

where $\dot{\psi}$ is the angular velocity of the turn, determined by the radius of turn curvature and velocity $\dot{\psi}R = V$. This is substituted to obtain the power loading for a steady level turn:

$$\frac{W}{P_a} = \frac{\frac{W}{S}}{Vq(K_2(\frac{W}{S}\sqrt{1+(\frac{V\dot{\psi}}{g})^2})^2 + C_{D0})} \quad (2.3.7)$$

The hover and hover-climb power requirement was set by the derivation done in equation 2.2.18. Finally, the stall speed requirement simply limits the wing loading by the lift equation rearranged:

$$\frac{W}{S} = \frac{\rho C_{Lmax} V_{stall}^2}{2} \quad (2.3.8)$$

2.3.2 Design Space Results

Some assumptions were made about the value of the maximum coefficient of lift C_{Lmax} . A stall angle of around 10 degrees was assumed having not known the airfoil that would be used yet. Using the results of thin airfoil theory and

accounting for 3D effects, the lift slope is as follows:

$$C_{L\alpha,3D} = \frac{2\pi}{1 + \frac{2\pi}{\pi e AR}} \quad (2.3.9)$$

yielding a C_{Lmax} of around 0.99 for a 10 degree angle of attack before stalling. Thus, the plot below was produced, with the feasible design space located underneath all maneuver curves and to the left of the stall curve. The stall speed was initially set as 10 meters per second. Choosing a point with the largest wing loading and highest power loading $\frac{W}{P_{req}}$ produces the smallest wing and least power required, lowering the weight of the aircraft. For this reason, a point was chosen at the corner of the design space, with a wing loading of 60 Pascals and power loading of 0.06 N/Watt.

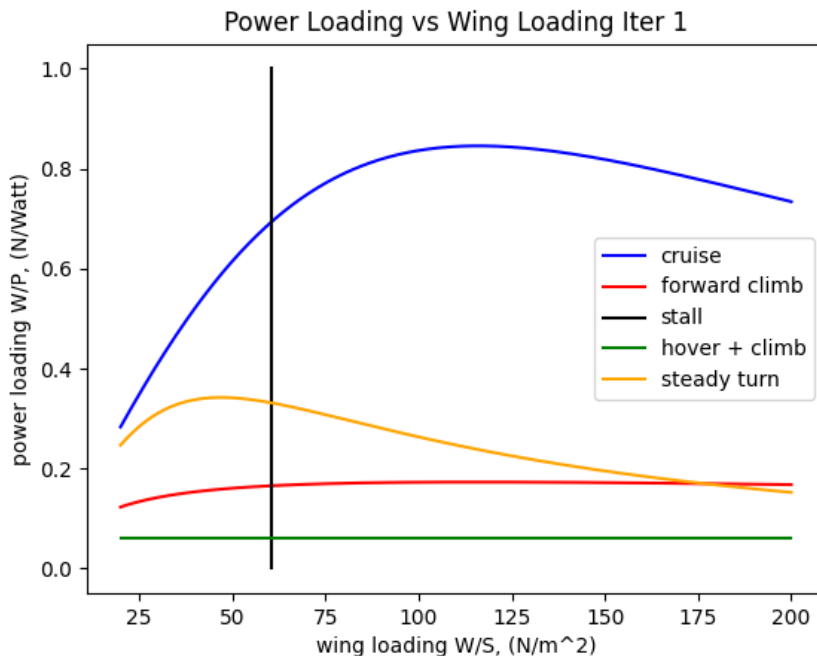


Figure 2.3: Power Loading vs Wing Loading for Iteration 1

It was then decided to add a camber assumption to the airfoil, as this changes the zero-lift angle of attack, yielding a higher C_{Lmax} . C_{Lmax} was determined to be 1.24 for a 10 degree stall and 2.5 degree α_0 for a cambered airfoil similar to those commonly used in this application. This simply changed the wing loading point to 73 Pascals, lowering the reference area of the wing.

With this wing loading and the weight found before, the wing reference area came out as 0.36 square meters, and the C_L was 0.37.

After completing some aircraft iterations using these design parameters and the component sizing methods described below, it was found that the aircraft was operating at a lift coefficient below that of its maximum $\frac{L}{D}$. Thus, the stall requirement was reevaluated. Because the mission dictates that this aircraft takeoff and land vertically, stalling for a landing or takeoff is an extraneous design requirement, as the thrust vectoring for hover can also be used to fly at low speeds. Thus, the stall requirement was ultimately removed, and the

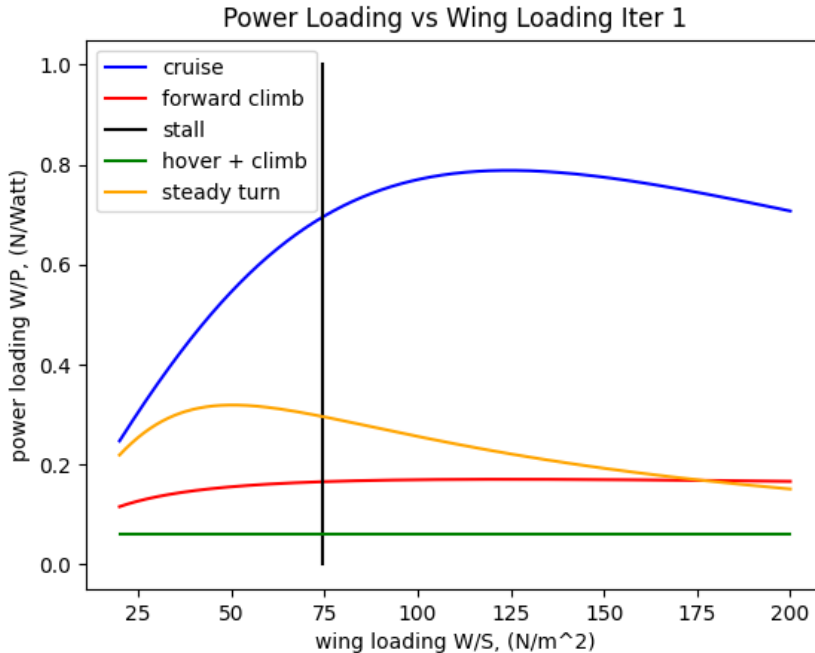


Figure 2.4: Updated Power Loading vs Wing Loading for Iteration 1

wing loading was free to be chosen based on efficiency only. With a parasitic drag coefficient C_{D0} consistently around 0.023, the C_L for maximum $\frac{L}{D}$ is theoretically around 0.7. Running a test wing of similar aspect ratio to the wing being considered in the first iteration yielded a maximum $\frac{L}{D}$ occurring at C_L between 0.4 and 0.5, depending on the airfoil used. Either way, the stall requirement led to operation at a coefficient of lift that was far below the point of maximum efficiency.

To remedy this, OpenVSP was used to test wing configurations to determine the C_L for maximum $\frac{L}{D}$. VSP's panel method was run on a test rectangular wing of aspect ratio 7, a number explained in the next subsection. From these plots, a target of $C_L = 0.4$ was set, as this would yield high efficiency for the first pass iteration, and more detailed airfoil analysis would be completed in later sections. While not at the peak of the curve, a value of 0.4 was close to peak efficiency and still left a reasonably large wing area, as the notion of needing a lower stall speed still lingered in the designer's head. Figures 2.5 and 2.6 demonstrate the region of higher efficiency.

At this point it should be explained that the processes of choosing a design point, weight estimate, and battery estimate were highly nonlinear and quite iterative and interconnected. Thus, whenever an update was made to the weight estimator code or the design space diagram code, the aircraft would change properties, leading to many "intermediate" iterations that were not considered major revisions. Thus, "Iteration 1" as a chapter or subdivision is somewhat arbitrary but generally encompasses the process of conventional aircraft design before making significant progress with SUAVE analysis tools.

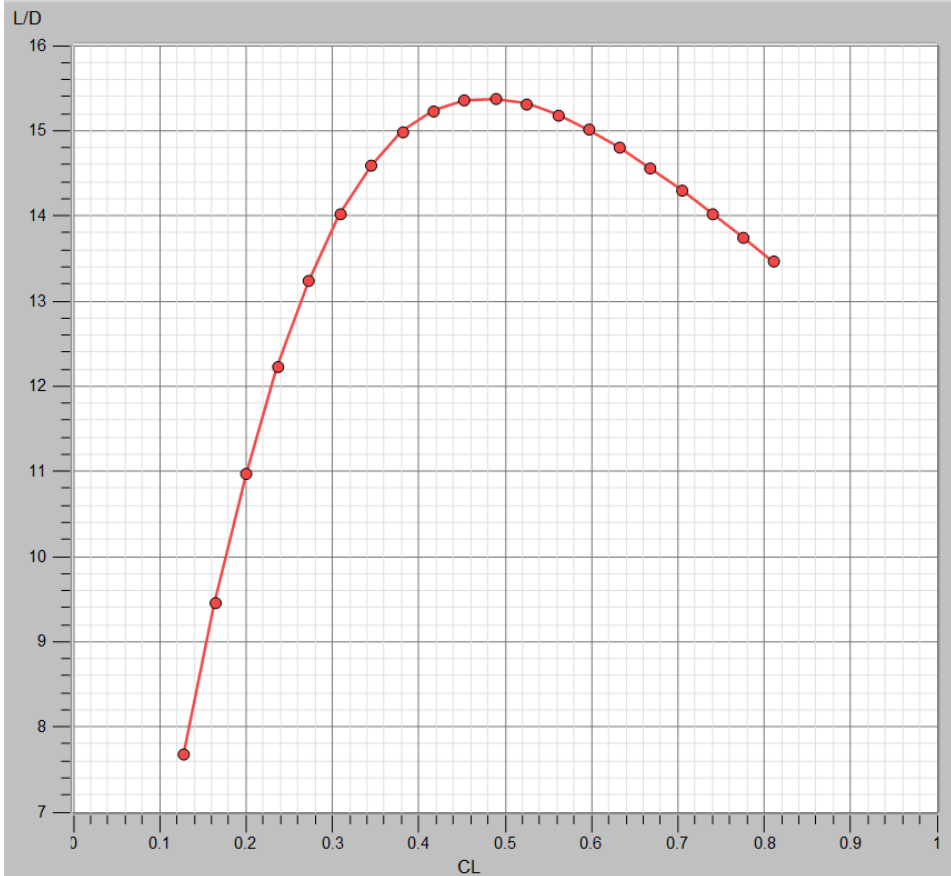


Figure 2.5: $\frac{L}{D}$ vs C_L for a wing using NACA 2412 airfoil (chosen for similarity to aircraft in this class, not used in final configuration)

2.4 First Pass Vehicle Component Sizing

From the weight estimation and design space diagrams, the wing area of the aircraft was simply computed as the weight divided by the wing loading in SI units $S = \frac{W_0}{\frac{W}{S}}$. The power requirement was then estimated as the weight divided by the power loading $\frac{W_0}{P}$. While more detailed power requirements were set when doing propulsion analysis in later sections, this provided a reasonably estimate based on point mass dynamics described above.

Next, the aircraft wing aspect ratio AR was chosen. In order to limit the span to a reasonable size that one individual might carry it by hand, the span was constrained to 1.6 meters (around 5.25 feet). This gave an initial estimate of aspect ratio 7 in order to limit the span given the wing area. This was then used to inform the weight estimation again, and the steps were repeated in a few iterations to arrive at the final iteration 1 configuration. The wing was put in a high wing configuration to aid lateral stability, as this produces a returning moment in sideslip, so as to passively maintain zero roll angle. As a result, the boom and tail were mounted at a similar level in order to keep the motors on the same plane to simplify design and avoid a significant difference in thrust during hover due to ground effect.

The tail was simply sized using the horizontal and vertical tail volume coefficient method. Compared to a conventional tail, a V-tail was decided upon due to its lower parasitic drag. Thus, the effective vertical and horizontal

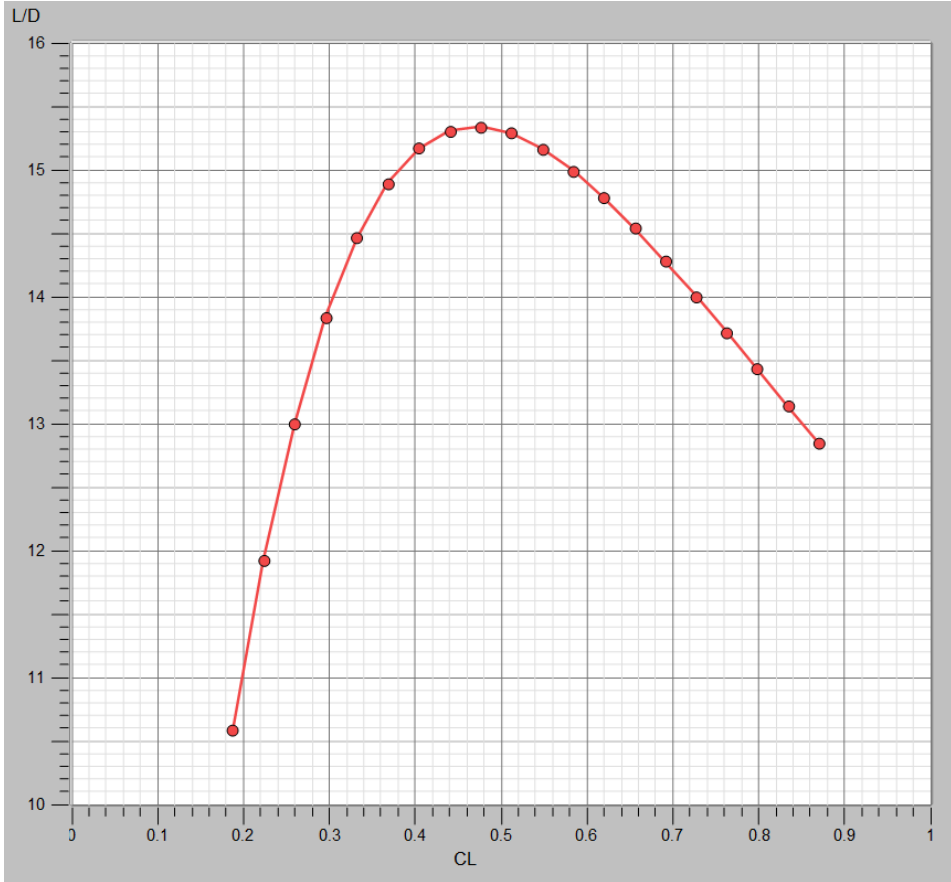


Figure 2.6: $\frac{L}{D}$ vs C_L for an Eppler 205 airfoil (chosen for similarity to aircraft in this class, not used in final configuration)

areas of the tail are simply the projections of the V-tail on the horizontal and vertical planes. Initially, the lever arm of the tail was 0.78m, to place its origin at a convenient 0.8m behind the nose. This was changed in future iterations with more robust reasoning, but provided a reasonable starting point. The tail volume coefficient method ensures the moment of the tail around the center of mass is approximately the same for a given tail volume coefficient. For instance, a larger lever arm requires a smaller tail. Horizontal and vertical tail volume coefficients are defined as follows, respectively [4]:

$$C_{HT} = \frac{L_{HT}S_{HT}}{C_W S_W} \quad (2.4.1)$$

$$C_{VT} = \frac{L_{VT}S_{VT}}{C_W b_W} \quad (2.4.2)$$

where L is the lever arm from the quarter chord of the tail to the quarter chord of the wing, S is the area of the surface, b is the span, C_W is the mean aerodynamic chord (MAC) and S is wing area. This method can be found in Raymer's *Aircraft Design*.

For different classes of aircraft, different volume coefficients are used, as they have different dynamic requirements. For this application, the tail values near a jet transport were used, providing high pitch and yaw authority and large volume for greater stability. A horizontal coefficient of 1.0 and vertical coefficient of 0.09 were selected to be consistent with table 2.7.

| | Typical Values | |
|--------------------------------|---------------------|-------------------|
| | Horizontal c_{HT} | Vertical c_{VT} |
| Sailplane | 0.50 | 0.02 |
| Homebuilt | 0.50 | 0.04 |
| General aviation—single engine | 0.70 | 0.04 |
| General aviation—twin engine | 0.80 | 0.07 |
| Agricultural | 0.50 | 0.04 |
| Twin turboprop | 0.90 | 0.08 |
| Flying boat | 0.70 | 0.06 |
| Jet trainer | 0.70 | 0.06 |
| Jet fighter | 0.40 | 0.07–0.12* |
| Military cargo/bomber | 1.00 | 0.08 |
| Jet transport | 1.00 | 0.09 |

Figure 2.7: Daniel Raymer’s *Aircraft Design* Tail Volume Coefficient reference table [4]

Table 2.1: Iteration 1 Key Component Parameters

| | |
|------------------------------------|-------|
| W/S (Pa) | 78 |
| W/P (N/Watt) | 0.06 |
| Est W0 (N) | 27 |
| Ref Area S (m^2) | 0.346 |
| AR | 7 |
| Span b (m) | 1.56 |
| MAC (m) | 0.222 |
| Cruise Speed (m/s) | 17.88 |
| Dynamic Pressure q @ 400 ft (Pa) | 193.7 |
| Cruise Cl | 0.403 |
| Taper | 0.48 |
| Root Chord (m) | 0.33 |
| Tip Chord (m) | 0.16 |

Table 2.2: Iteration 1 Tail Parameters

| | |
|-------------------------|--------|
| C_{HT} | 1.000 |
| C_{VT} | 0.090 |
| $L_{HT}(m)$ | 0.780 |
| $L_{VT}(m)$ | 0.780 |
| $S_{HT}(m^2)$ | 0.099 |
| $S_{VT}(m^2)$ | 0.062 |
| tail dihedral (deg) | 32.211 |
| overall area $S_T(m^2)$ | 0.117 |

The fuselage was initially sized based on an estimated payload the size of a standard 0.5 liter water bottle in tandem with a large 6000+ mAh battery. Furthermore, the fuselage was lengthened to allow positioning of the battery to adjust the center of gravity. The rear of the fuselage was tapered to a 20mm boom in order to minimize the interference of the boom and the rear vertical

rotor. The result was a 18cm wide, 15cm tall elliptical cross section that tapers at the nose and rear boom. The full cross section area was extended for 0.56 meters.

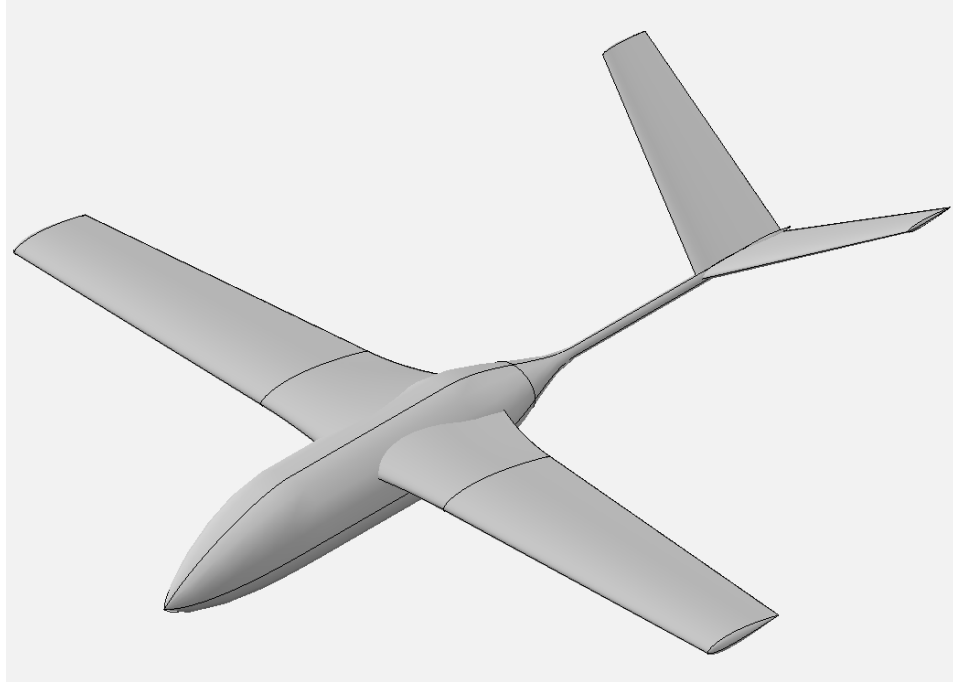


Figure 2.8: Iteration 1 Final Configuration Sketch

2.5 SUAVE Basic Implementation

The implementation of SUAVE was an arduous task at first, but later became a more intuitive and useful workflow. Due to a high amount of dependency on external packages and system type, debugging SUAVE to run the simplest of examples took many hours, with little documentation by the authors on how to properly set up the software. Furthermore, deconflicting dependency issues between SUAVE and OpenVSP Python packages took immense amounts of debugging, testing, and time.

For reference, the version of SUAVE that works is compiled and run on windows system for linux using Ubuntu 24.04. SUAVE 2.5.2 was run with Numpy 1.23.5, Scipy 1.9.3, Python 3.9.21, Scikit-learn 1.1.3, Matplotlib 3.9.4, and OpenVSP 1.26.1. Note that a separate environment is needed to run OpenVSP, as the dependencies were somewhat different than those of SUAVE.

SUAVE analysis was done in the form of a mission analysis, where an aircraft configuration is constructed, analyses are set up, mission segments are established, and the analyses are run on the constructed vehicle. For the vehicle construction, an aircraft configuration was defined using a main wing, fuselage, and tail. The main wing was initially composed of three segments: the root segment, tip segment, and intermediate segment. Each segment could be parametrized to have different airfoils, chords, angles of incidence, and more. The fuselage was constructed similarly, with five cross sections separating segments from tip to tail. The fuselage was initially constructed after modeling

a similar fuselage in OpenVSP and copying over reasonable values. SUAVE contains its own data structures similar to a dictionary that organize aircraft components and sub-components neatly. For specific aircraft dimensions of iteration 1, see the code "vtol_mk2_v1.py".

After the component sizing was translated from the sizing calculations to SUAVE for iteration 1, the energy network was defined. The realistic energy network of the aircraft consists of a lithium polymer battery, electronic speed controller, brushless motors, and propellers. SUAVE contains scripts that generates optimal propeller geometries depending on input parameters. For this application, the propeller was designed primarily to avoid stall in the hover, climb, and cruise conditions. While changing the propeller changed some aspects of the aircraft energy consumption, it did not affect the aircraft aerodynamics much. For an initial starting point, 8" diameter propellers were selected due to the fact that drones of similar size use propellers around this diameter. SUAVE then runs a script that sizes a motor from the propeller characteristics.

The SUAVE analysis initially resulted in extremely high drag, and debugging the drag breakdown led to a finding about SUAVE's parasitic drag approximation. An additional coefficient of excrescence drag, that of additional features that may interfere with a smooth streamlined body such as antennae protrusions, rivets, and cavities was added to the parasitic drag coefficient based on an empirical curve fit. However, this model was built on data from large commercial aircraft and did not apply to small UAVs, leading to a highly inaccurate overestimate of excrescence drag. The component of the python package that adds this drag was commented out for the remainder of this project. From there, the drag was compared to that of OpenVSP results, and they matched relatively well. A propeller design that did not stall the blade element method analysis that SUAVE runs had the following parameters in table 2.3. For visualization, an XROTOR loft is pictured in Figure 2.9.

Table 2.3: Iteration 1 Propeller Parameters

| | |
|------------------------|-------|
| blades | 3 |
| freestream velocity | 17.88 |
| angular velocity (rpm) | 7215 |
| tip radius (in) | 4 |
| design Cl | 0.5 |
| design thrust (N) | 2 |

This propeller serves as a starting point and further analysis is explained in later chapters for the propeller selection.

SUAVE requires the user to define analyses, and the Fidelity Zero model was chosen, which is SUAVE's built in vortex lattice method solver. For the vortex lattice discretization, 40 spanwise panels were used, with 25 chordwise panels. The mission was defined according to that described in the Intro-

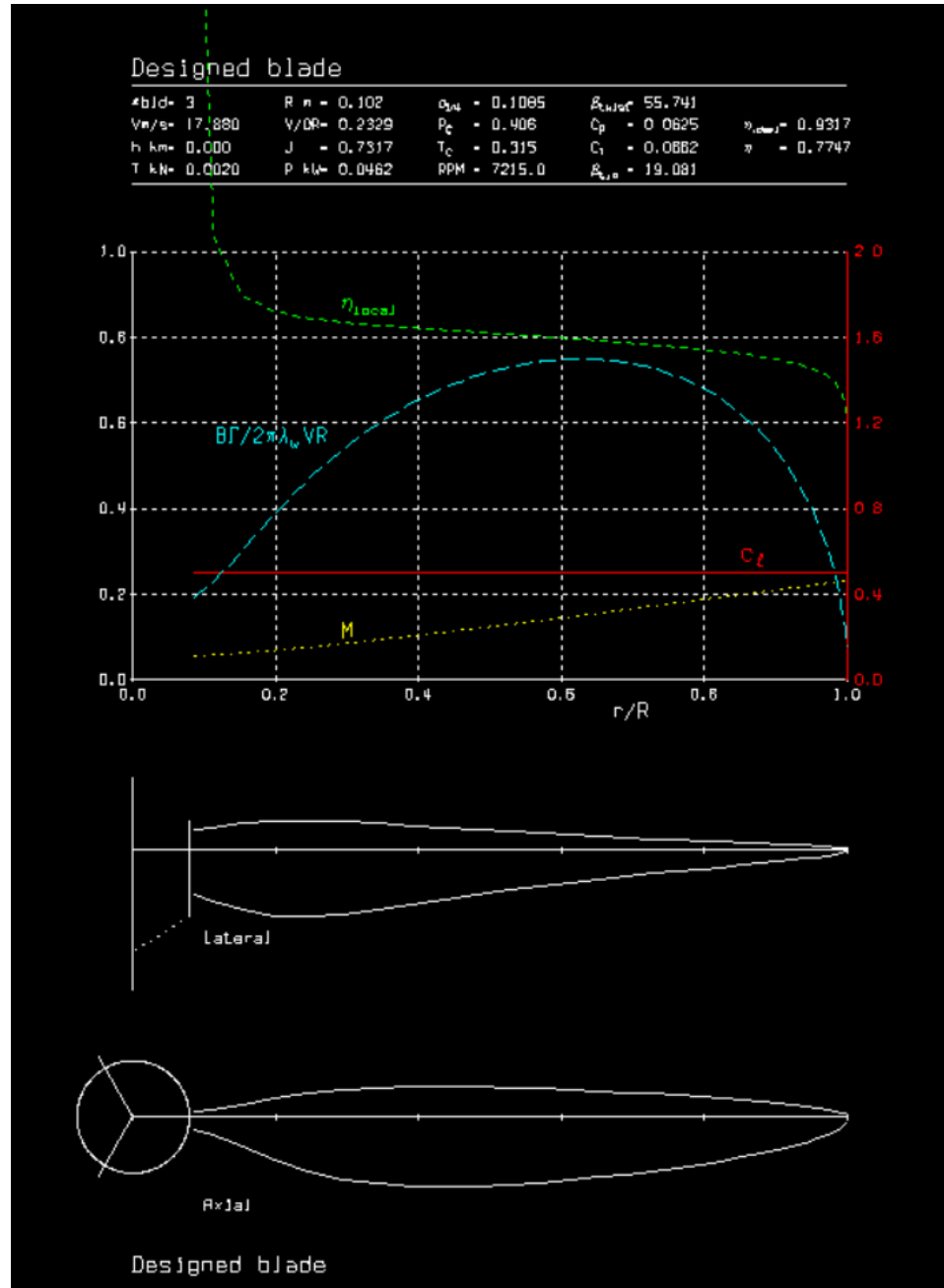


Figure 2.9: Propeller Geometry for Iteration 1

duction. Multiple configurations of the aircraft were defined. In the cruise configuration, the two tractor motors are oriented in the direction of the aircraft longitudinal axis for efficient forward thrust. The rear motor remains pointed upward and idles in cruise. In the hover configuration, all motors orient in the aircraft z-direction, perpendicular to the longitudinal axis. This vectors thrust upward from all three motors. Configurations are assigned to each of the mission segments, and transition was omitted from the analysis due to complexity in modeling a tiltrotor mechanism. This was deemed acceptable since transition was expected to take minimal energy and time, only lasting a few seconds for each transition to and from hover configuration. Finally, the analyses were setup and run, with outputs in the form of plots and a printed report of aerodynamic characteristics, energy network performance, and mission progression with time.

2.6 SUAVE Results

Below are the results of SUAVE analysis of aircraft iteration 1. Figure 2.10 suggests that the aircraft experiences a drag of around 2.4 Newtons, which results in the somewhat low lift to drag ratio of 11.98 in Figure 2.11. In Figure 2.11, the drag coefficient is an expected value of approximately 300 counts, and the lift is as designed, at $0.4 C_L$. The battery pack conditions in Figure 2.13 indicate that the battery capacity selected would likely be sufficient to complete the mission, but energy analyses were done in more detail in later chapters. The disc power loading in Figure 2.14 shows that hover thrust efficiency is quite high at over 6 grams per watt. The propeller and motor efficiencies in Figure 2.15 are informative, showing approximately 70% efficiency for both the motor and propeller. This efficiency statistic was a significant step toward higher accuracy in Iteration 2 simulations. Figure 2.16 shows the flight profile over time, which is as described in the Introduction.

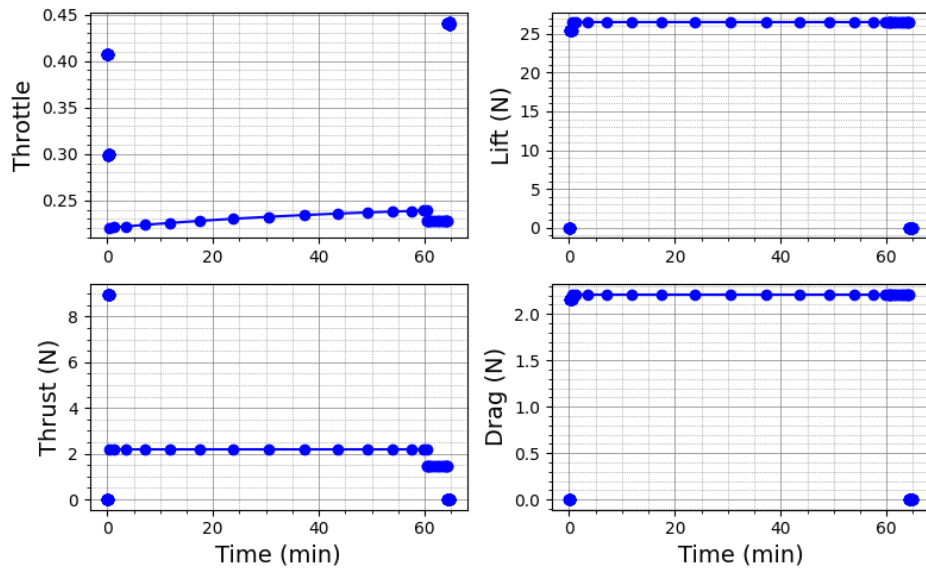


Figure 2.10: Iteration 1 Aerodynamic Forces

2.7 Comparison of Configurations

A blended wing body aircraft was briefly compared to the conventional aircraft. Using SUAVE, a simple flying wing with extended fuselage section was modeled, and the resulting $\frac{L}{D}$ ratio reached over 15.0. It should be noted that SUAVE estimates of $\frac{L}{D}$ are always below that of OpenVSP, which predicted closer to 20 or higher. While the efficiency gain is significant, the control problem introduced likely would slow the development of the aircraft build. Thus, the BWB concept was reserved for the next iteration of aircraft and considered a topic for senior Thesis.

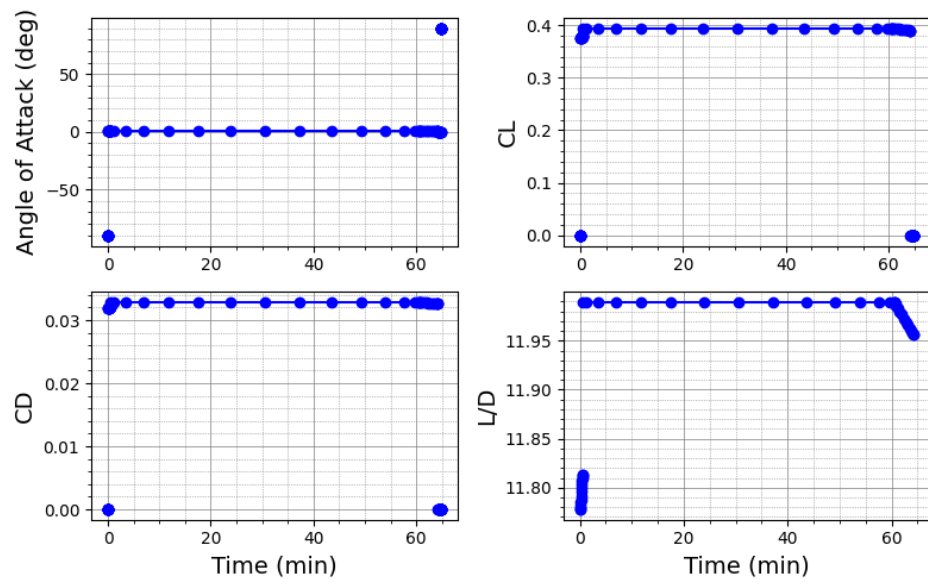


Figure 2.11: Iteration 1 Aerodynamic Coefficients

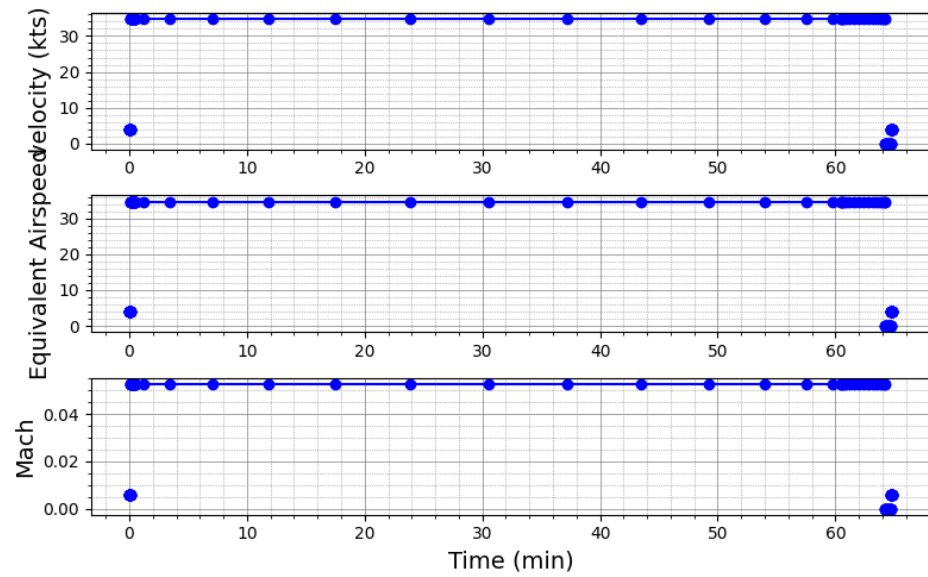


Figure 2.12: Iteration 1 Velocities

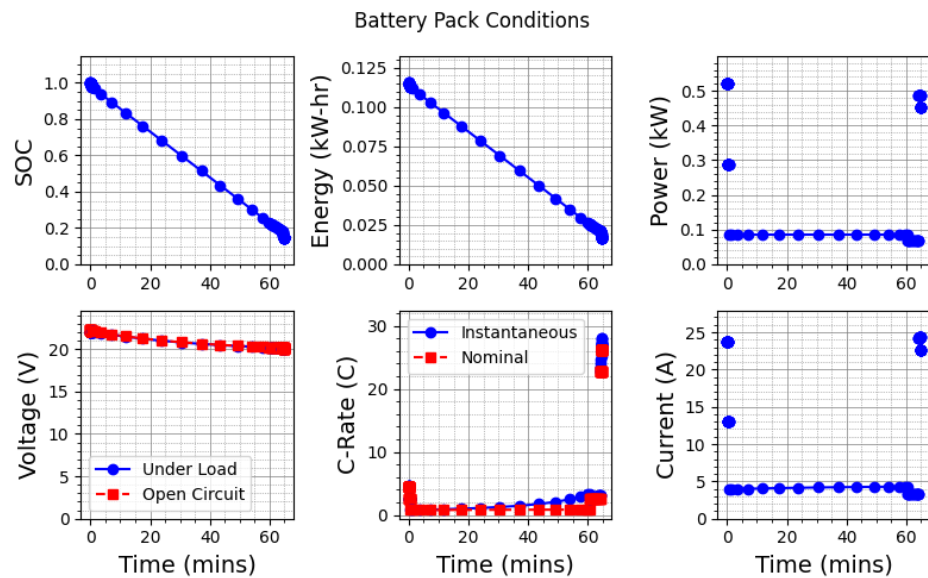


Figure 2.13: Iteration 1 Battery Conditions

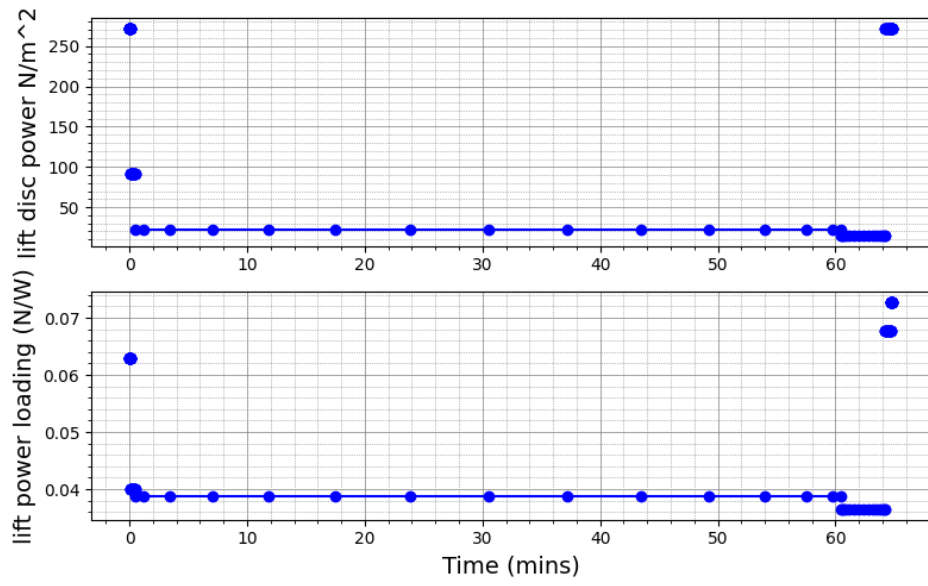


Figure 2.14: Iteration 1 Disc Power Loading

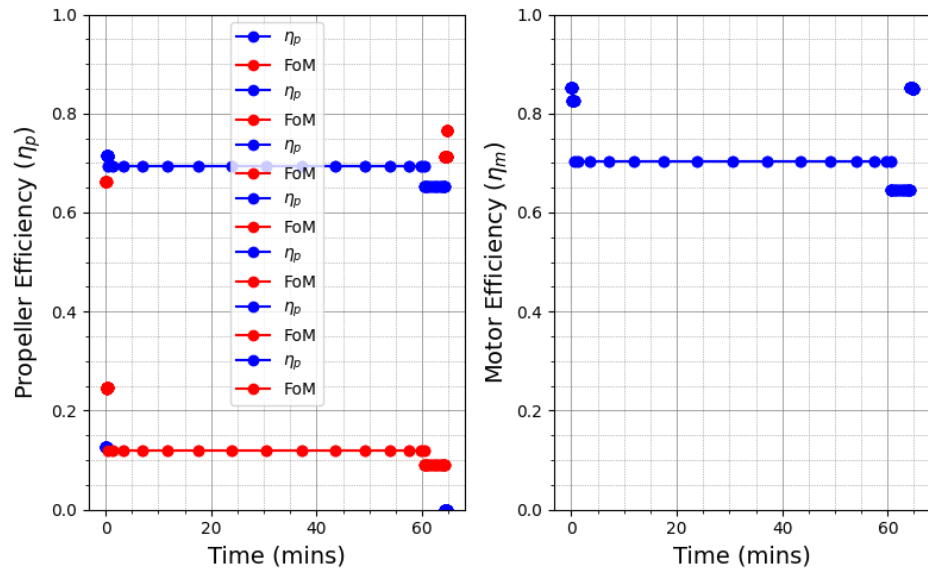


Figure 2.15: Iteration 1 Electric Motor Performance

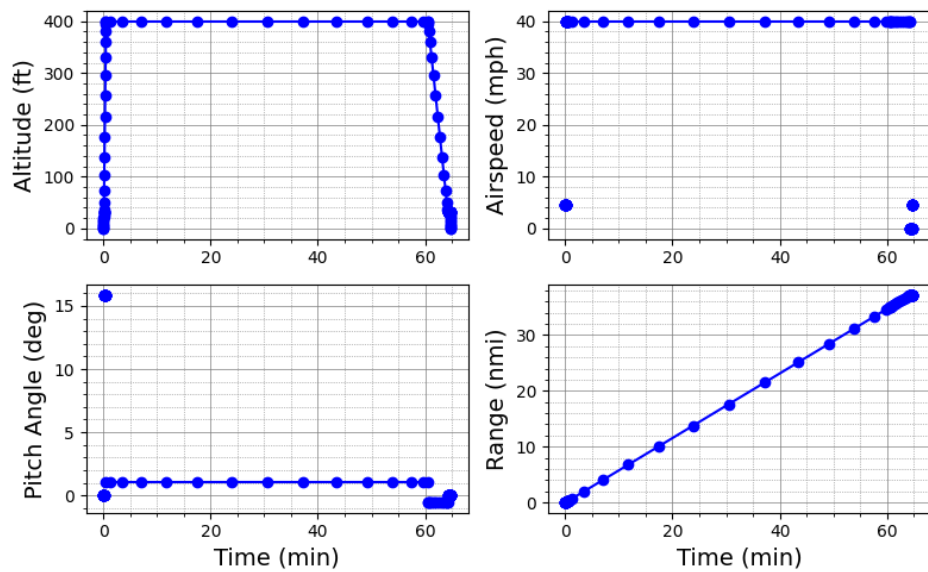


Figure 2.16: Iteration 1 Flight Conditions

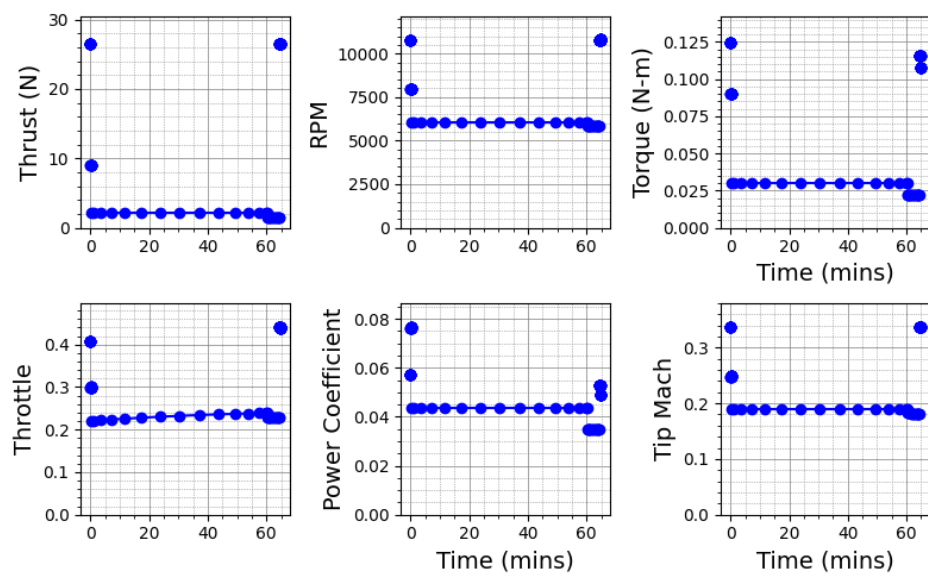


Figure 2.17: Iteration 1 Propeller Performance

Chapter 3

VTOL MK2 Iteration 2

3.1 Iteration Goals

While the entire process of designing this aircraft was quite nonlinear, Iteration 2 attempts to capture a variety of design considerations that marked a significant step in increasing the accuracy and fidelity of analyses of aircraft performance. This includes an updated weight and battery estimate, significantly more detailed airfoil selection, a tail drag minimization script, and more SUAVE simulations. Correcting for the efficiencies reported by SUAVE was a significant step toward higher accuracy modeling. A more accurate battery capacity and weight were found, and an airfoil was chosen. Iteration 2 SUAVE source code can be found in the file "vtol_mk2_v2.py".

3.2 Iteration 2 Weight, Battery, and Design Space

Iteration 2 began with an updated physical model for the weight and battery capacity estimation scripts. Since efficiencies of the motor and propeller were much too high the first iteration around, the efficiencies were updated using SUAVE analysis of the Iteration 1 aircraft. SUAVE approximates the motor and propeller efficiencies at 70% each, resulting in more loss than Iteration 1. This is more accurate to what might be expected in real life. This resulted in the following spread of aircraft weight and battery estimates for a fixed aspect ratio of 7, seen in table 3.1.

From the spread of available weight estimates in Iteration 2, an empty mass fraction was chosen based on the following thought process: Creating a 3D printed airframe is heavier than one of foam for the same planform, due to higher density and more structural concerns. Thus, creating an airframe below 1 kg if infeasible, while targeting 1.5 to 1.6 kg is a reasonable design challenge for weight minimization. Achieving a 2 kg empty weight is quite easy and not much of a challenge. Thus, the weight fraction of 0.575 was

Table 3.1: Iteration 2 Updated Weights and Battery Capacities

| $\frac{W_e}{W_0}$ (AR=7) | W0 (N) | Battery mAh | We | Battery Wh | Battery Mass (kg) |
|--------------------------|--------|-------------|-------|------------|-------------------|
| 0.55 | 25 | 5700 | 13.75 | 126.54 | 0.617 |
| 0.562 | 27 | 6100 | 15.17 | 135.42 | 0.661 |
| 0.575 | 28.3 | 6600 | 16.27 | 146.52 | 0.715 |
| 0.588 | 30.5 | 7100 | 17.93 | 157.62 | 0.769 |
| 0.6 | 33 | 7700 | 19.8 | 170.94 | 0.834 |

Estimated Weight vs AR for various Empty Weight Fraction Estimates, Iter 2

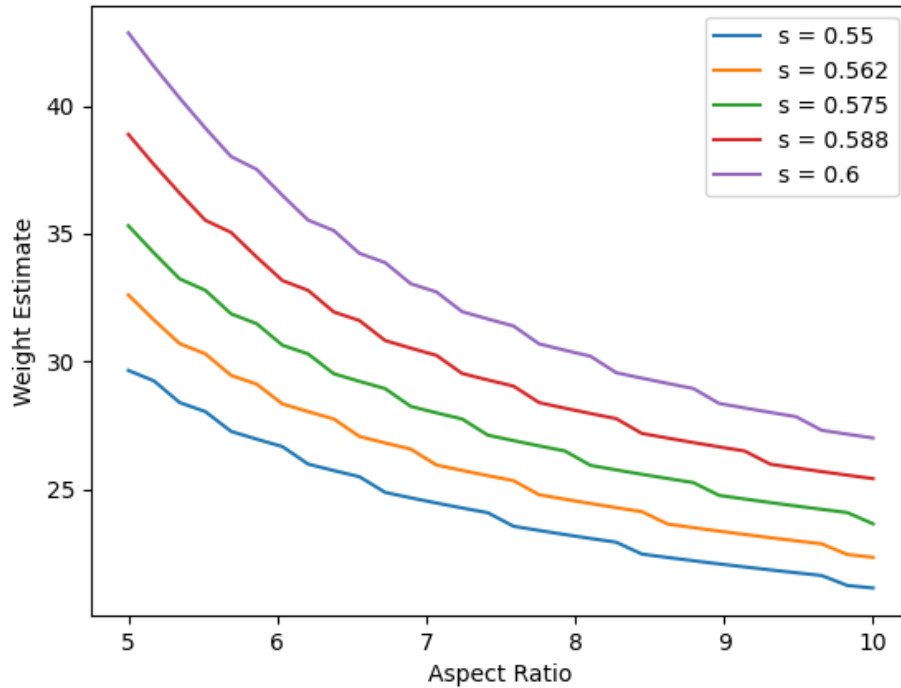


Figure 3.1: Iteration 2 Updated Weight Estimation Plot

chosen for approximately 1600 grams of empty weight. This led to an updated weight of 28.3 Newtons and a battery capacity of 6600 mAh with the updated efficiencies.

3.3 Iteration 2 SUAVE Analysis

SUAVE analysis of Iteration 2 included experimentation with adjusting planform quantities based on the updated weight. The plots are listed below, but the primary identifying factor is the higher $\frac{L}{D}$ in figure 3.4, which will be the primary design goal going forward.

Battery Capacity vs AR for various Empty Weight Fraction Estimates, Iter 2

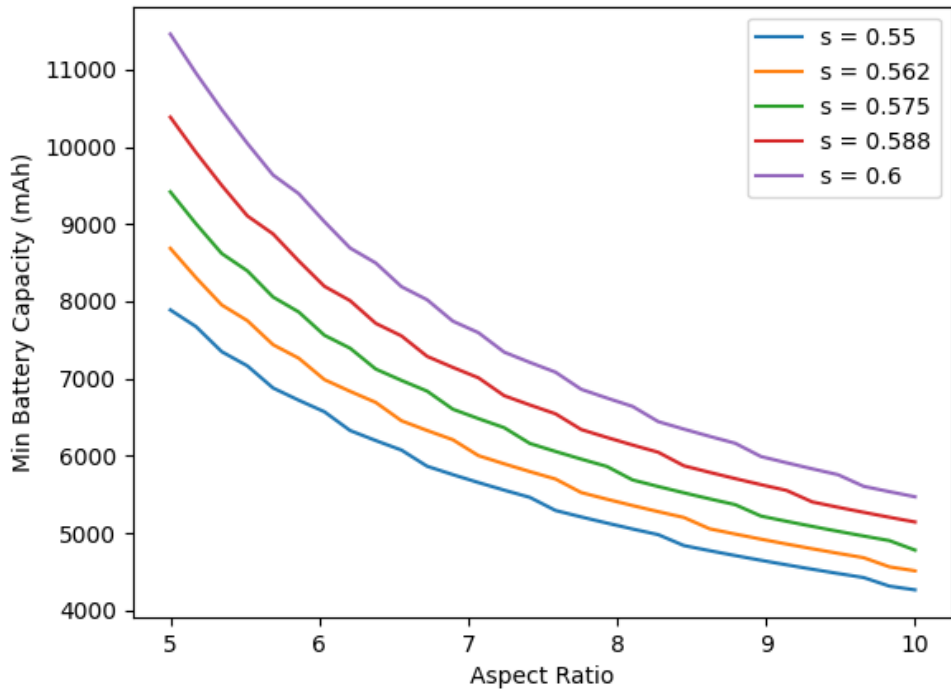


Figure 3.2: Iteration 2 Updated Battery Capacity Estimation Plot

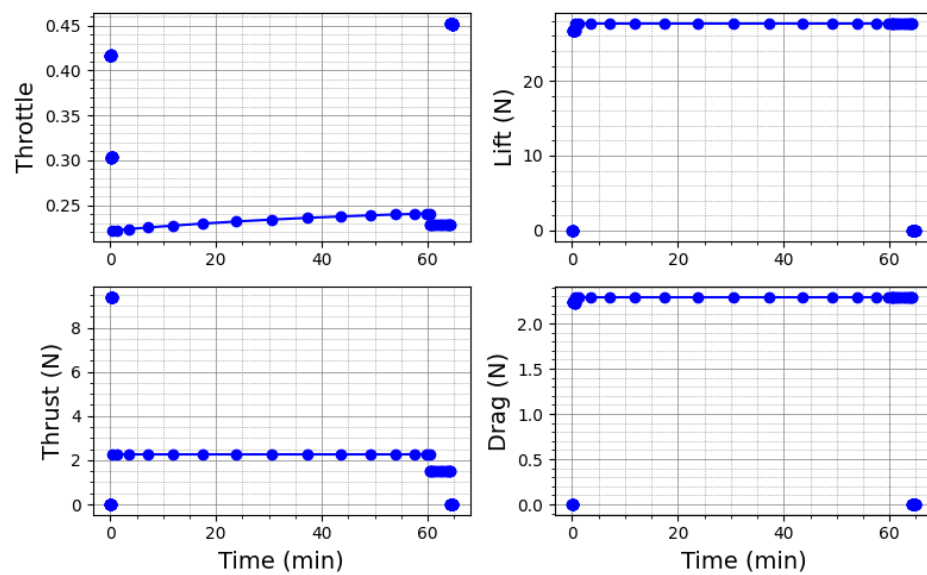


Figure 3.3: Iteration 2 Aerodynamic Forces

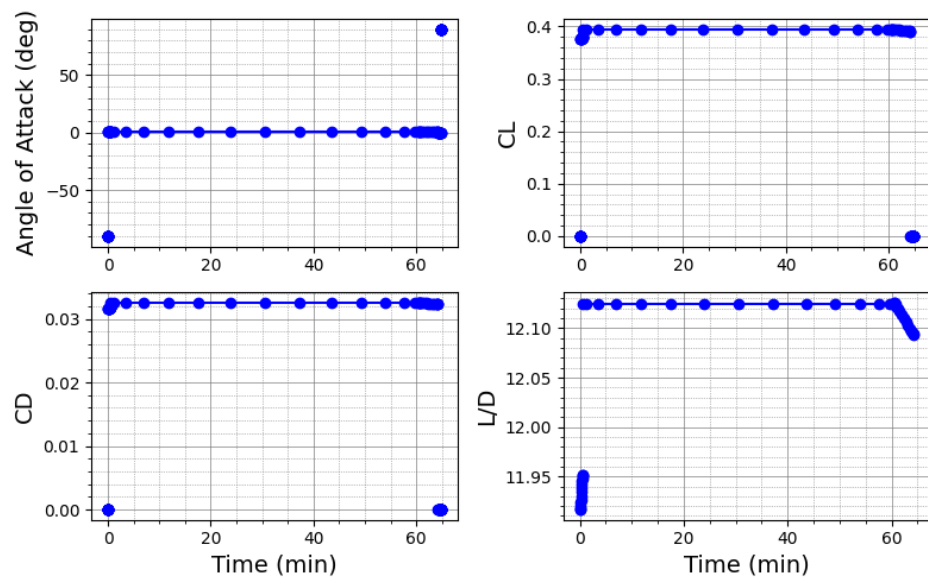


Figure 3.4: Iteration 2 Aerodynamic Coefficients

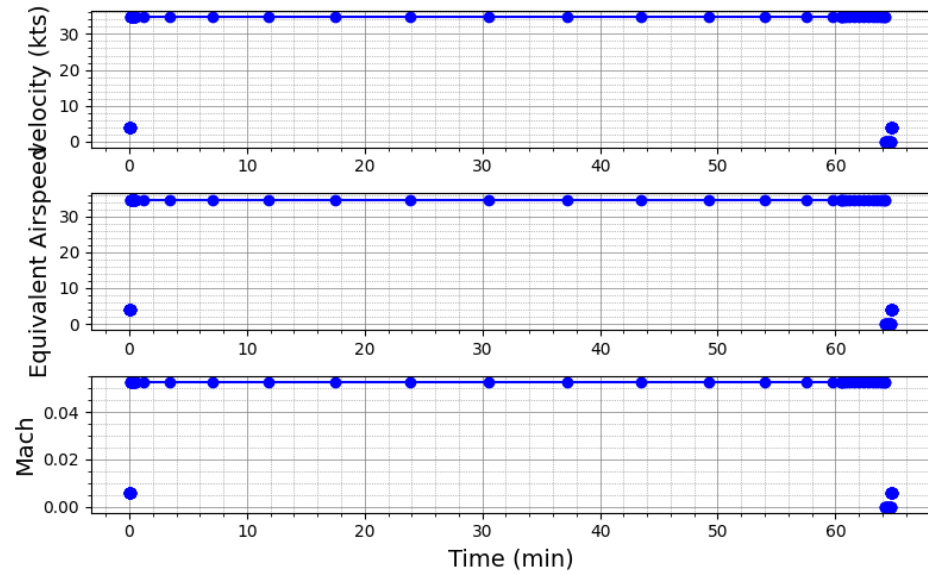


Figure 3.5: Iteration 2 Velocities

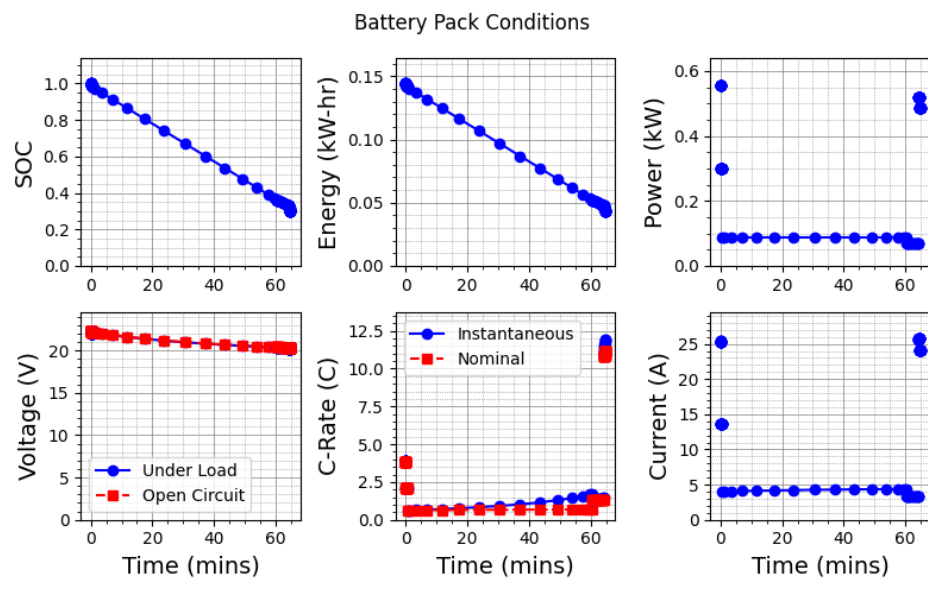


Figure 3.6: Iteration 2 Battery Conditions for Cruise Segment Only (With Updated Propeller)

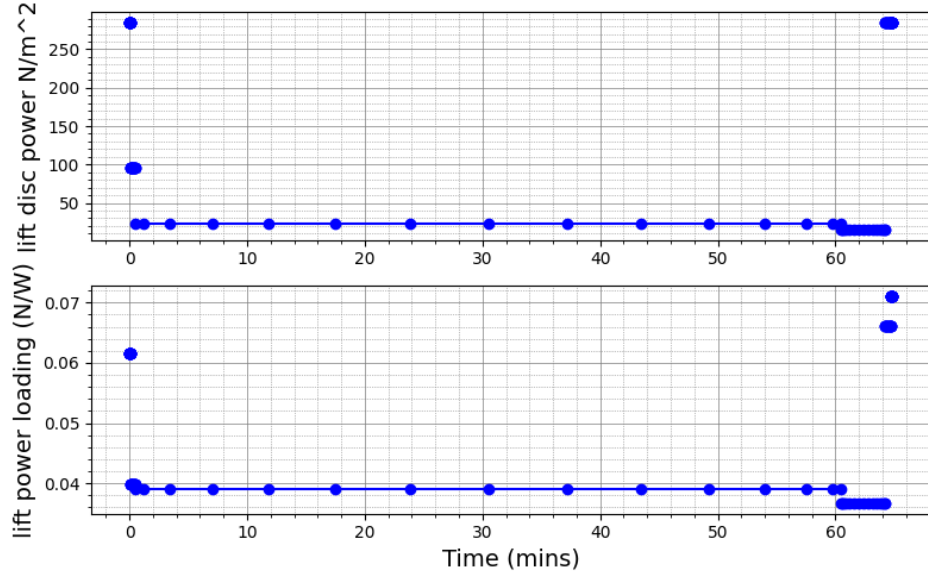


Figure 3.7: Iteration 2 Disc Power Loading

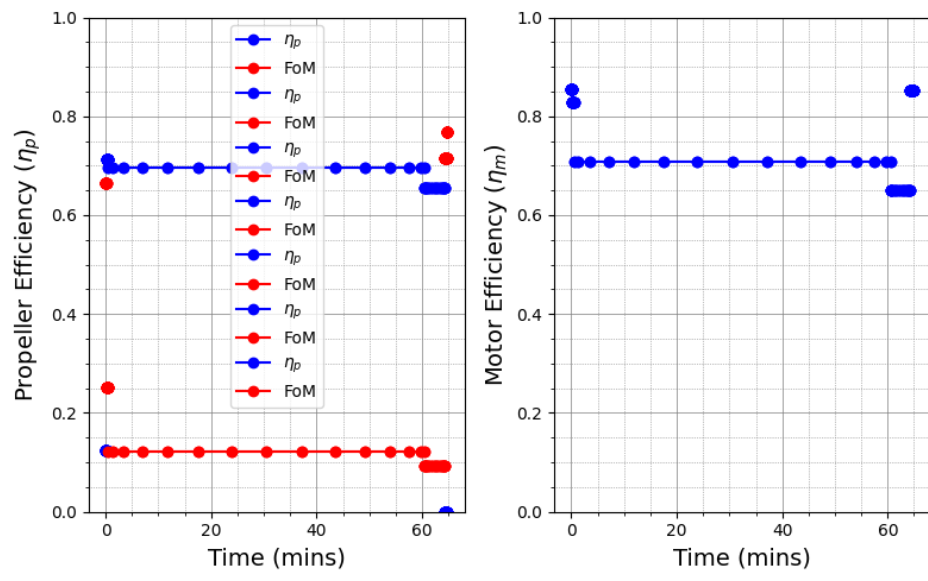


Figure 3.8: Iteration 2 Electric Motor Performance

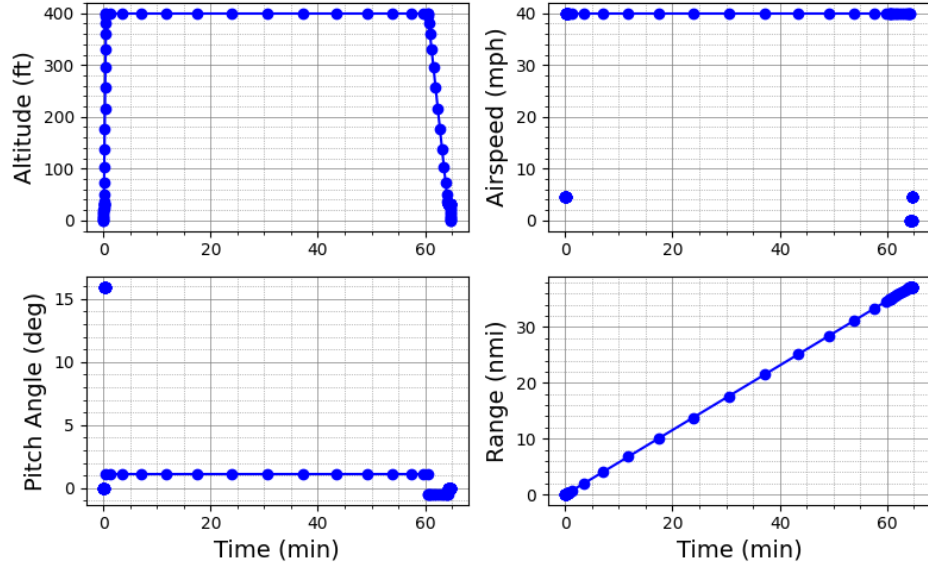


Figure 3.9: Iteration 2 Flight Conditions

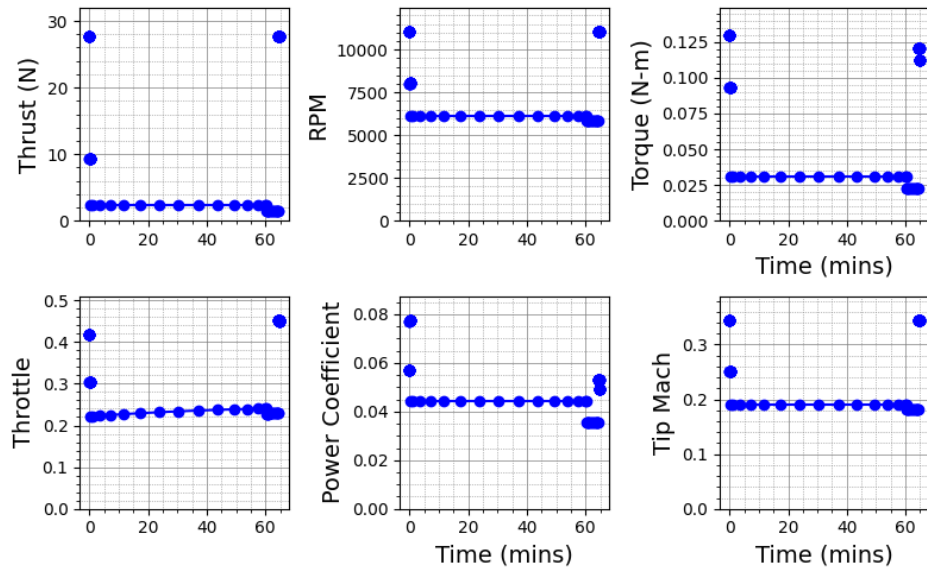


Figure 3.10: Iteration 2 Propeller Performance

3.4 Airfoil Selection

Airfoil selection was done with the primary goal of maximizing efficiency $\frac{L}{D}$ in cruise and the secondary goal of avoiding sharp stall and excessive aerodynamic moments. Because the Reynolds number of this aircraft is on the order of 2×10^5 , airfoils that perform well at low Reynolds numbers were desired.

3.4.1 Airfoil Candidates

A list of airfoils was chosen from existing databases including NACA 4-series airfoils, Eppler series airfoils, and Selig airfoils from airfoiltools.com. To select the range of airfoils, other aircraft similar in size were studied, and airfoils were inspired by a study on Low Reynolds Number Airfoil Design by Michael Selig [5]. The airfoil list and some general characteristics are listed in Table 3.2

3.4.2 XFLR5 and XFOIL Analyses

XFLR5, a wrapper of XFOIL with a graphical user interface, was used to analyze and compare airfoils. Each of the airfoils in Table 3.2 was loaded with 150 points, and a sweep of airfoil polars was computed for Reynolds numbers between 30000 and 600000 in order to cover the range of Reynolds numbers at which each local cross section of the wing might experience. These polars were computed for angles of attack between -5 and 15 degrees at 0.25 degree increments for a detailed polar. Most of the analysis was done at the Reynolds number of the mean aerodynamic chord, approximately 2×10^5 . The polars at other Reynolds numbers were used in 3D wing analysis, which draws upon the airfoil polars to determine local lift distribution. N_{crit} was set to 9 because

Table 3.2: Airfoil Considerations. "t" represents thickness while "c" represents chord.

| Airfoil | t/c (%c) | Max t Location (%c) | Camber (%c) | Max Camber Location (%c) |
|---------|----------|---------------------|-------------|--------------------------|
| E205 | 10.5 | 29.7 | 2.5 | 38.7 |
| E214 | 11.1 | 33.1 | 3.7 | 59.6 |
| E374 | 10.9 | 34.3 | 2 | 38.9 |
| E387 | 9.1 | 31.1 | 3.2 | 44.8 |
| N2412 | 12 | 30 | 2 | 40 |
| N2410 | 10 | 30 | 2 | 40 |
| N4412 | 12 | 30 | 4 | 40 |
| N4412 | 10 | 30 | 4 | 40 |
| S2091 | 10.1 | 26 | 3.7 | 39.5 |
| S3021 | 9.5 | 30 | 2.5 | 39.2 |
| S4061 | 9.6 | 30.9 | 3.3 | 44.7 |
| SD7032 | 10 | 26.6 | 3.4 | 45.1 |

most of the flow over the airfoil was assumed to be laminar. Because local 2D $\frac{L}{D}$ results do not clearly translate to a 3D wing without knowing the lift distribution, the plots of 2D $\frac{L}{D}$ of each airfoil were not utilized. Instead, 3D wing analysis using each airfoil was more useful. For the 2D case, however, the stall characteristics were investigated. Figure 3.11 depicts the C_L vs α of each airfoil. Evidently, the thinnest airfoils like the E387 and S3021 show the sharpest stall characteristics, with C_L dropping rapidly after its maximum point. Other, thicker airfoils like the E214 and E374 show very gradual stall where C_L lingers near C_{Lmax} before dropping at higher angles of attack.

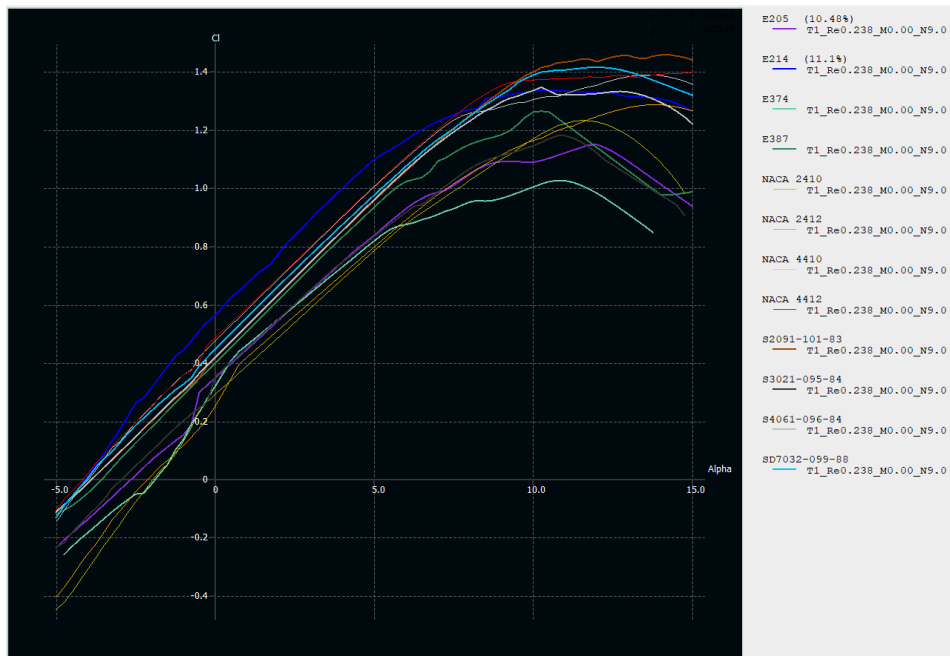


Figure 3.11: All 2D Airfoil Lift Curves Plotted in XFLR5

For each airfoil, a trapezoidal wing was created to determine the performance of each airfoil in 3D. Both panel method and lifting line method were run with similar results produced. The velocity and lift coefficient were that of the cruise segment. Figure 3.12 shows the $\frac{L}{D}$ vs C_L for each wing, with wing

0-11 corresponding to the airfoils in each row of Table 3.2, respectively. Results indicate that at the cruise C_L between 0.4 and 0.5, the NACA 2410 shows the highest efficiency. The Selig 7032 also demonstrates high efficiency and very gradual stall. Since the aircraft would transition to and from hover for takeoff and less emphasis was put on stall concerns due to hover capabilities, the NACA 2410 was chosen for the main wing. The tail utilizes a symmetric 0012 airfoil since it is expected to produce both positive and negative lift to trim the aircraft.

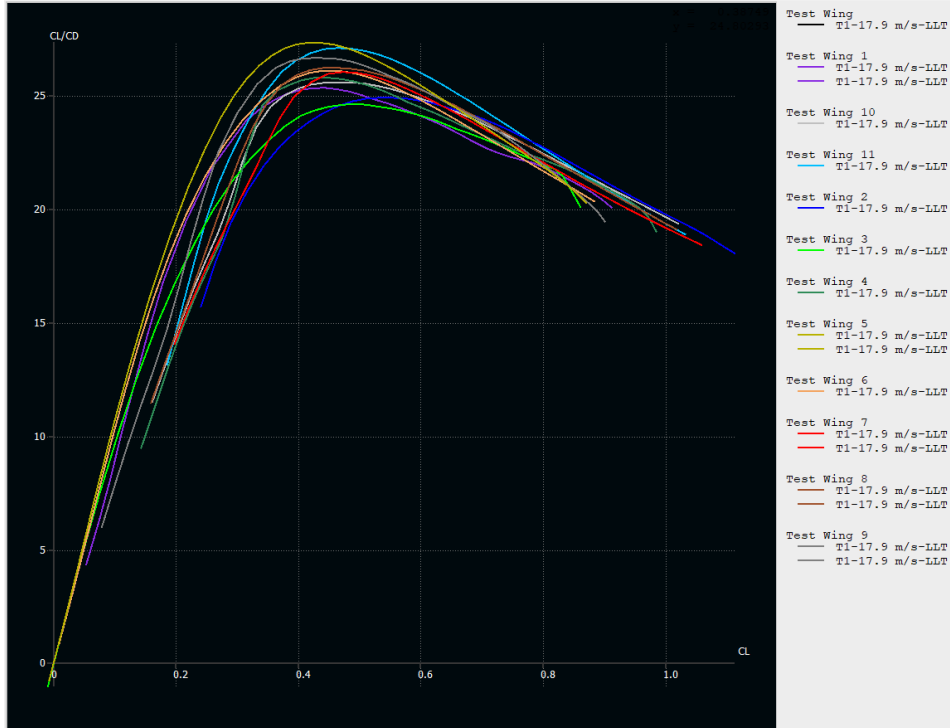


Figure 3.12: $\frac{L}{D}$ vs C_L for Wings with Candidate Airfoils

3.5 Tail Optimizer

The position of the tail was computed to minimize wetted area of the boom assembly and tail in order to minimize C_{D0} . A python script computed tail area based on the tail volume coefficient method utilized in Chapter 2 as a function of the quarter chord lever arm distance. Sweeping over a range of lever arm distance shows the effect on total boom and tail area. A longer lever arm adds fuselage area but reduces tail area. Figure 3.13 shows the minimum wetted area point, at 0.7m. A line depicting an area within 10% is used to show the sensitivity of the wetted area to lever arm, indicating an acceptable range of tail placement.

From here, information gained about the tail and airfoil informs the third and most comprehensive iteration of this aircraft.

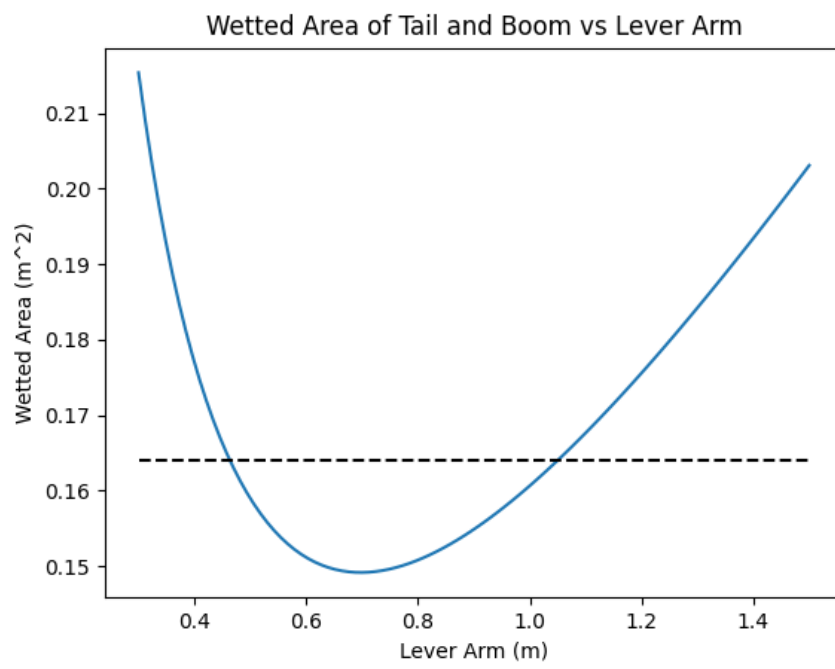


Figure 3.13: Tail Lever Arm Drag Minimum Point.

Chapter 4

VTOL MK2 Iteration 3

4.1 Iteration Goals

Iteration 3 represents a higher level of analysis done for component selection and some optimization efforts for the parametrized geometry of the aircraft. In this round of analyses and design choices, higher confidence was held in the results, as each parameter was justified through an engineering thought process that will be explained. The final version of the source SUAVE code for iteration 3 can be found in "vtol_mk2_v3_1sectioned.py". For the version that uses the correct propeller model without the blade element method stalling for better cruise segment analysis, the source code is "vtol_mk2_v3_final_correct_prop_cruise_only.py".

4.2 Weight and Battery Updated Estimate

From Iteration 2, weight and battery estimates were updated to account for changes in expected energy use. As will be explained later, a 6500 mAh capacity battery was desired for its high energy density off-the-shelf. Furthermore, Iteration 3 included a higher aspect ratio wing, so higher empty mass fraction could be accepted for the same performance. Investigating the weight and battery estimate plots, the desired battery capacity point at 6500 mAh allows for a higher empty mass fraction when operating larger aspect ratio wings. Throughout the process of Iteration 3, increasing the C_L to values above 0.5 reduced wing area to the point where a higher aspect ratio could be achieved given the span restriction of approximately 1.6 meters. Ultimately, the aspect ratio was increased to 9 without issue, and the weight was estimated at 29.3 Newtons, for an empty mass fraction of 0.594. This allowed for a 1.74 kg empty mass, increasing the weight margin for the structure.

4.3 Energy Network Component Selection

The detailed energy network component selection was done in the later iterations since it was necessary to have an accurate drag estimate. The problem of selecting a propeller and corresponding motor was coupled, and options were chosen from a variety of off-the-shelf components. The goal of the energy network was to achieve high efficiency for the motor and propeller, as this would result in the least battery capacity necessary to complete the mission.

4.3.1 Propeller and Motor Selection

Propeller efficiency for a given blade pitch distribution varies with advance ratio, defined as

$$J = \frac{V}{nD} \quad (4.3.1)$$

where V is forward velocity, n is rotations per second, and D is propeller diameter. The advance ratio dictates how much forward distance is traveled per circumferential distance. Propellers with high pitch have higher efficiency at higher advance ratios than lower advance ratios because their local angle of attack of airflow past the blade is closer to the optimal angle for maximum efficiency $\frac{L}{D}$. When selecting a propeller, in collaboration with UIUC, online vendor APC Propellers gives empirical data on products designed for UAVs and RC aircraft. These were used to correctly size a propeller for the application at hand.

A second design goal in addition efficiency in cruise was thrust in hover mode, where advance ratios would be low due to not having a high forward velocity. Furthermore, the required thrust from the propellers must be produced at a throttle point that was far below maximum output of the motors. Depending on the control algorithm used, topping out the power output of the motors during hover in order to combat perturbations from the desired state would be problematic if the maximum thrust of the propeller was a limiting factor. Since the advance ratio for optimal efficiency is different for forward flight than it is for hovering, there are conflicting goals for a propeller of fixed pitch. Due to the majority of the mission being in cruise, the energy expenditure in cruise is much higher than in hover, even though hover requires more power.

When sizing propellers, the ideal case was first considered, where propellers would operate near their maximum efficiency. First, a study was conducted to investigate what angular velocity was necessary to achieve desired advance ratios for different diameters, informing the range of angular velocities the selected motors should operate at. Propellers from 8 to 12 inches were considered. For a cruise velocity of 17.88 meters per second, the following table shows the ballpark range of angular velocities expected in cruise. Note that a regular range of advance ratios was chosen based on propellers between typical quadcopter values and slow flying fixed wing aircraft.

Table 4.1: Ballpark Angular Velocities from Various Propeller Advance Ratios and Diameters

| Diameter (in) | Desired J | n (rps) for J | omega (rpm) for J |
|---------------|-----------|---------------|-------------------|
| 8 | 0.5 | 175.98 | 10,559.06 |
| 9 | 0.45 | 173.81 | 10,428.70 |
| 10 | 0.5 | 140.79 | 8,447.24 |
| 12 | 0.5 | 117.32 | 7,039.37 |
| 8 | 0.6 | 146.65 | 8,799.21 |
| 9 | 0.63 | 124.15 | 7,449.07 |
| 10 | 0.6 | 117.32 | 7,039.37 |
| 12 | 0.6 | 97.77 | 5,866.14 |
| 8 | 0.7 | 125.70 | 7,542.18 |
| 9 | 0.72 | 108.63 | 6,517.94 |
| 10 | 0.7 | 100.56 | 6,033.75 |
| 12 | 0.7 | 83.80 | 5,028.12 |
| 8 | 0.8 | 109.99 | 6,599.41 |
| 9 | 0.8 | 97.77 | 5,866.14 |
| 10 | 0.8 | 87.99 | 5,279.53 |
| 12 | 0.8 | 73.33 | 4,399.61 |

From table 4.2, the angular velocity is higher for lower advance ratio and lower diameter, as dictated by equation 4.3.1.

Electric motors are classified by K_v , which is a constant that dictates a linear rpm response to voltage input, such that $\omega = K_v V_{in}$. Therefore to achieve a high rpm, a higher K_v rating is required for a given voltage, which depends on throttle. The aircraft should operate at a low throttle during cruise in order to have a high capacity for peak power during hover and to retain control authority during hover. For example, if cruise conditions require 90% throttle from the motor, then there is very little margin for hovering. If cruising at only 40% throttle, then there is much greater capacity for power output during hover phase and to perform the peak power spikes demanded by the control algorithm to reject perturbations from an upright hover state. For the purpose of having a large power margin for transitioning to hover mode, it was decided that the motors should run at approximately 30% throttle in cruise.

For electric motors, the equivalent circuit in steady state can be thought of as an external voltage applied across a resistive component that also experiences a back-EMF from the rotation of the motor and resulting changing magnetic field (how a motor works in the first place):

$$V = E + IR \quad (4.3.2)$$

where E is the back-EMF, I is the current, and R resistance. From here, the K_v motor constant is defined as

$$E = \frac{\omega}{K_v} \quad (4.3.3)$$

such that the current through the motor can be written as

$$I = \frac{V - \frac{\omega}{K_v}}{R} \quad (4.3.4)$$

and the torque can be written as

$$T = \frac{I}{K_v} = \frac{1}{K_v} \left(\frac{V - \frac{\omega}{K_v}}{R} - I_0 \right) \quad (4.3.5)$$

accounting for free current of the motor [1].

Electric motor efficiency is defined as the useful mechanical shaft power divided by the input electrical power. This can be written as a function of input voltage V , K_v , internal resistance R , and no-load current I_0 :

$$\eta_m = \frac{\omega T}{IV} = \frac{(1 - \frac{I_0 R}{V - \frac{\omega}{K_v}})\omega}{VK_v} \quad (4.3.6)$$

The plots for various motor options are shown below, with efficiency and torque plotted against rpm. In order to operate near highest efficiency, the motor is chosen based on the propeller required angular speed and torque at the desired throttle point. Operating near the peak of the efficiency curve is desirable. Note that these curves change for each separate input voltage, which can be tailored to meet specific power requirements by the motor.

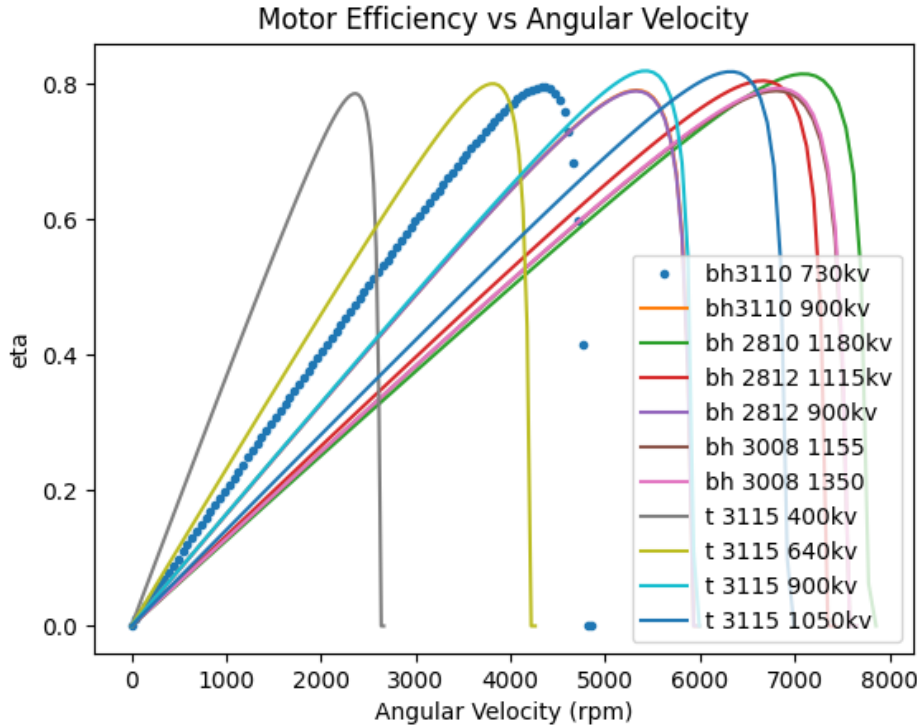


Figure 4.1: All Motor Efficiencies at 40% Throttle. Selected Motor Points are Dots.

Once the motor curves were known, specific propellers were investigated for each diameter and advance ratio combination. Propellers for each combi-

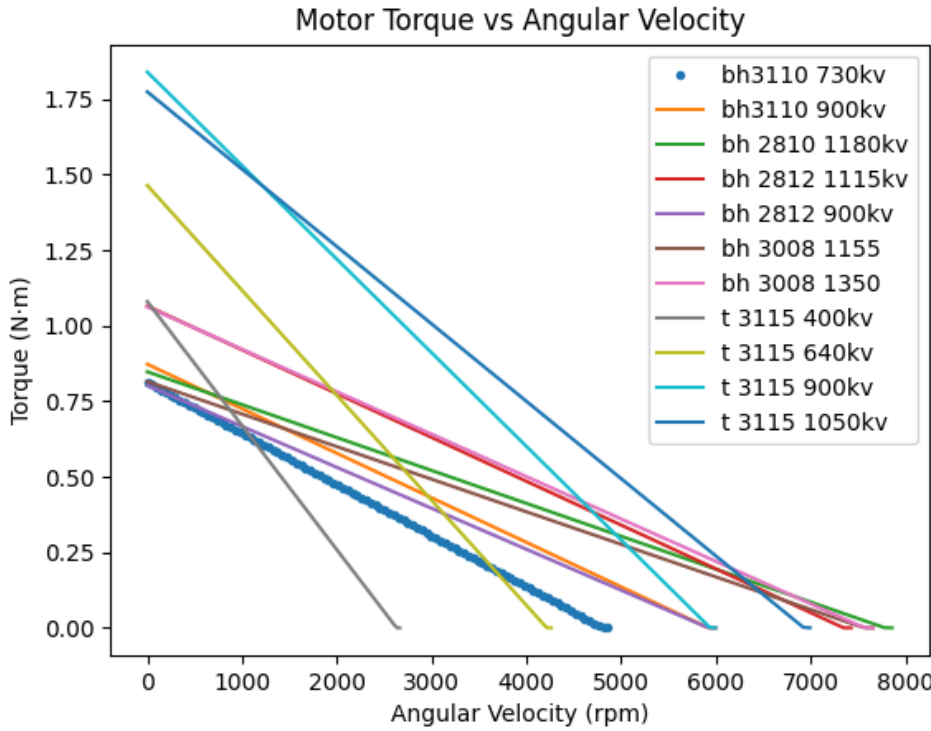


Figure 4.2: All Motor Torques at 40% Throttle. Selected Motor Points are Dots.

nation of J and D were chosen based on the efficiency peak being located at that advance ratio, by inspecting the UIUC propeller database plots. Some combinations, however, did not have a good propeller option and were omitted. Ultimately, an 8-inch, 9-inch, and 10-inch propeller were . Using an 11 or 12-inch propeller was deemed unnecessary, as the UIUC plots showed an apparent efficiency drop-off at the larger diameters.

Higher advance ratios and a larger propeller diameter were desired for lower RPM, but high efficiency and low angular moment of inertia were also prioritized. For each propeller investigated, the power, thrust, and angular velocity at maximum efficiency advance ratio was computed. From the empirical data, thrust and power were calculated using power and thrust coefficients,

$$C_t = \frac{T}{\rho n^2 D^4} \quad (4.3.7)$$

$$C_p = \frac{P}{\rho n^3 D^5} \quad (4.3.8)$$

At this point, thrust was always larger than the required thrust by the two tractor propellers, so the angular velocity was iteratively changed to converge on an accurate thrust value. Changing the RPM then changed the advance ratio, which changed the C_p and C_t of the propeller, changing the thrust again. Reiterating multiple times resulted in a value for ω that balanced the drag of the aircraft well. Because the thrust requirement necessitated an advance ratio generally lower than that of ideal efficiency, the propeller in flight would be operating on the downward slope of the efficiency vs advance ratio curve.

Examples of an η_p vs J , C_t vs J , and C_p vs J curves are given in Figures 4.3, 4.4, and 4.5 for an APC Electric 9x7.5 Slow Flying propeller. While not the propeller chosen, it shows strong efficiency characteristics with peak η_p values above 0.7. The data is also available from UIUC in text form at different angular velocities from their wind tunnel results.

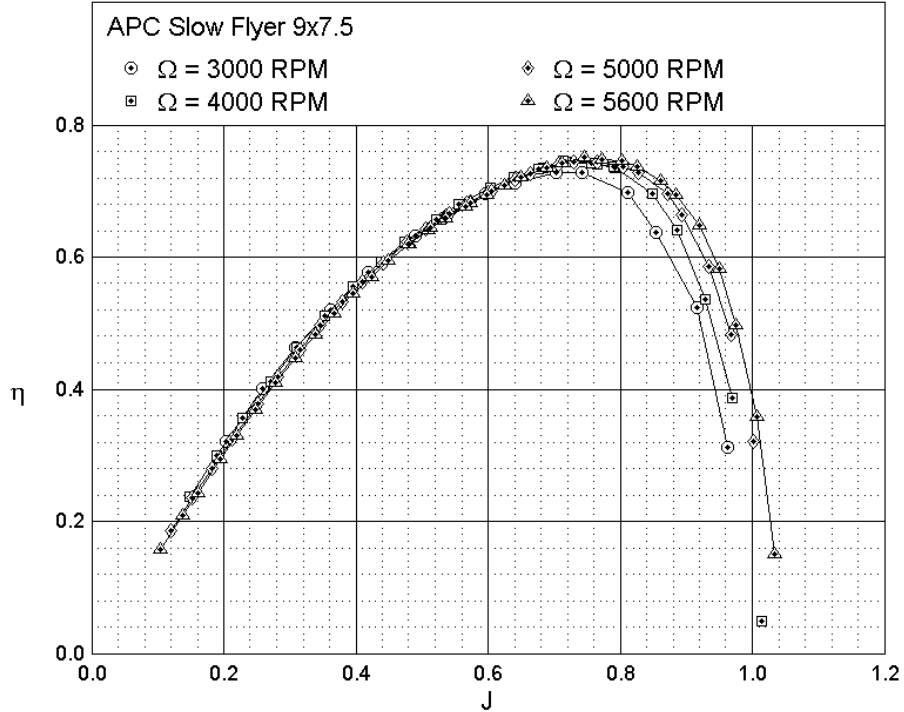


Figure 4.3: APC Slow Flyer 9x7.5 Propeller Efficiency (Not Chosen Propeller) [2]

Even though many candidate propellers were found to have high efficiencies at specific advance ratios, adjusting the angular velocity value through an iterative process led to many propellers dropping efficiency due to necessarily operating outside their preferred advance ratio range. Furthermore, some propellers were discounted due to the fact that they were sold only for one direction of rotation. Since a multicopter of this type is better off with two directions of rotation, only those sold in both directions were considered.

For an example of one propeller analysis, the 9x7.5 propeller above operates at its highest efficiency of 0.74 at an advance ratio around 0.76. However, spinning at an RPM to produce this advance ratio produces too much thrust, around 3 newtons per propeller. With two propellers producing 6N and a drag of only around 2.2 to 2.4N, the propeller will accelerate the aircraft into a higher advance ratio regime, dropping its efficiency. To match the force of drag, the RPM is lowered, the advance ratio adjusted, and the new thrust computed. This is repeated until the thrust is approximately in the desired range of 1.1 to 1.2 newtons, at which point the new C_p value results in 77 Watts

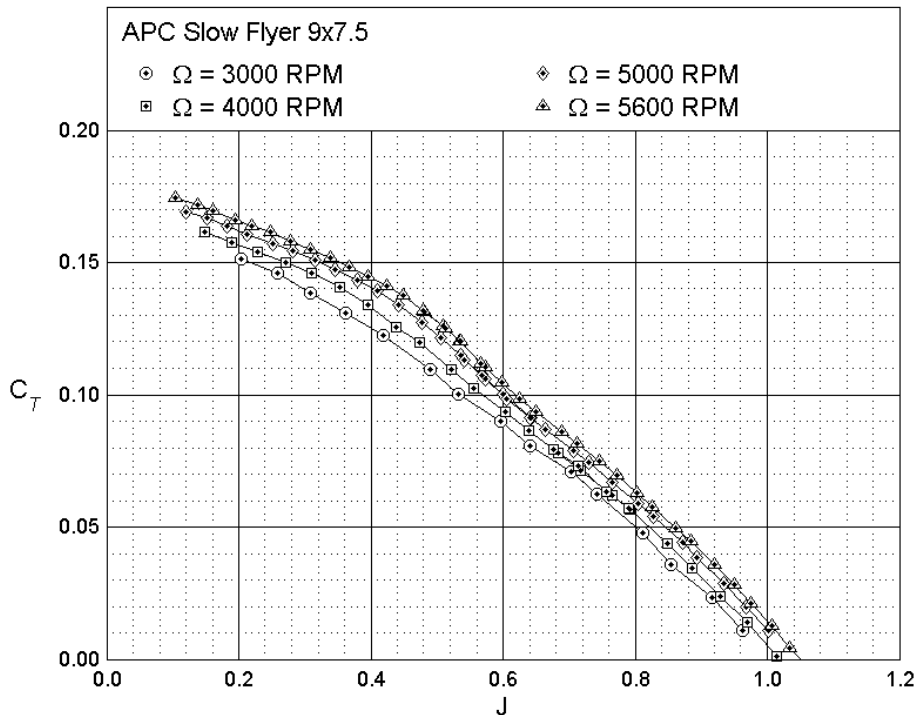


Figure 4.4: APC Slow Flyer 9x7.5 Propeller Thrust (Not Chosen Propeller) [2]

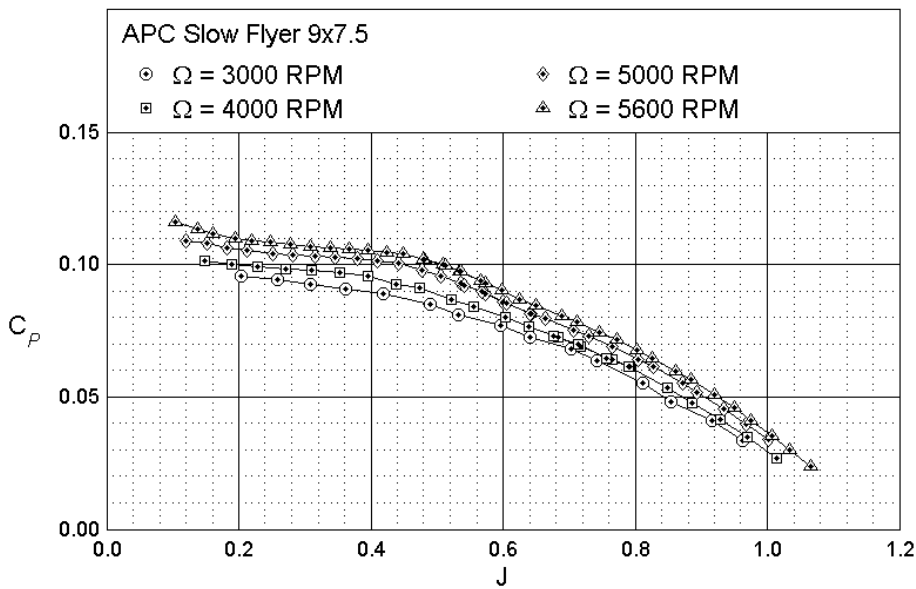


Figure 4.5: APC Slow Flyer 9x7.5 Propeller Power (Not Chosen Propeller) [2]

of power transferred to the air with 47.6 Watts being useful work ($P = TV$), dropping the efficiency to 0.62. Multiple propellers were run through this process, with the following table illustrating their compared efficiencies at the

correct thrust balance. Finally, ω is adjusted to compute the efficiency in hover mode, the other power-hungry mission segment. Assuming a stationary hover, the induced velocity of the propeller is calculated from thrust T by

$$V_i = \sqrt{\frac{T}{2\rho S_r}} \quad (4.3.9)$$

where S_r is the rotor disk area, using actuator disk theory as described in Chapter 1. Thus the advance ratio can be recalculated based on the induced velocity for the diameter of the propeller and thrust required to hover, $\frac{W_0}{3}$. For instance, a 10 inch propeller will produce an induced velocity of 8.9 meters per second to produce enough thrust to hover at sea level. This informs the advance ratio in hover, which, after iteration like for cruise, was intuitively found to be much lower: 0.28 for the 10 inch propeller and around 0.31 for the 9 inch propellers. At lower advance ratios, the values of C_t are larger, but the efficiency drops. After finding C_t and C_p for this hover advance ratio, the power and efficiency are extracted and compared. Note that the lower diameter propellers use much more power to hover, due to the fact that they induce a larger velocity at the actuator disk in order to produce sufficient thrust. Furthermore it can be seen that lower pitch of propeller consumes less power in hover. Table 4.2 below shows some of the propellers that made it to the final round of analysis for selection:

Table 4.2: Propeller Final Selection Table

| Propeller | 8x6 SF | 9x6 SF | 9x7.5 SF | 9x9 E | 10x10 E |
|--------------------------------------|---------|---------|----------|---------|---------|
| Optimal Advance Ratio | 0.704 | 0.625 | 0.711 | 0.782 | 0.845 |
| Cruise Iterated Advance Ratio | 0.765 | 0.745 | 0.823 | 0.869 | 0.949 |
| Cruise Iterated Efficiency | 0.735 | 0.689 | 0.617 | 0.711 | 0.756 |
| Cruise RPM | 6900 | 6300 | 5700 | 5400 | 4450 |
| Cruise Torque (NM) | 0.088 | 0.053 | 0.065 | 0.053 | 0.060 |
| Hover Iterated Advance Ratio | 0.288 | 0.317 | 0.335 | 0.319 | 0.284 |
| Hover Iterated Efficiency | 0.441 | 0.528 | 0.469 | 0.428 | 0.447 |
| Hover RPM | 11500 | 9300 | 8800 | 9250 | 7450 |
| Hover Torque (NM) | 0.207 | 0.215 | 0.256 | 0.264 | 0.112 |
| P_{shaft} Cruise, 2 Props (W) | 63.226 | 69.378 | 77.075 | 60.073 | 55.898 |
| P_{shaft} Hover, 3 Rotors (W) | 746.414 | 627.682 | 709.052 | 765.840 | 587.976 |
| Hover Shaft Energy 120s (J) | 89569 | 75321 | 85086 | 91900 | 70557 |
| Cruise Shaft Energy 3480s (J) | 220,025 | 241,435 | 268,222 | 209,056 | 194,527 |
| Motor Efficiency | 0.79 | 0.79 | 0.79 | 0.79 | 0.79 |
| Mission Total Energy (Wh) | 108.86 | 111.38 | 124.23 | 105.82 | 93.21 |

The choice of propeller was ultimately the APC 10x10 electric, which provided the highest efficiency in cruise due to its high pitch and reasonable efficiency in hover. Overall, it results in the least total mission energy expended by the battery.

Now that a preferred propeller has been selected, a motor was matched to it through torque matching. The power of the propeller at cruise conditions

was divided by the angular rate to obtain the torque required by the propeller. Using the characterization of the motor with I_0 , R , and K_v , the desired voltage can be calculated to obtain the target ω and torque:

$$V = \left(\frac{2\pi K_v \tau_t}{60} + I_0 \right) R + \frac{\omega_t}{K_v} \quad (4.3.10)$$

where τ_t and ω_t are the target torque and angular velocities in newton meters and rotations per minute, respectively. This is simply a rearranging of the equations used to compute efficiency and torque of the motors as a function of angular velocity and input voltage.

From here, the efficiency is recalculated, and multiple motors are compared at the throttle point at which they satisfy the angular velocity and torque requirement of the propeller in steady state. All motor considerations are listed in table 4.3.1.

Table 4.3: Motor Selection Table

| Motor | Cruise Throttle | Hover Throttle | Cruise η | Hover η |
|--------------------|-----------------|----------------|---------------|--------------|
| BH 3110 730Kv | 0.300 | 0.504 | 0.790 | 0.840 |
| BH 3110 900Kv | 0.247 | 0.415 | 0.765 | 0.820 |
| BH 2810 1180Kv | 0.194 | 0.327 | 0.773 | 0.812 |
| BH 2812 1115Kv | 0.200 | 0.335 | 0.757 | 0.815 |
| BH 2812 900Kv | 0.249 | 0.418 | 0.767 | 0.818 |
| BH 3008 1150Kv | 0.200 | 0.336 | 0.745 | 0.795 |
| BH 3008 1300Kv | 0.195 | 0.327 | 0.738 | 0.802 |
| Tmotor 3116 400Kv | 0.521 | 0.874 | 0.778 | 0.853 |
| Tmotor 3115 640Kv | 0.329 | 0.550 | 0.748 | 0.831 |
| Tmotor 3115 900Kv | 0.235 | 0.394 | 0.741 | 0.825 |
| Tmotor 3115 1050Kv | 0.204 | 0.341 | 0.737 | 0.818 |

From here, the Brother Hobby 3110 stator size, 730 K_v motor was selected. This produces the highest efficiency in hover and cruise by torque matching with the chosen propeller to meet the thrust requirements in each regime. Furthermore, the large stator diameter and considerable stator height are consistent with motors commonly used for cinematic drones of this weight class.

This motor requires approximately 30% throttle in cruise and 50% throttle in hover, which yields a reasonably large margin for excess power that is available for fast hover climbing or for use by the control algorithm which preferably does not top out the motor power. The motor efficiency in cruise is shown in Figure 4.6 at the proper throttle point. Evidently, the motor is operating near its peak efficiency, which is why it was chosen over numerous other choices.

While the selected propeller's actual geometry is difficult to discern, an XROTOR model of a similarly performing propeller was created for SUAVE simulations. This produced more accurate energy network simulation, and the efficiencies were similar to those seen in empirical data of the chosen propeller as described in the SUAVE results section. This propeller was designed us-

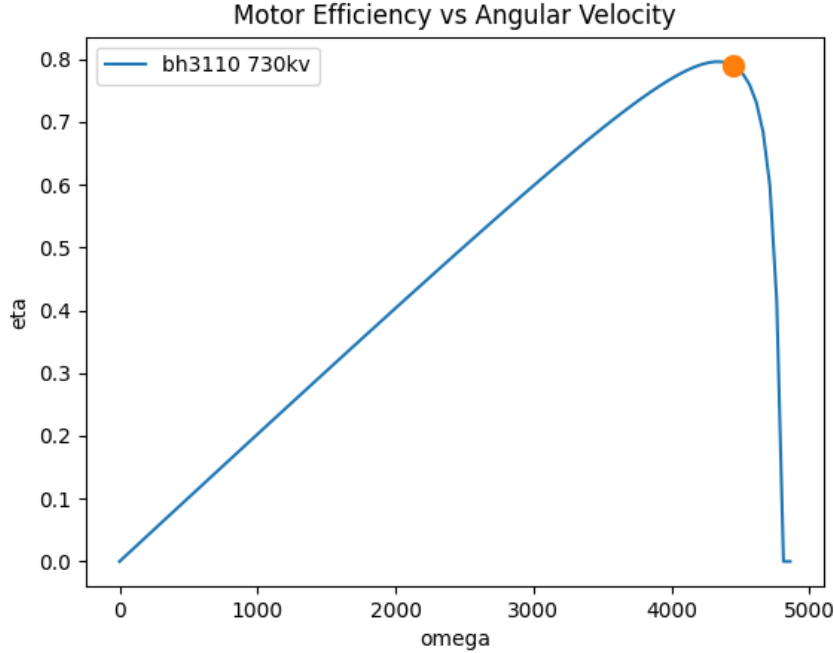


Figure 4.6: Cruise Condition Motor Efficiency Plot. Orange Dot Indicates Operational Point at 29.99% Throttle Voltage.

ing the operating point to match drag, as described previously. The resulting values of C_t and C_p were similar to those of the APC propeller selected, validating the propeller in SUAVE simulation even further. Figure 4.7 depicts the propeller used in simulation, as the propeller in SUAVE was constructed with the same parameters as the XROTOR generation.

4.3.2 Battery Selection

The battery sizing script for Iteration 3 suggested a battery around the size of 6500 mAh. This battery size was preferred partially because a specific vendor sell a high-voltage version of this battery that is technically still 6 cells but operates at slightly higher voltage allowing it to have a higher energy density. While most LiPo batteries have energy densities around 150 to 200 Wh per kilogram, the battery mentioned has a 205 Wh per kilogram energy density. This battery size was then revalidated using the Mission Total Energy in table 4.2. With energy consumption estimated at around 93 to 100 Wh in cruise and hover only, plus the fact that energy would be expended during climb and landing, the battery size using this energy statistic was estimated between 6000 and 6500 mAh. This was assuming around 80% of the capacity was usable so as to not damage the battery. For reference, $E = C_{bat}V_{bat}$, where energy of the battery is equal to its charge capacity multiplied by its voltage.

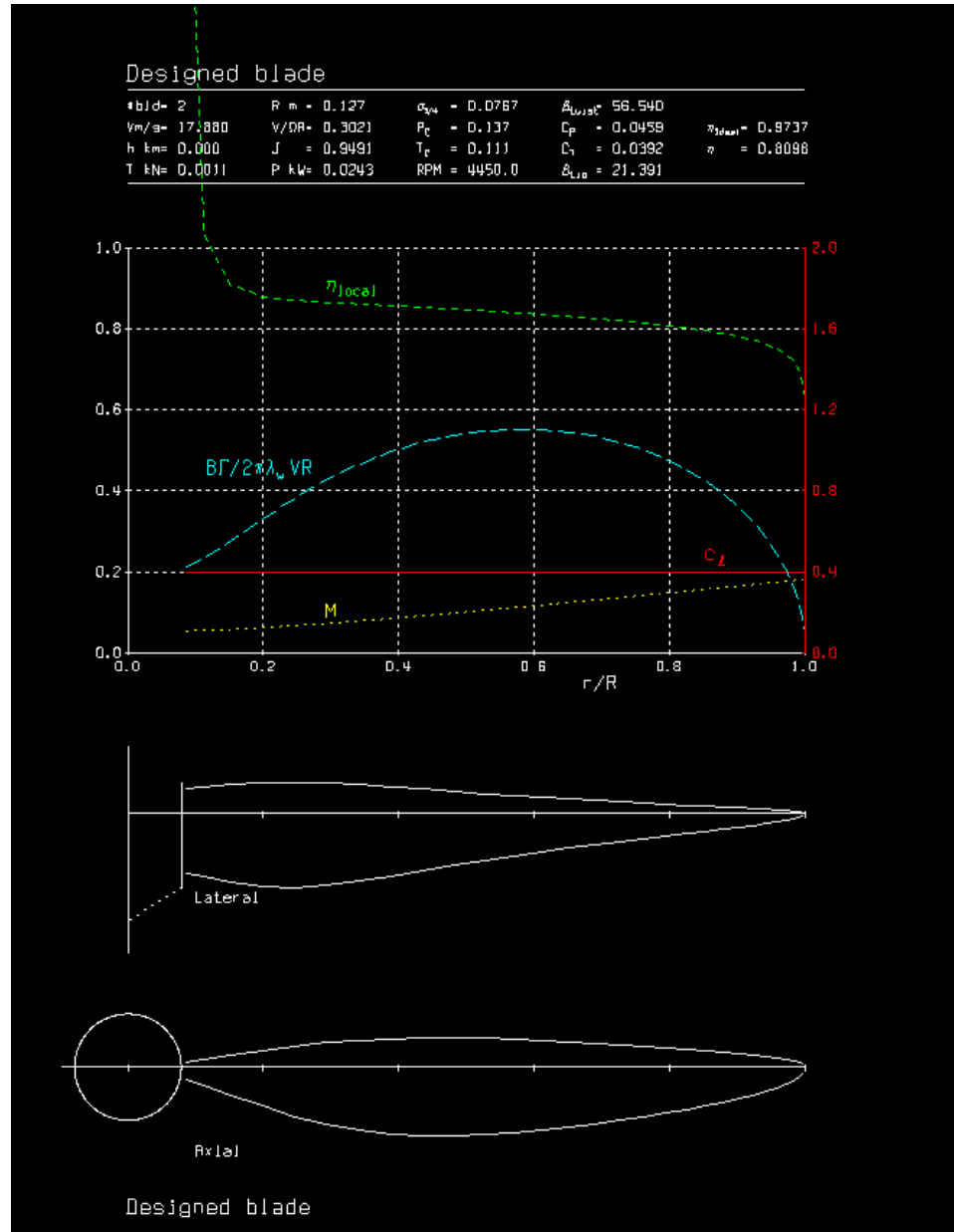


Figure 4.7: XROTOR Model of a Propeller Similar to the Off the Shelf Selected Propeller: APC 10x10E.

4.4 SUAVE Optimization and Major Planform Changes

SUAVE contains a built-in optimizer that accepts input parameters, an objective function, and constraints. It then runs a SciPy optimizer algorithm that attempts to perturb the parameters to find a global minimum in the objective function within the boundaries of the constraints. SUAVE's built-in optimizer package was implemented for VTOL MK2, but results were ultimately not promising.

The optimization is split into multiple classes instead of one mission analysis class. The Procedure scripts drives the optimization problem, accepting a mission, setting up analyses, and defining sizing scripts for the aircraft configuration after parameters are perturbed. The Procedure script also correlates specific mission characteristics to optimization constraints and objectives. In

this case, the drag coefficient was correlated to the objective variable of drag coefficient, which was minimized by the optimizer. The "Optimize" script ran the problem and defined the constraints, objective, and parameters. A constraint was placed upon the battery fraction consumed of less than 80%, such that the battery was not drained below a damaging level. The problem objective was the aforementioned drag coefficient. Wing area, taper ratio, and sweep were independently used as the parameter being changed, and combinations of the variables were also attempted. Scaling of the parameters, objective, and constraints were such that the optimizer was operating on order one.

SUAVE optimization problems were attempted, but the optimizer always changed the parameters to values extremely close to the input initial parameter values. This indicates that the design space is either extremely flat where the derivatives of the objective with respect to the parameters are very low, or the optimizer was not operating correctly. The design was required to move on due to design constraints, so the optimizer was put on hold for this project in favor of running manual sweeps of each parameter.

First, since airfoil had been chosen, the C_L and therefore reference area S were tested over a range of values, with cruise segment $\frac{L}{D}$ representing the dependent variable. Two methods were used: analysis of the entire aircraft including fuselage and tail, and analysis of wing aerodynamics only. A script was added to the SUAVE analysis to perform this sweep. The former is shown in Figure 4.8, and the latter is shown in Figure 4.9. A more refined version of the latter is depicted in Figure 4.10. During the C_L sweep, taper ratio of a trapezoidal wing was held constant at 0.5. The results indicate that when optimizing for the full vehicle, a C_L of 0.57 is optimal, with a resulting S_{ref} of 0.268 square meters. This configuration was run, and the actual C_L was reported as 0.55, somewhat lower than the input value, possibly due to some thrust being vectored downward at nonzero angle of attack. The whole-aircraft C_L sweep led to an $\frac{L}{D}$ of 12.523. Analyzing the wing only led to an optimal choice of C_L of 0.533 and S_{ref} of 0.287 square meters. Running this configuration resulted in an actual C_L of 0.517 and $\frac{L}{D}$ equal to 12.654. The more promising result of the wing-only analysis led to the decision to forego the whole-aircraft analysis.

Next, the same code was used to run a range of taper ratios to determine the optimal point. To obtain as close to an elliptic distribution as possible, a taper ratio of 0.4 is theoretically and experimentally approximates an elliptic lift distribution along the wing, minimizing induced drag for a trapezoidal wing at low Reynolds numbers [3]. When SUAVE computes parasitic drag, it reports less wing surface area and thus lower C_{D0} for a lower taper ratio. This effect may be because the thickness of the wing is accounted for in computation of wetted area, so shifting toward a triangular wing reduces wetted area marginally. Since SUAVE computes total drag, it adds parasitic and induced drag, such that $\frac{L}{D}$ is maximized at lower taper ratios than the induced drag only consideration. Figure 4.11 shows the sweep of taper ratios, with efficiency

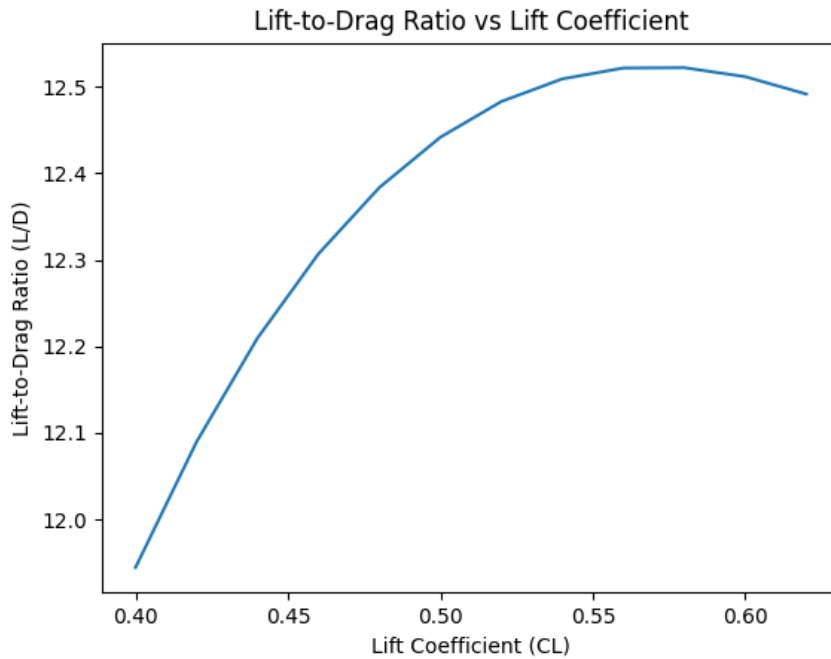


Figure 4.8: Sweep of $\frac{L}{D}$ vs C_L , Analysis Conducted Simulating Entire Aircraft.

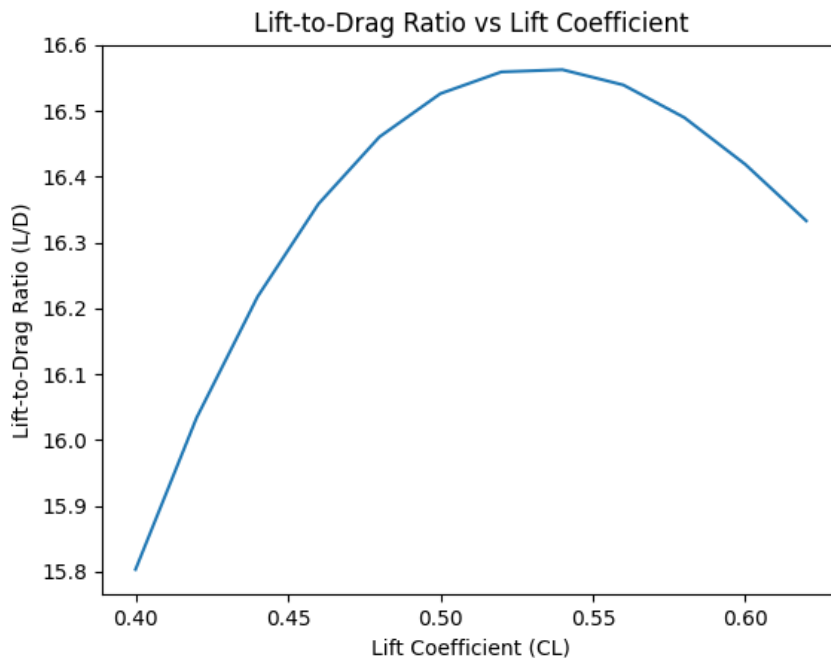


Figure 4.9: Sweep of $\frac{L}{D}$ vs C_L for Wing Only, Coarse Resolution.

maximizing at taper ratios closer to 0.25. However, taper ratio was selected to be closer to the minimum induced drag case of 0.4 out of skepticism of SUAVE's wetted area calculation and mechanical constraints. In order to fit a spar through the outboard wingtip, the thickness of the wing was required to be greater than 1 cm, so the taper ratio lower bound was 0.4. Taper ratio was attempted to be optimized using OpenAeroStruct as described in the next section, but ultimately the value of 0.4 provided high enough efficiency to compensate for the mechanical requirement.

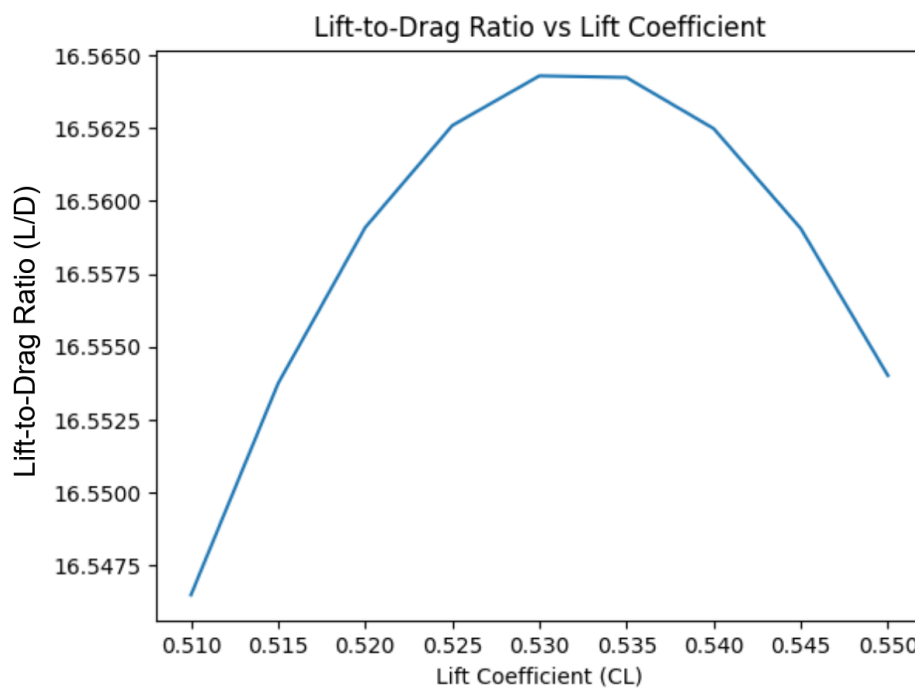


Figure 4.10: Sweep of $\frac{L}{D}$ vs C_L for Wing Only, Refined Resolution.

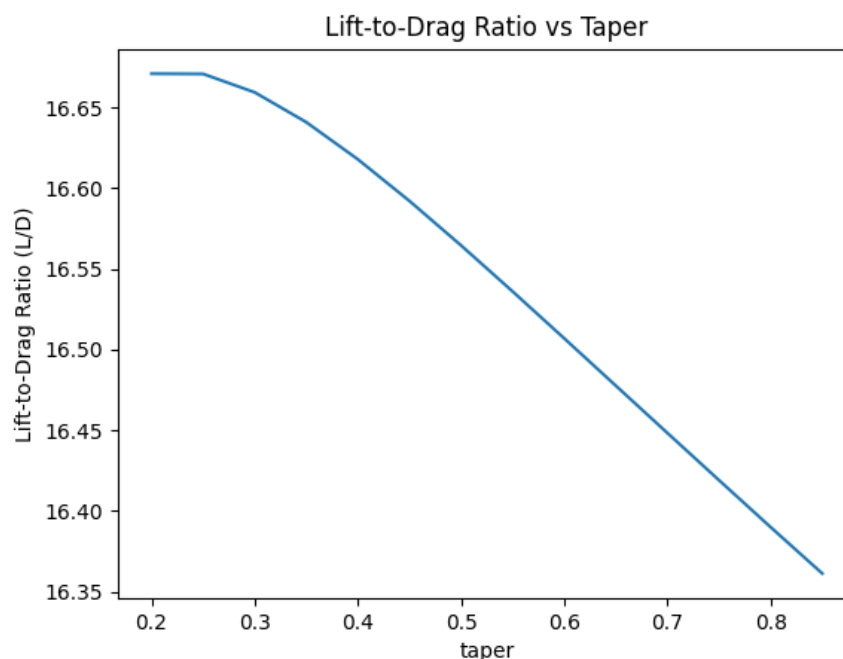


Figure 4.11: Sweep of $\frac{L}{D}$ vs taper ratio for Wing Only

4.4.1 Final Tail Configuration

Using the result of the tail parasitic drag minimizer from Chapter 3, the tail parameters were recomputed. The tail area was further reduced by relaxing the tail volume horizontal coefficient to 0.8 and the vertical coefficient to 0.07, closer to those of a twin engine general aviation aircraft. The final details are given in Table 4.4.1.

Table 4.4: Final Tail Parameters

| | |
|----------------------------|--------|
| Optimal Lever Arm (m) | 0.7 |
| Horizontal Vol Coefficient | 0.8 |
| Vertical Vol Coefficient | 0.07 |
| Horizontal Area (m^2) | 0.0585 |
| Vertical Area (m^2) | 0.0461 |
| Total Area (m^2) | 0.0745 |
| Dihedral (deg) | 38.22 |
| Root chord (m) | 0.16 |
| Taper | 0.5 |
| Tip Chord (m) | 0.08 |

4.5 OpenAeroStruct Drag Minimization

Induced drag is caused by local downwash changing the angle of attack such that the lift vector tilts rearward on an airfoil. The minimum induced drag for a 3D planform comes from an elliptical lift distribution across the span of the wing, such that the downwash is constant. For the purpose of this UAV, wing parameters were altered to achieve low drag in order to increase the lift to drag ratio. One method attempted was induced drag minimization using OpenAeroStruct developed by MDO Lab at University of Michigan.

OpenAeroStruct interfaces with OpenVSP through python, and an example code was altered in order to take an input wing and optimize its chord or twist distribution to find a minimum drag configuration. First, a zero-twist example was optimized for taper ratio, and the taper ratio that was closest to an elliptic lift distribution was 0.49. However, implementing a viscous parasitic drag with OpenAeroStruct's geometry optimization failed, so the result was discarded in favor of the SUAVE sweep method.

With taper set at 0.4, the twist along the wing was attempted to be optimized to closer resemble an elliptic lift distribution. Using OpenAeroStruct, the parameters were defined as nine individual twist angles linearly spaced along the wing sectioned into eight segments per side. The result was as expected, where washout near the wingtip decreased local section lift to zero, and the inboard sections experienced lower angles of attack to flatten out the lift distribution produced by a trapezoidal wing. The section twists counting from root to tip are listed in Table 4.5.

This twist distribution minimized inviscid drag according to the vortex lattice method used by OpenAeroStruct with C_{D0} set to 0. However, running OpenVSP on the wings shows that the twist distribution makes minimal difference in induced drag despite being closer to an elliptic distribution. The taper ratio of 0.4 already achieves a lift distribution quite close to elliptic. Figure 4.12 depicts the comparison of the OpenVSP analysis of the wing loading prior to and after the OpenAeroStruct optimization. At the cruise C_L , the C_{Di} induced drag coefficient is 0.00952 for the zero-twist wing and 0.00947 for the optimized-twist wing according to OpenVSP. This gain is quite negligi-

Table 4.5: Optimized Twist Angles using OpenAeroStruct on Trapezoidal Wing, 8 Segments

| section | angle (degrees) |
|--------------------|-----------------|
| 0 | 0 |
| 1 | 0.6826811196 |
| 2 | 0.8201132906 |
| 3 | 1.041543391 |
| 4 | 1.112230609 |
| 5 | 1.085003168 |
| 6 | 0.7878173366 |
| 7 | 0.1705077801 |
| 8 | -1.926143102 |
| wing aoa in cruise | 3.332533964 |

ble, showing that taper already achieves a high Oswald's efficiency. Figures 4.13 and 4.14 show the output of the OpenAeroStruct optimizer, with a twist distribution that closer approximates elliptic loading.

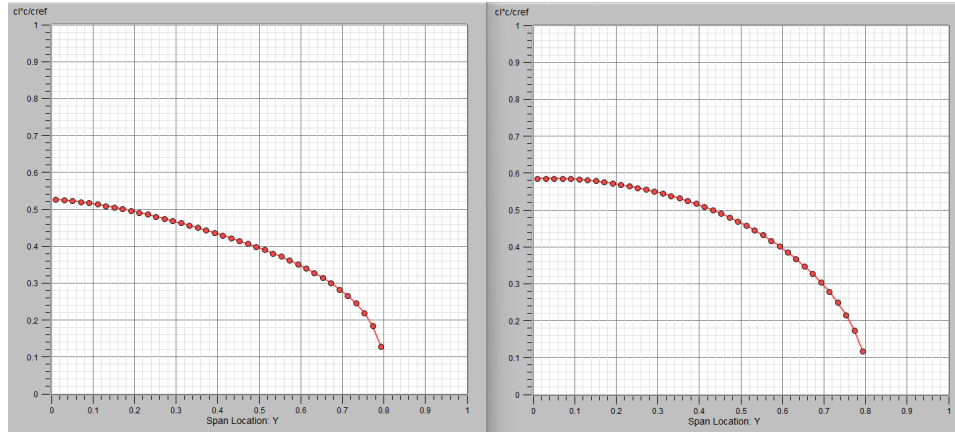


Figure 4.12: Comparison of Zero Twist (left) and Optimized Twist (right) Tapered Wing Loading Distribution.

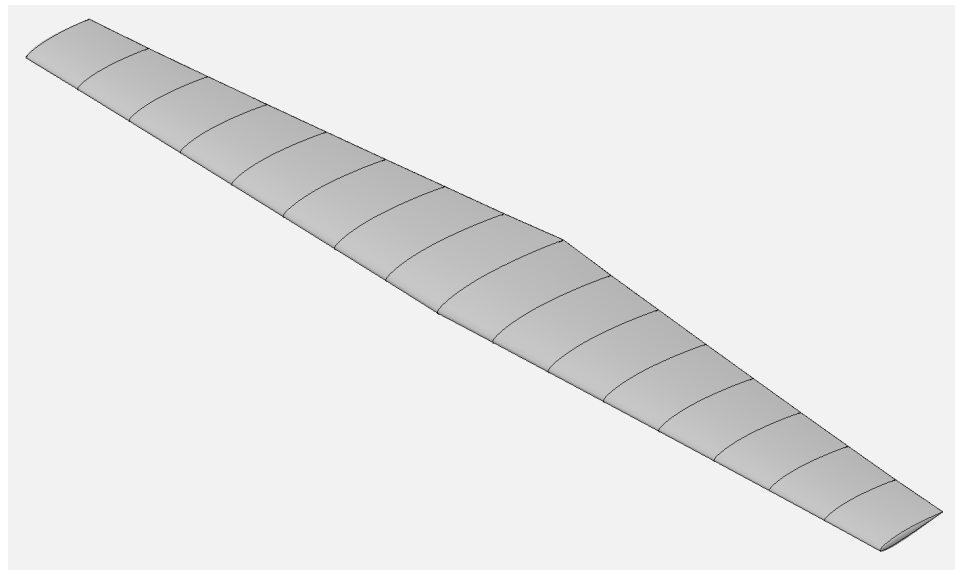


Figure 4.13: Optimized Twist Wing

Furthermore, when running SUAVE simulations using the zero twist and

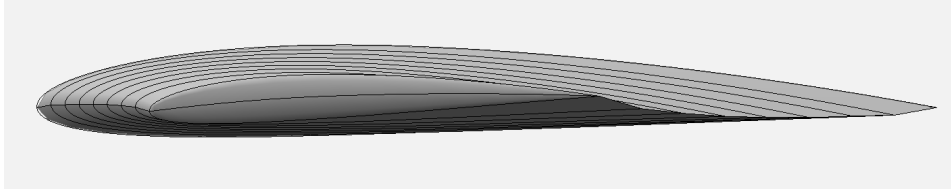


Figure 4.14: Optimized Twist Wing from Side View

optimal twist wings, the results show higher $\frac{L}{D}$ for the zero-twist result. This is where inconsistencies in design optimization become apparent. While the wing was being optimized alone in OpenAeroStruct, the simulation of the entire aircraft resulted in marginally lower efficiency. SUAVE allows for a high resolution of vortex lattice discretizations, and 40 spanwise and 25 chordwise segments were implemented. However, OpenAeroStruct has no easy control of VLM resolution to the knowledge of the author, so its modeling may have been quite different than that of SUAVE. Ultimately, it was decided upon to remain with a zero twist wing to remain consistent with the use of SUAVE as a source of truth in simulation. Furthermore, OpenVSP showed that the gain in induced drag is quite negligible, and mechanical considerations of fitting a rigid straight spar through the wing then increased in relative importance.

Small angles of wing sweep was tested briefly with OpenVSP, and it was discovered to have a weak positive effect on efficiency, but the tradeoff was undesirable, as wing sweep introduces mechanical complexity due to necessitating a split spar in the center of the aircraft. This requires much stronger wing box components that increase the structural weight of the aircraft. Thus, the wing quarter chord sweep was zero degrees. For the same mechanical spar reason, the wing was given no dihedral and thus relied on its high-wing position for roll stability.

4.6 Final Configuration SUAVE Results

Due to issues with the blade element method model stalling when all segments are considered, the SUAVE simulation was run with the original choice of propeller for mission analysis aerodynamics which did not depend on energy network. The analysis of the energy network and power in cruise was independently analyzed with a model that included a propeller very similar to the one chosen. Thus, Figure 4.20 shows the efficiency of the chosen motor and propeller in the cruise segment only. Note that in the simulation with a similar propeller to the one selected, the efficiency of the propeller increased in the cruise segment to approximately 75% which is precisely the efficiency extracted from empirical data. The motor efficiency in SUAVE exceeds 75%, which is predicted by the motor characterization operating at this cruise condition.

Figure 4.15 shows the expected lift and drag on this configuration, which leads to a higher $\frac{L}{D}$ of 12.76 as seen in Figure 4.16, as a result of the parameter optimization. Again, SUAVE underestimates $\frac{L}{D}$ compared to OpenVSP, so it

is assumed to be a conservative value. With the selected propeller, Figure 4.22 shows higher efficiency and higher motor efficiency than previous iterations. Note that the battery in this iteration was required to be oversized for the simulation to work properly. Nevertheless the energy consumption remains as expected. Note that energy consumption is close to what was anticipated by the propeller analysis. By just estimating the drag and already being close to an optimal point, the propeller analysis led to a 93 Wh consumption in cruise, while the actual aircraft with some optimized parameters consumed 87 Wh in the cruise segment. Running the same aircraft in SUAVE with the properly selected propeller and motor yields an even higher $\frac{L}{D}$ of 13.0003 as the final configuration efficiency. Once again, it should be noted that SUAVE underestimates efficiency compared to OpenVSP, which regularly estimates 17 and above for this aircraft. To be conservative, SUAVE remained the source of truth throughout this project such that the battery would be sufficient to complete the mission rather than fall short. Nevertheless, discrepancies like this point to the use of higher fidelity methods to validate or a deep dive into the source analyses of both softwares to find the discrepancy in drag estimation.

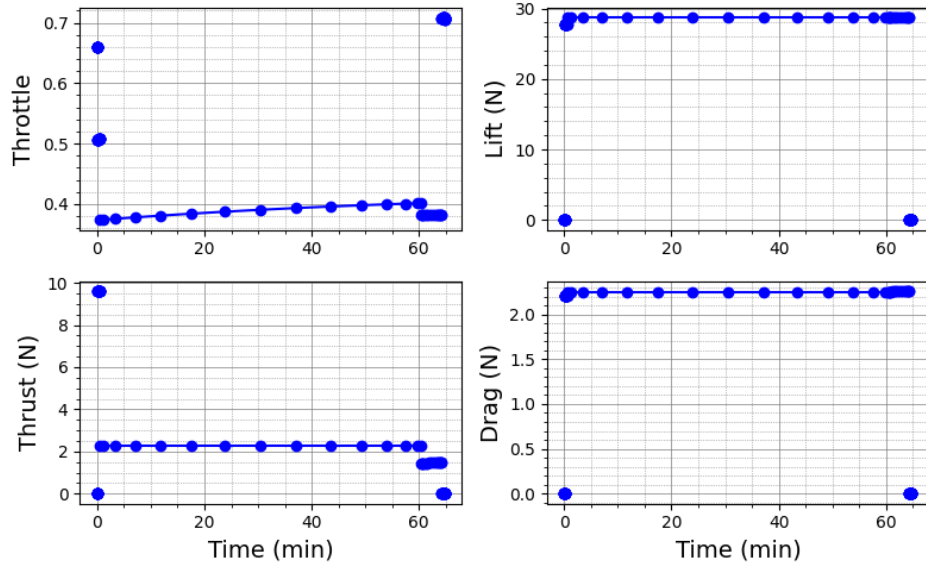


Figure 4.15: Iteration 3 Aerodynamic Forces

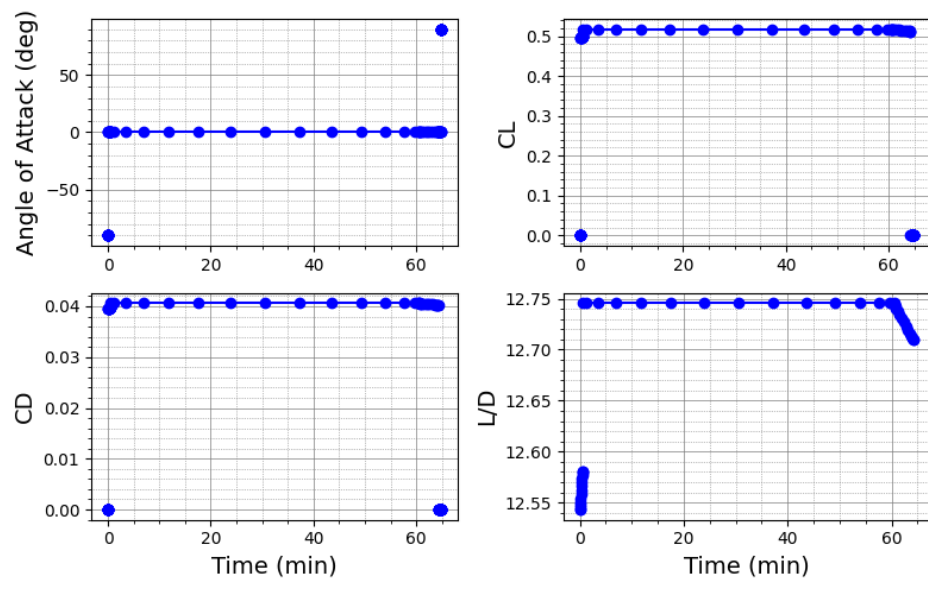


Figure 4.16: Iteration 3 Aerodynamic Coefficients

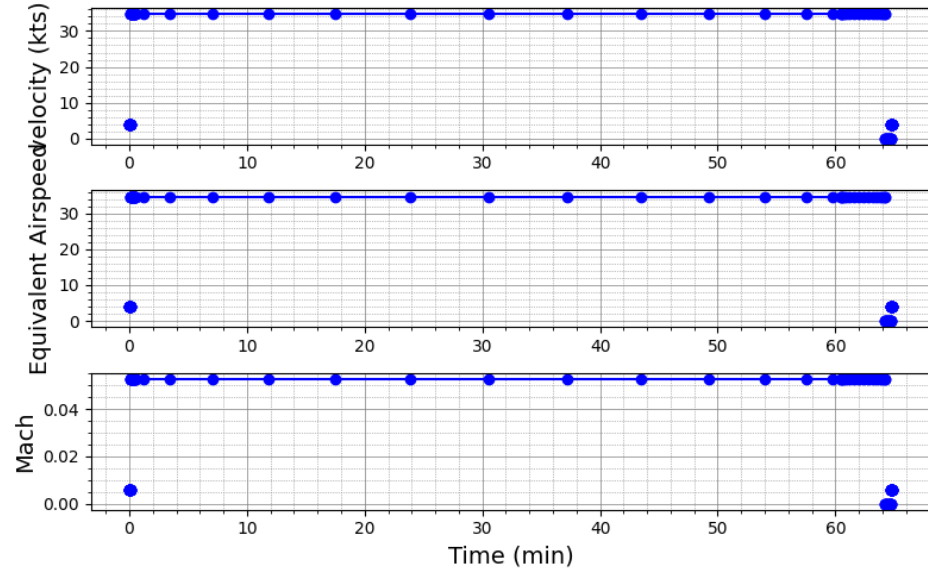


Figure 4.17: Iteration 3 Velocities

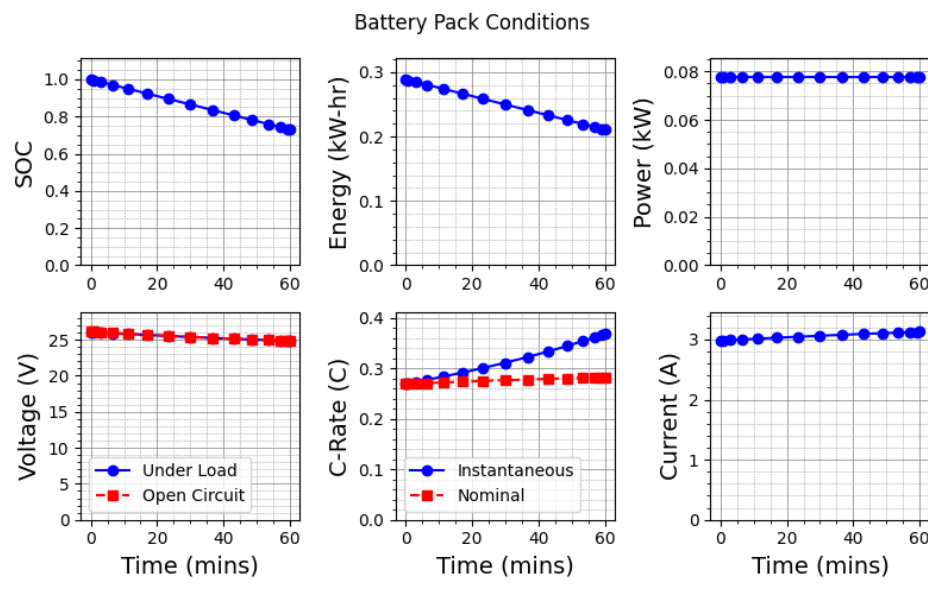


Figure 4.18: Iteration 3 Battery Conditions for Cruise Segment Only (With Updated Propeller). Note oversized battery for SUAVE to converge correctly

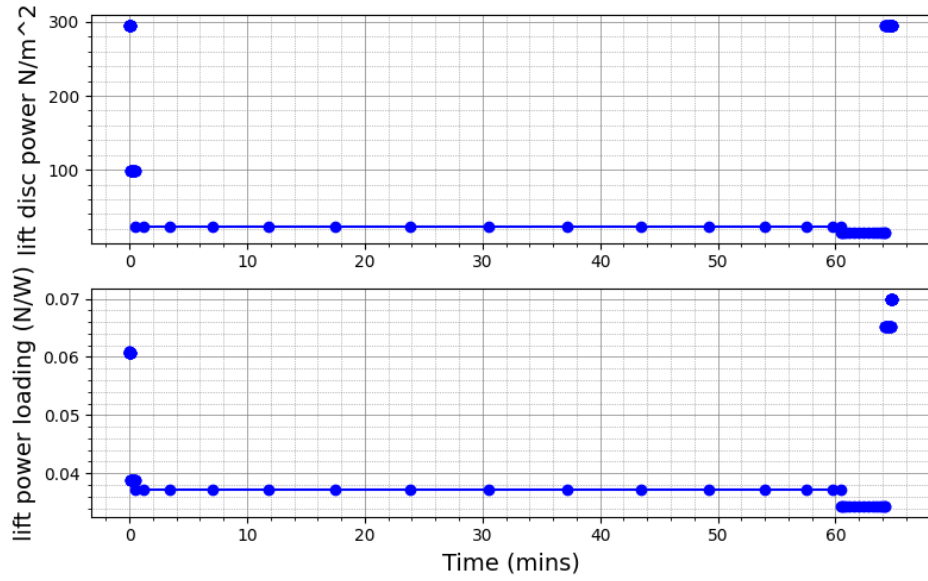


Figure 4.19: Iteration 3 Disc Power Loading

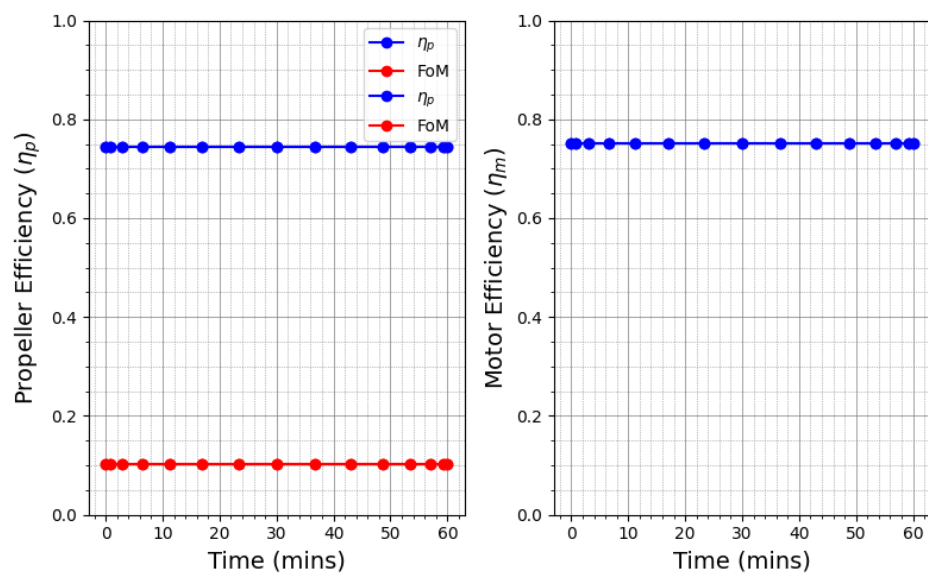


Figure 4.20: Iteration 3 Electric Motor Performance in Cruise

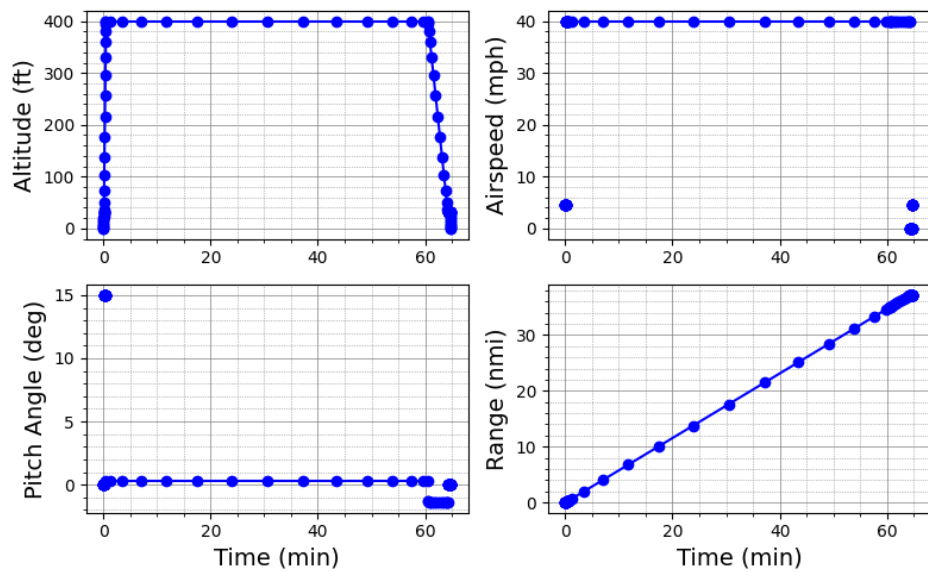


Figure 4.21: Iteration 3 Flight Conditions

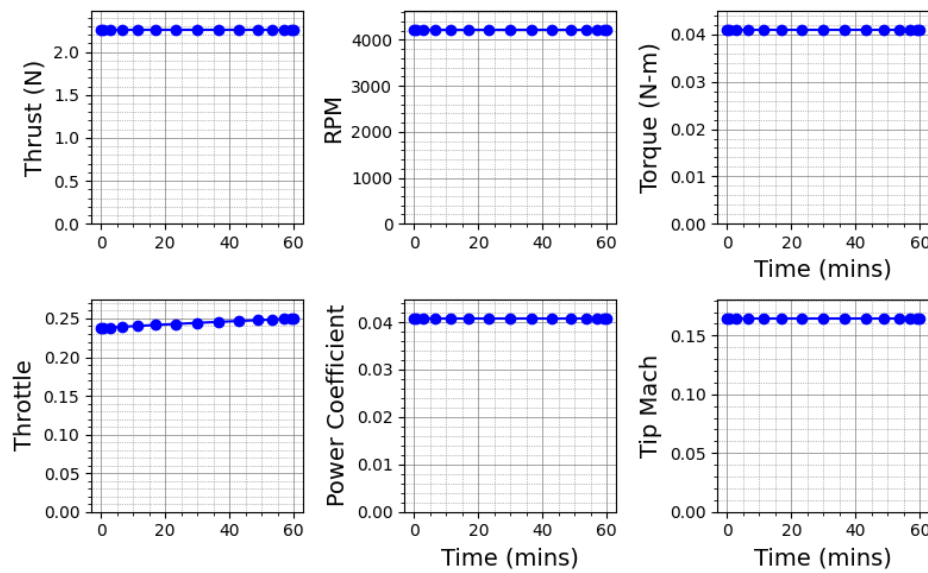


Figure 4.22: Iteration 3 Propeller Performance in Cruise

The final configuration is shown in Figures 4.23, 4.24, 4.25, and 4.26 using OpenVSP geometry. At this point, the model was ready to transition to Siemens NX for mechanical design of the components.

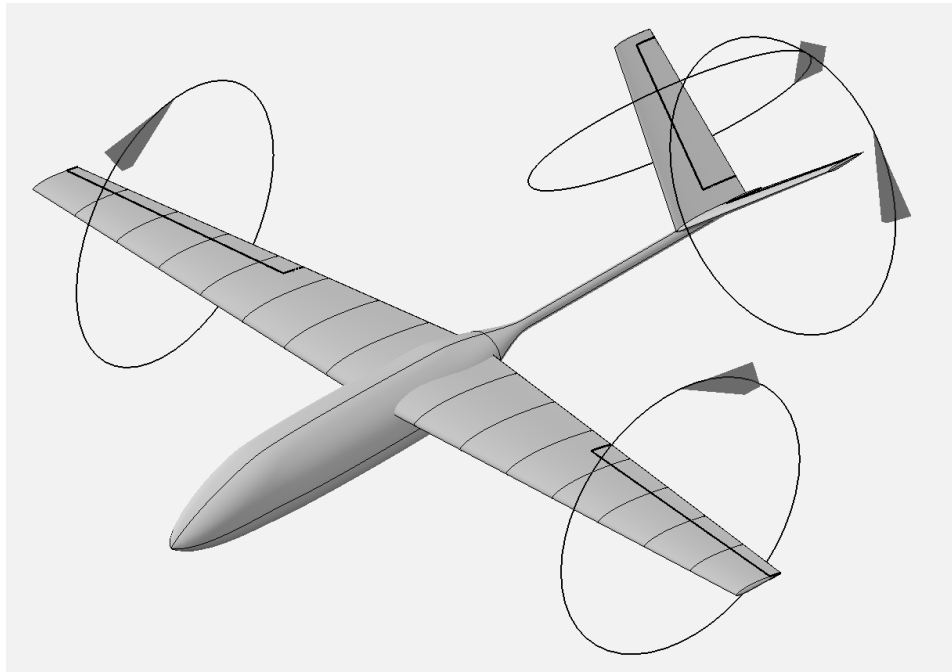


Figure 4.23: Final Configuration Iso View

4.6.1 Stability and Center of Mass

The center of mass plays a critical role in aircraft stability. To ensure longitudinal static stability, the center of mass is placed in front of the aircraft neutral point (X_{NP}) so that pitch perturbations result in a restoring moment.

Dynamic stability was left as a future exercise, but with the methods used, relatively high confidence is held in the fact that the aircraft will be dynamically stable when excited in its eigenmodes. This analysis is left as future

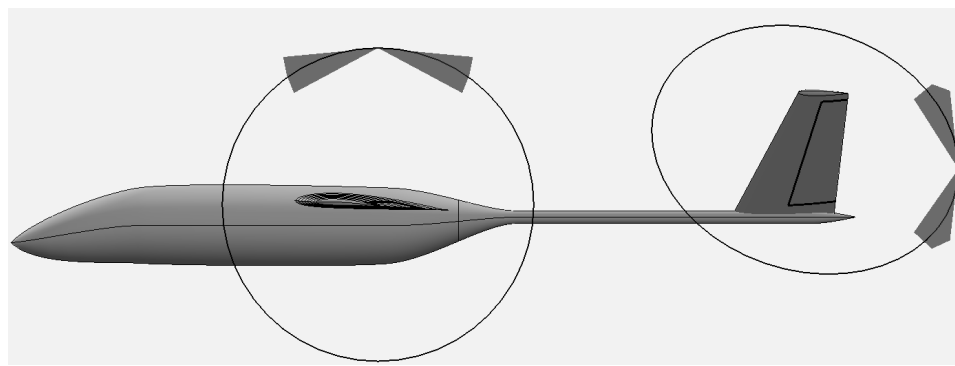


Figure 4.24: Final Configuration Side View

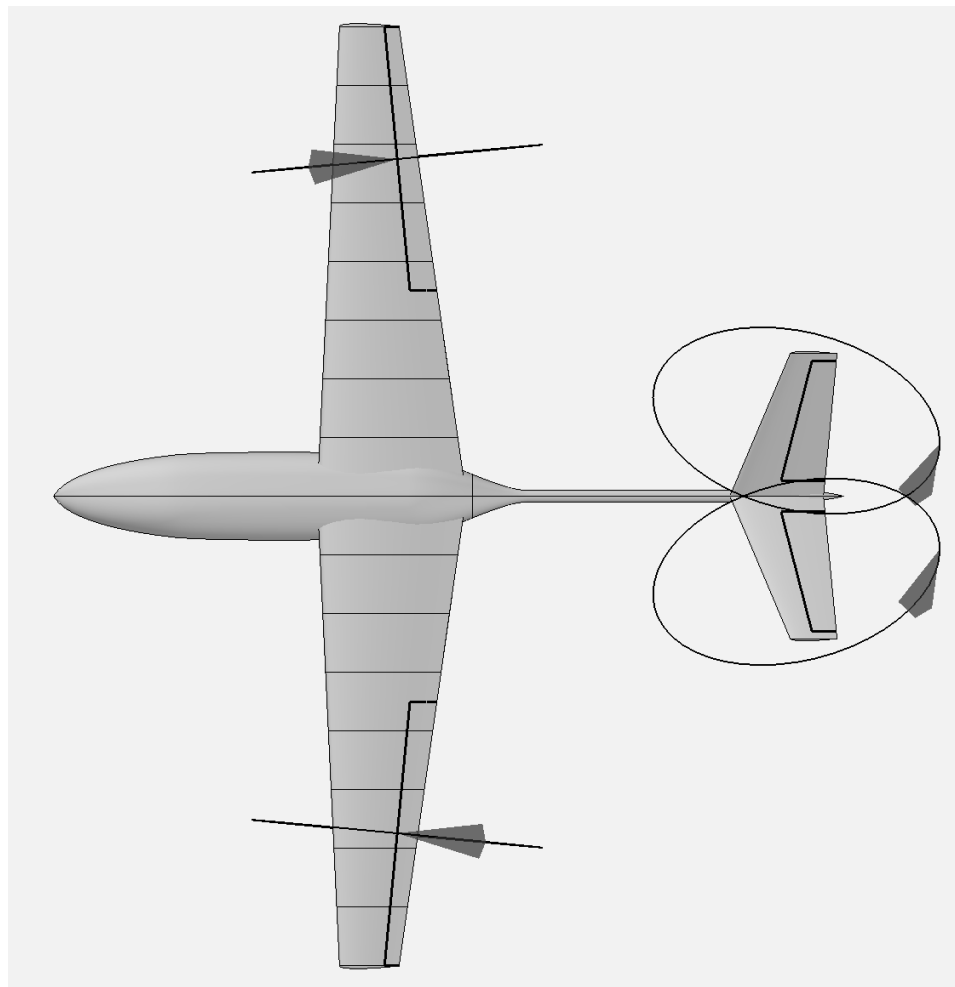


Figure 4.25: Final Configuration Top View

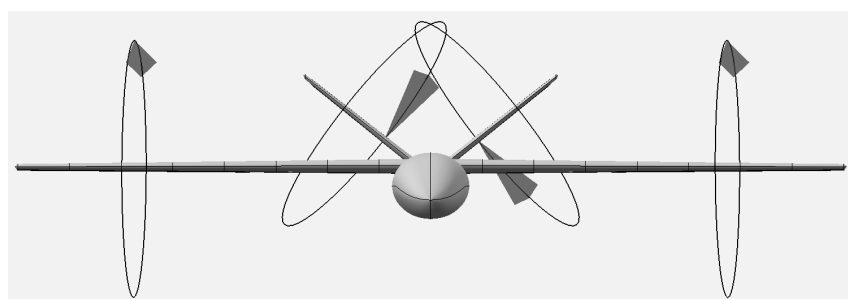


Figure 4.26: Final Configuration Front View

work.

As a brief summary, the neutral point of the aircraft is the point at which the moment becomes independent of angle of attack. Since the cambered

airfoil used on the main wing produces a pitch-down moment, a tail applies a pitch-up moment to trim the aircraft. If the neutral point is behind the center of mass, then C_{my} vs α has a negative slope, indicating a restoring moment when perturbed from equilibrium.

The neutral point was found using OpenVSP's pitch stability analysis feature in VSPAero. Stability margin is defined as $\frac{X_{NP} - X_{CG}}{MAC}$, where MAC is the mean aerodynamic chord, assuming the x-axis is longitudinal and positive x is toward the tail. With the neutral point at 0.1116m behind the wing root leading edge (origin), a 20% stability margin yields an X_{CG} of 0.074m behind the wing root leading edge. Then, a weight buildup of all components and their respective locations was constructed, and playing with the battery location until the center of mass was in the correct location yielded a battery position of 0.05m behind the wing root leading edge.

From here, the tail incidence angle was iterated until the moment about the CG reached zero at the correct cruise C_L . Running VSPAero with the wing and tail produced more reliable results than the full aircraft including fuselage. This was assumed valid since the fuselage does not contribute significantly to aerodynamic moments, as it is not a lifting surface. Figure 4.27 shows the stability curve of C_{my} vs C_L , and the zero-moment point lies at $C_L = 0.52$, approximately where the ideal cruise condition lies. This was achieved by tuning the tail incidence to 1.23 degrees pitch up, indicating that the tail has a slight pitch-down trim at the desired C_L .

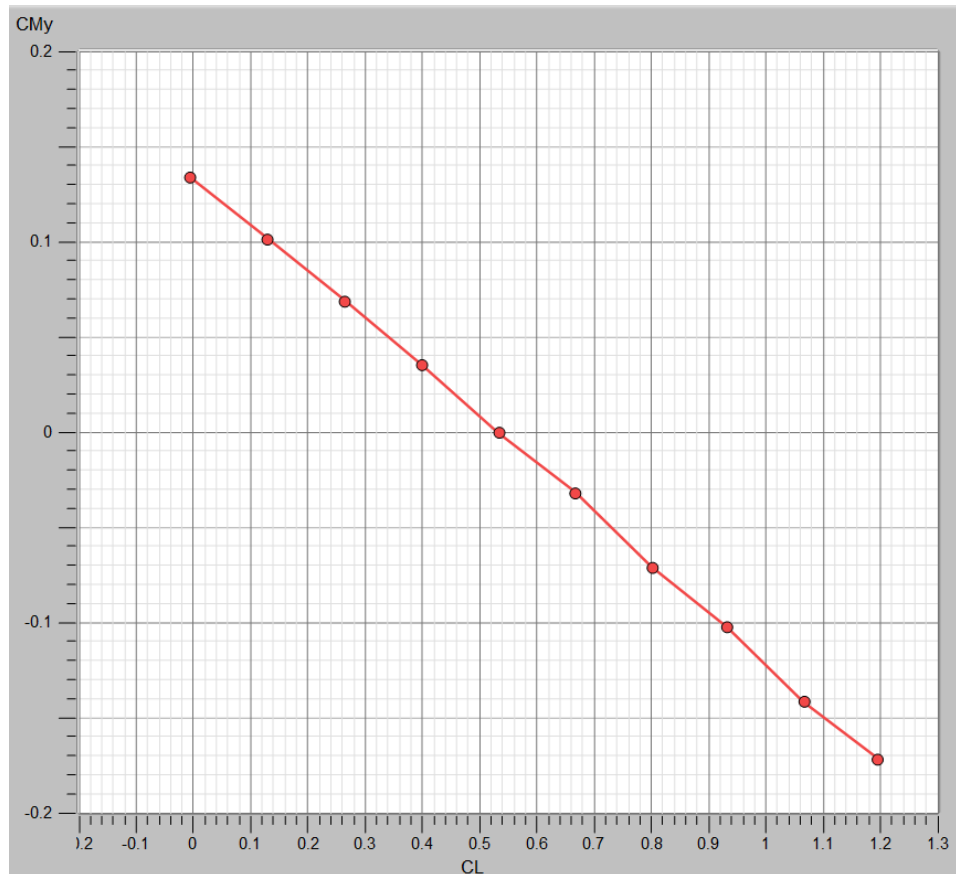


Figure 4.27: Stability Plot of C_{my} vs C_L , Showing Positive Static Margin

4.6.2 Iteration Comparison

The three major iterations represent increasing accuracy in terms of aircraft sizing. More accurate weight estimation led to a heavier aircraft in iteration 2 over iteration 1. Furthermore, the optimization efforts in Iteration 3 led to efficiency gains over iteration 2. Table 4.6.2 shows the comparison. Even though the initial iteration shows the lowest total energy expended, it is inaccurate in its weight approximation, as it represents an underweight aircraft and is too aggressive. Iterations 2 and 3 represent more accurate and conservative weight estimations, taking into account better models for the powerplant efficiency than iteration 1.

Table 4.6: Iteration Aerodynamics Comparison

| Coefficient | Iter 1 (Low Confidence) | iter 2 | iter 3 Old Prop | iter 3 New Prop |
|---------------------|-------------------------|---------|-----------------|-----------------|
| CL | 0.3938 | 0.3949 | 0.5174 | 0.5172 |
| CD | 0.0328 | 0.0326 | 0.0406 | 0.0398 |
| CD0 | 0.0208 | 0.0204 | 0.0244 | 0.0234 |
| CDi | 0.0114 | 0.0115 | 0.0154 | 0.0156 |
| L/D | 11.9886 | 12.1250 | 12.7455 | 13.0003 |
| Mission Energy (Wh) | 98.86 | 101.57 | 100.73 | 99.34 |

When comparing to OpenVSP's drag polar, the SUAVE result at the cruise condition is greater than that of OpenVSP, as OpenVSP predicts a C_D of 0.029 compared to SUAVE's C_L 0.040. OpenVSP features a lower parasitic drag estimation in its vortex lattice method solver, with C_D at $C_L = 0$ of 0.018 compared to the more accurate value of 0.024 through SUAVE's computation, which is validated when running OpenVSP's dedicated parasitic drag calculator, which predicts 0.023. Induced drag is also higher in SUAVE's estimate compared to OpenVSP, with values of 0.015 and 0.01, respectively. SUAVE's more accurate parasitic drag computation makes it more reliable than investigating C_{Dtot} vs C_L using OpenVSP. Overall, SUAVE may be operating more conservatively than OpenVSP. Figure 4.28 shows the drag polar from OpenVSP, which underestimates drag components compared to SUAVE.

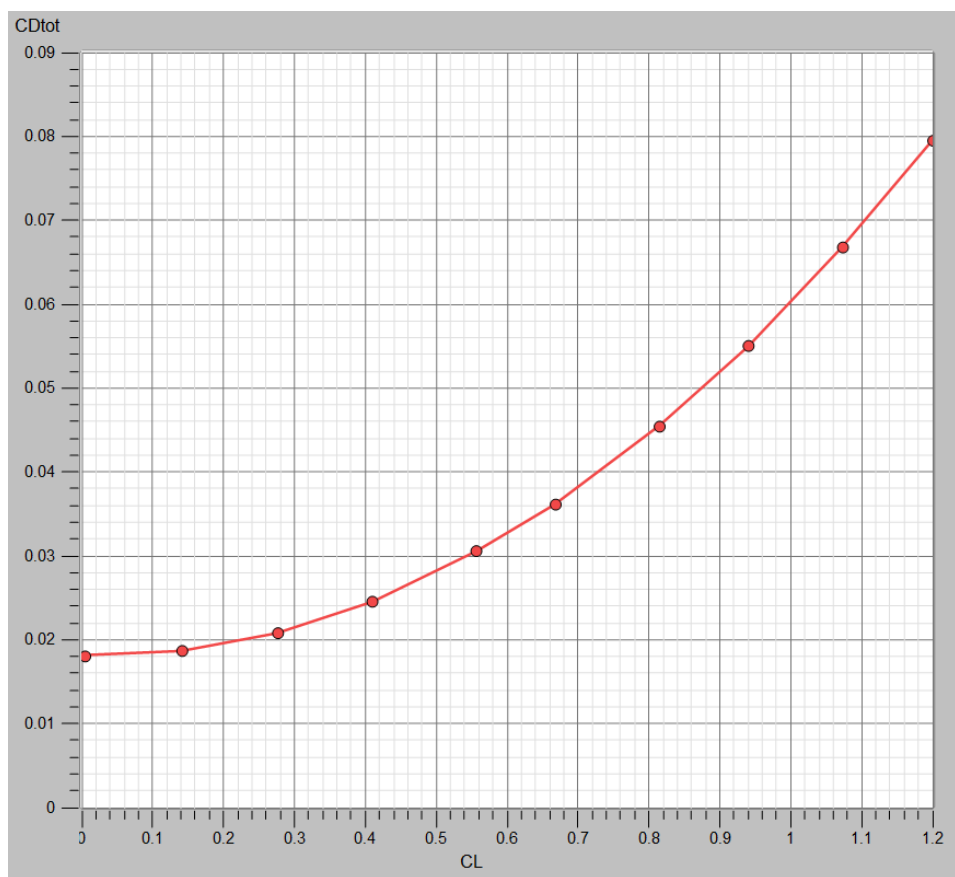


Figure 4.28: OpenVSP Drag Polar using VLM

Chapter 5

VTOL MK2 Mechanical Design

After the design had been finalized in OpenVSP, the model was exported as a STEP file and imported into Siemens NX 2406. From here, a top-down design procedure was implemented, where the model was segmented into individual subassemblies. In NX, the majority of the design was done in a single part file due to the system components being quite interdependent on each other. In the top down process, the individual bodies are linked to individual part files using NX wave linking features. The details of each component are given in the following sections. At the time this paper was written, the mechanical design had not been completed. This report details what work has been done and what is planned for the future to continue the build.

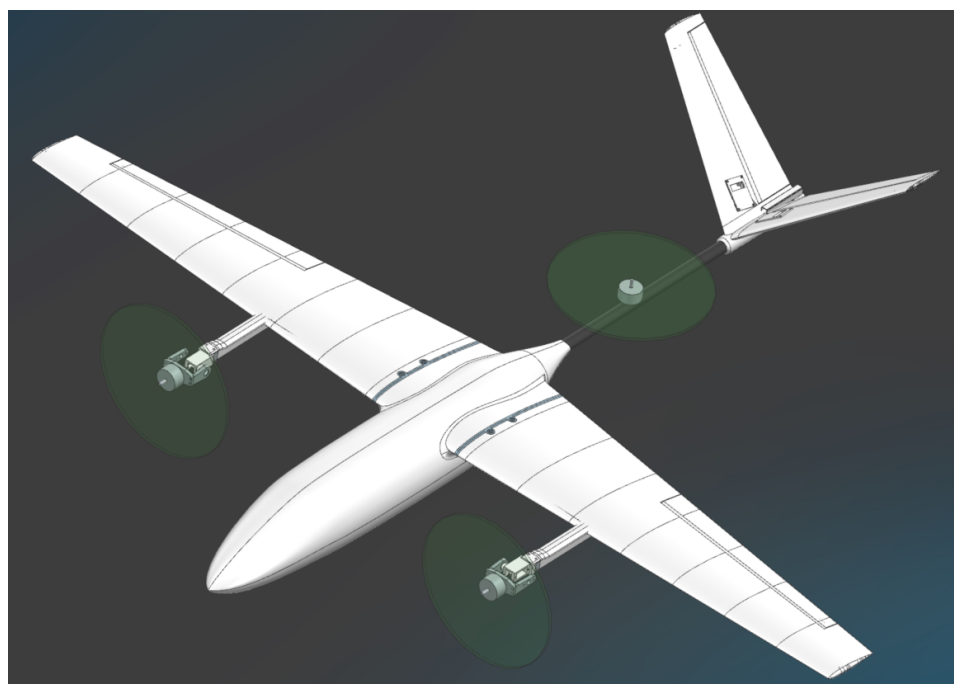


Figure 5.1: Cruise Configuration

5.1 Wing

The main wing was designed with cavities for the spars, control servo, and wires leading into the fuselage. They are detachable for easy transportation,

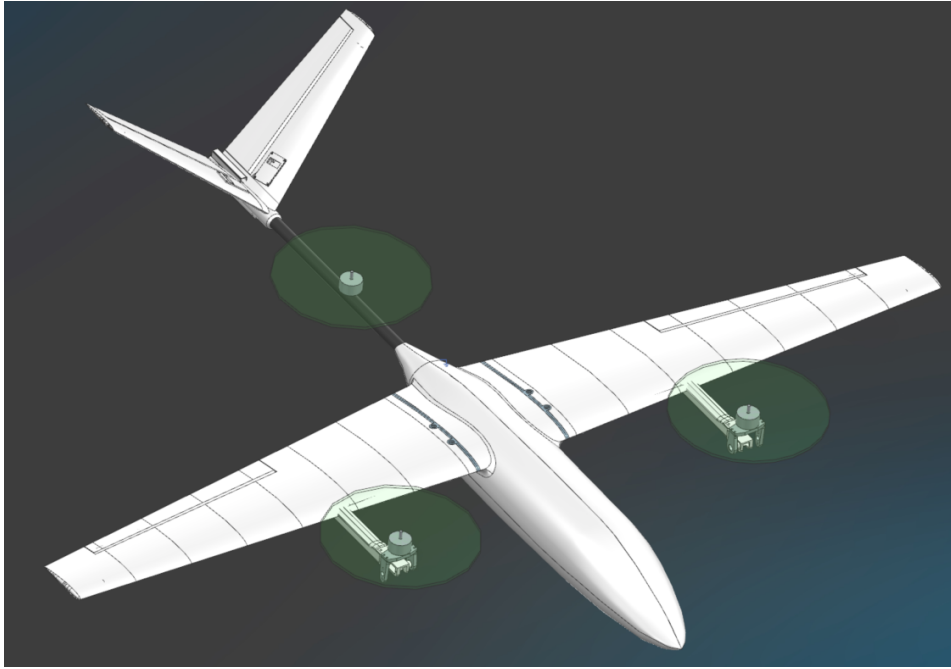


Figure 5.2: Hover Configuration

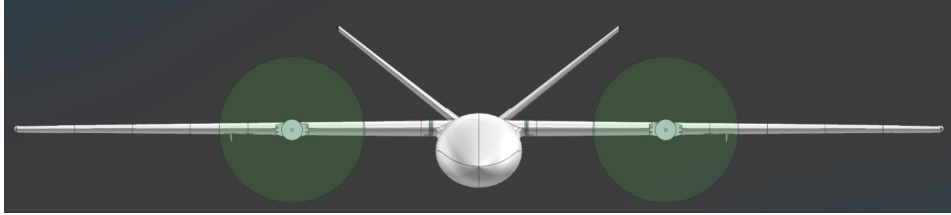


Figure 5.3: Front View Cruise Configuration

and bolts mount it to the fuselage. The tiltrotor booms are printed as singular parts that mount to the wing spars and integrate seamlessly with the remainder of the wing. Figure 5.4 shows the wing and wingbox. The main spar carries the shear and bending load of aerodynamic forces and transfers them to the 3D printed wingbox. The wingbox only supports normal force from the spar and transfers it to the tail boom and fuselage shell (hidden) for reasons specified in the Spar Design section. The wingbox is made of PLA or PETG plastic with sufficient wall layers and infill to support the load and remain rigid. The wings are attached to the fuselage using a coupling designed to be bolted together for easy removal and storage. In Figure 5.5, the wing in white has a gray plate glued onto it, which bolts to the gray plate glued to the fuselage. Because the spar takes the load of aerodynamic forces, this joint is not load bearing and just keeps the wing from sliding off the spar. Figures 5.6 and 5.7 detail this interaction. Cutouts and channels allow wires to pass through the wings for servos and motors.

5.1.1 Tiltrotor Mechanism

At the end of the booms are heat set insert mountings for a servo box that houses the tiltrotor motor. The propulsion motor mounts to a motor plate with side linkages that fix the propulsion motor to the servo motor for precise

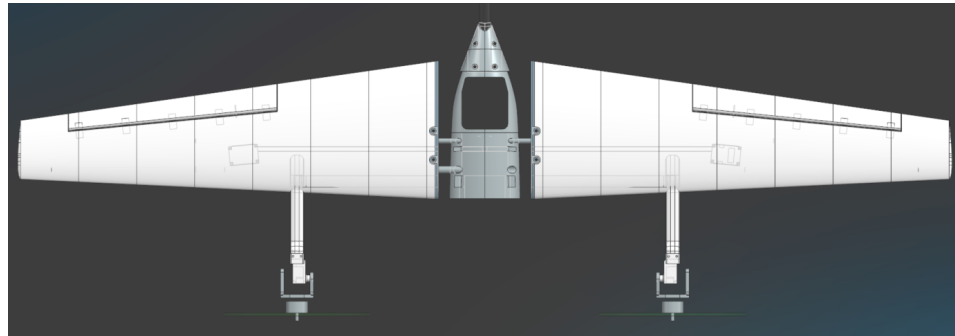


Figure 5.4: Wing CAD Showing Wingbox, Wings, Booms, Tiltrotors, and Ailerons. Fuselage Hidden.

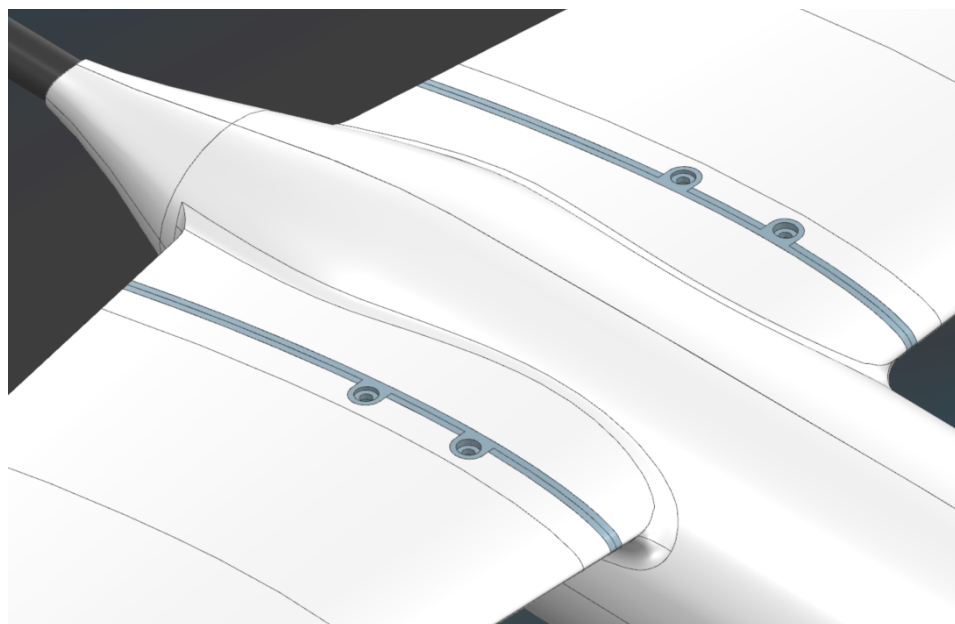


Figure 5.5: Fuselage and Wing Junction.

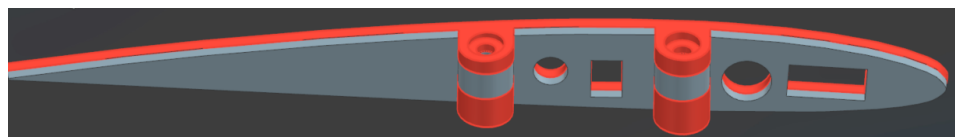


Figure 5.6: Junction Plates Shown, Bolted Together. Nut Pocket holds 10-32 Nut.

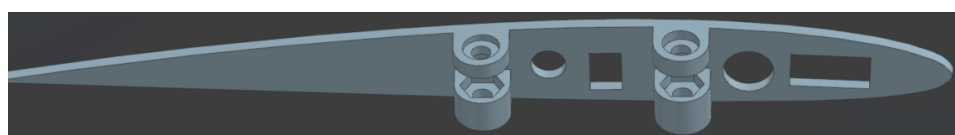


Figure 5.7: PLA or PETG Plate Glued to Fuselage Section, Featuring Nut Pocket.

angular control. A press-fit bearing on one side of the pivot arms combined with the fact that the servo control arm is bolted directly to the other pivot arm produces a fully constrained system that rotates 1:1 with the servo motor. The motor faceplate and side pivot arms are 3D printed separately in their respective print orientations in order to create stronger parts in the direction of loads – printed layers are less likely to shear when they have large area in the plane of the print bed. A wire channel is cut through the boom and wing

to allow the propulsion motor and tilt servo wires to route to the fuselage interior. Figures 5.8 and 5.9 show the tiltrotor mechanism without the servo motor mounted. The close side mounts to the servo horn, while the far side features the bearing. A shoulder bolt is used to fasten the bearing to the servo housing. The tiltrotor assembly is detachable from the boom for print orientation and maintenance reasons using four 4-40 heat set inserts. The booms and tiltrotor mechanisms were designed to allow the rotors to angle 20 degree rearward from vertical. Figure 5.10 shows this clearance, used for yaw control in hover.

The remaining mechanical tasks for the wing are to complete joining parts and sectioning into multiple parts, which is not a complex task.

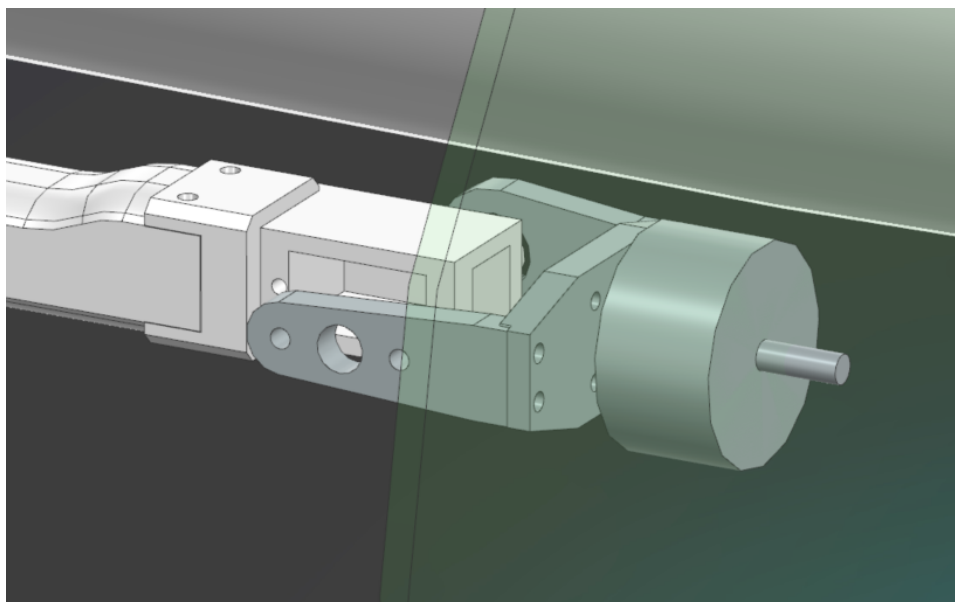


Figure 5.8: Tiltrotor Mechanism Hover Configuration

5.1.2 Spar Design

The main wing spar is a carbon fiber tube designed to take the bending moment in the highest load-factor scenario during normal operation. During a tight turn, the aircraft is expected to turn at a 28m radius, but the requirement was increased to 8.5m to allow for a 3-second full circle sustained turn. This requirement was changed to account for more aggressive pilots handling the aircraft. Here, the load factor is calculated as 3.96 using Equation 2.3.6. The total lift is 116 Newtons under this maneuver.

Assuming a uniform lift distribution for structural reasons is more conservative than the actual lift distribution, which is shifted inboard. Multiple inner and outer diameters were analyzed in a spreadsheet, which changed the moment of inertia and distance from the neutral axis and thus the maximum stress experienced. Another limiting factor was the thickness of the wing, which constrained the spar diameter to less than approximately 12mm. Furthermore, the main spar was not able to reach all the way out to the wingtips since the tips tapered and thus had lower thickness. In the end, a 12mm

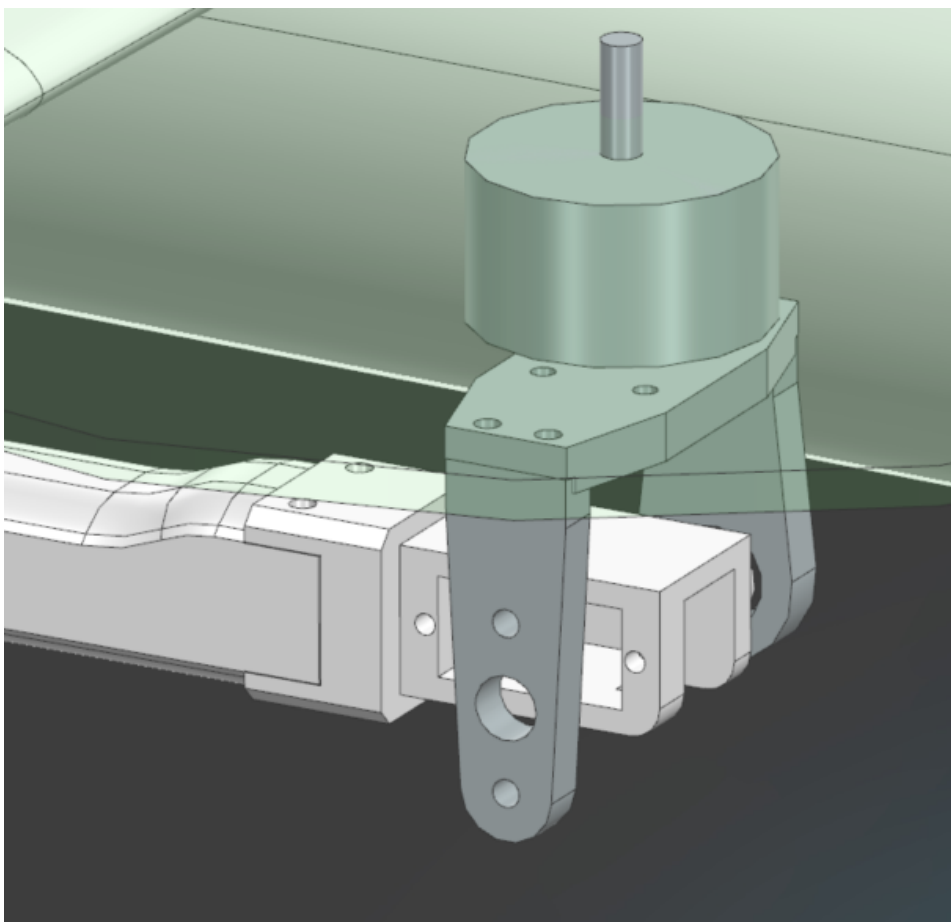


Figure 5.9: Tiltrotor Mechanism Cruise Configuration

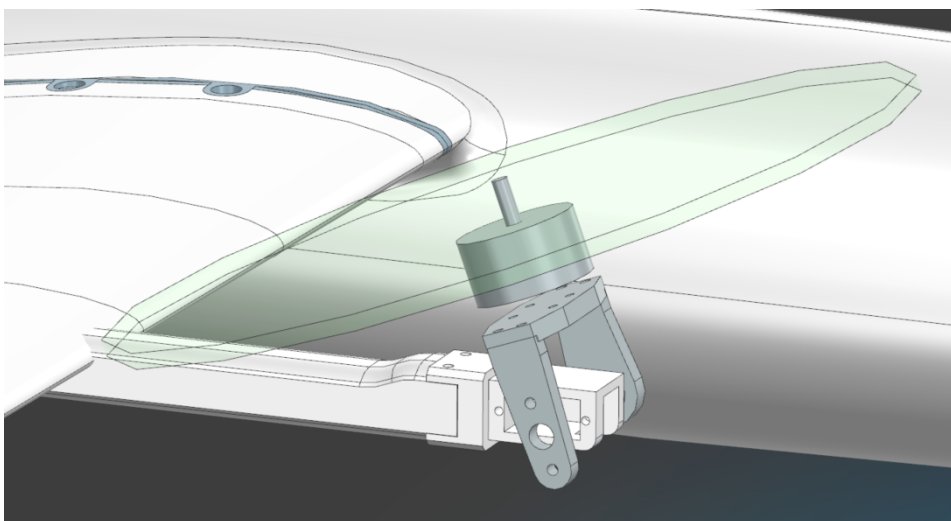


Figure 5.10: Tiltrotors Have 20 deg Rear Clearance

outer diameter and 10mm inner diameter tube was chosen. With a uniform lift distribution, the maximum moment experienced from the spar was 340 MPa tensile stress on the underside and 340 MPa compressive stress on the top side. Since carbon fiber composite is weaker in compression, this stress was compared to the yield stress of the material, which is approximately 517 MPa, for a safety factor of 1.504.

Because online vendors sell lengths of carbon fiber tube limited to 1m, the span of 1.6m would require the spar to be multiple segments. The first option would be to use symmetrical spars, with a joint in the center and no segments

along the wing. This has the disadvantage of requiring a strong junction in the middle where stresses are maximized. A second option was to use a 1m section across the center of the aircraft symmetrically, then add smaller spar sections to support the outboard side of the wings. This method allows for the selection of a smaller outboard spar due to a smaller bending moment. However, the disadvantage is that in order to transfer all loads to the center spar, a junction section of the wing must be able to withstand the load of the transfer. While weight is reduced from a smaller spar on the outboard section of the wing, some weight will be recovered by reinforcing the junction in the region where the inner and outer spar overlap. A third option is to use a "telescoping" spar configuration which is similar to the second option. However, the outboard spar would slide concentrically into the inboard main spar, and a 3D printed coupling would ensure a proper fit. This has the advantage of eliminating the need for a 3D printed junction component to transfer the load to the inner spar. As a result, the third option is lightest and strongest, and so it was selected. To prevent the wing from twisting, a second rear spar is added. Figure 5.11 shows the spar system, with the smaller diameter spar sliding into the larger diameter main spar. There will be a 3D printed insert that ensures a press-fit between the two components.

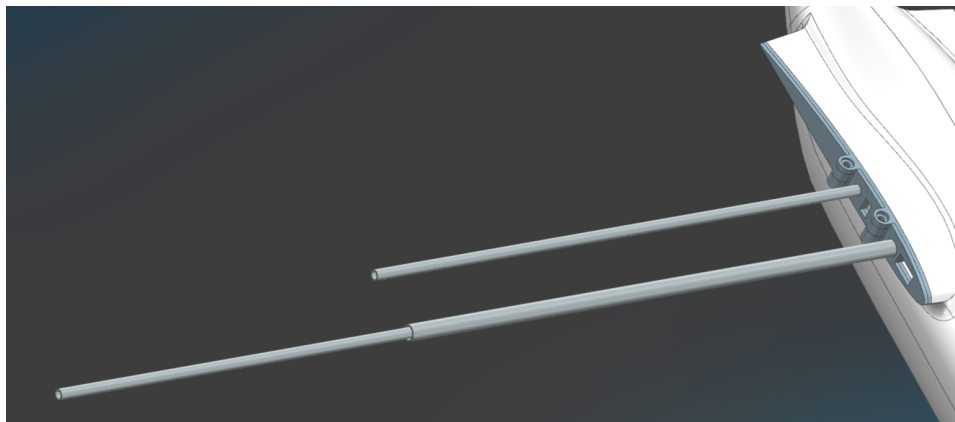


Figure 5.11: Spar Telescoping Configuration

5.2 Fuselage

The fuselage is designed to house the battery and electronics. The load from the wings is transferred to the wingbox, which then distributes the load over the inside of the fuselage and the tail boom. Figure 5.12 shows the wingbox and tail clamp system, which is printed out of high strength PLA. The print is sectioned into three parts, with the forward half split in two for print orientation reasons, and since they transmit normal forces upward to the fuselage, the bond strength is not relevant. The third component is the rear boom clamp with the hole in it as an electronics access hatch. This component is bolted to the front half using heat set inserts and 10-32 bolts. The boom clamp is pictured from the underside in Figure 5.13, where a lower clamshell component

squeezes the boom to retain it. Four bolts through heat set inserts installed from below ensures an extremely strong joint. Loads are transferred through the clamp to the wingbox to maintain rigidity.

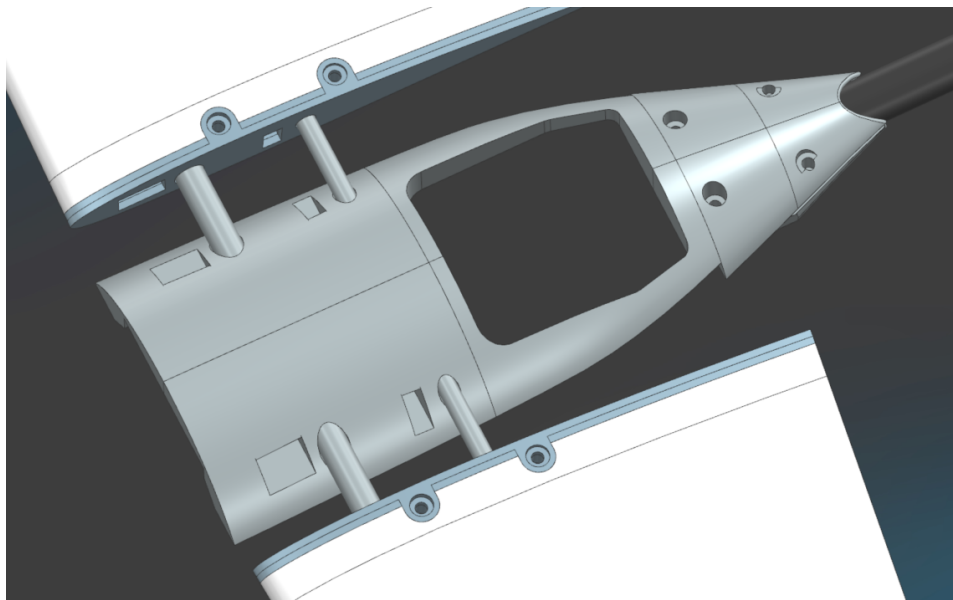


Figure 5.12: Wingbox and Tail Boom Clamp

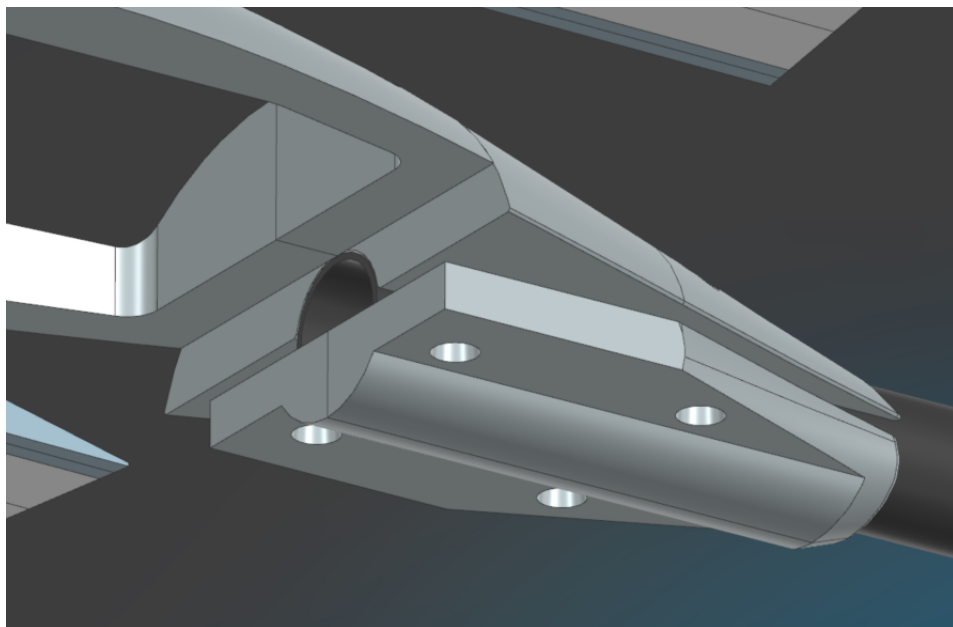


Figure 5.13: Underside of Boom Clamp

The remainder of the fuselage has yet to be sectioned and designed, but access hatches are planned for easy installation of the battery. A battery tray inside will allow for placement of the battery to precisely achieve the correct center of mass for static stability. The rear rotor mounting also has yet to be designed but will be a simple clamping mechanism onto the rear boom. Figure 5.14 shows the fuselage and rear lift rotor. A rear wiring port is shown in Figure 5.15, which allows the rear lift motor wires to pass through into the interior of the fuselage.

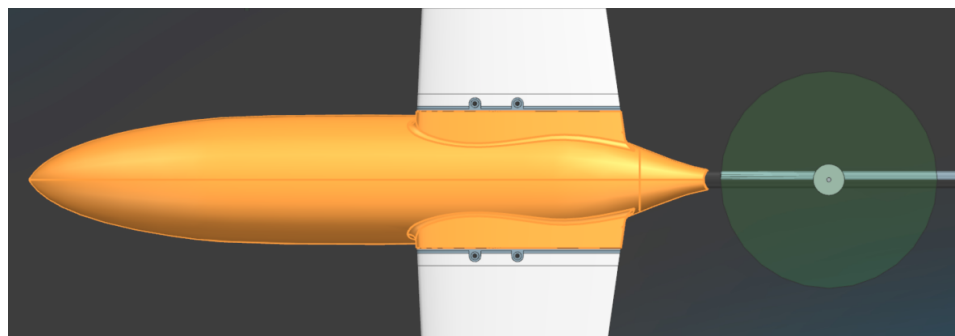


Figure 5.14: Fuselage (Unfinished)

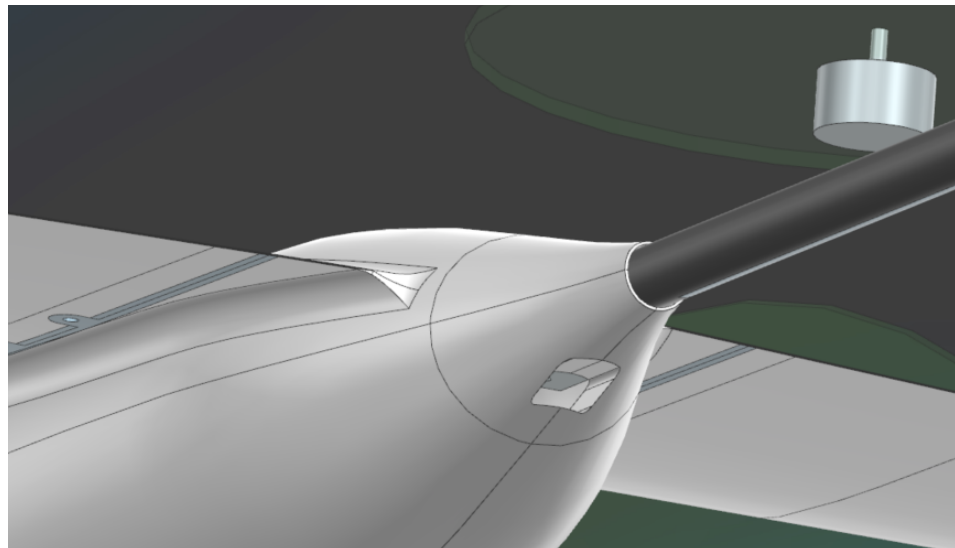


Figure 5.15: Rear Wiring Port

5.3 Tail

The tail mounts to the carbon fiber boom using a clamping mechanism, using bolts to tighten. This provides an easily removable but extremely strong union of the tail to the boom. The tail clamp is visible in Figure 5.16. The tail features two servo motors to control the deflection of the ruddervators, and the linkage arm has yet to be designed. Figure 5.17 shows the tail from the front, top view. Visible is a wiring channel that passes the servo wires into the rear of the carbon fiber boom, allowing them to travel through the boom into the fuselage. The tail is supported by two 6mm OD 4mm ID carbon fiber spars on each side.

5.4 Control Surfaces

The control surfaces were initially sized according to guidelines set by historical examples in Raymer's *Aircraft Design*. Figures 5.18 and 5.19 show Raymer's guidelines. The tail was chosen to have a control surface with 50% chord and almost 90% span of the tail planes. The ailerons were chosen as 25% chord and 40% span. They mount to the outboard of the wings to improve the moment induced by deflection. Mechanically, control surfaces were mounted using nylon hinges commonly found in the RC aircraft community, bonded

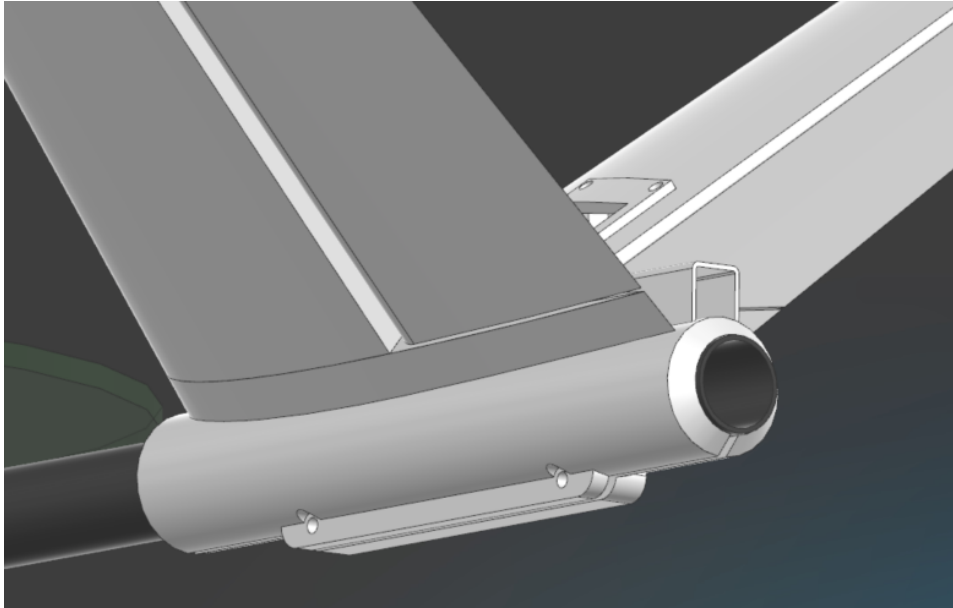


Figure 5.16: Tail Clamp

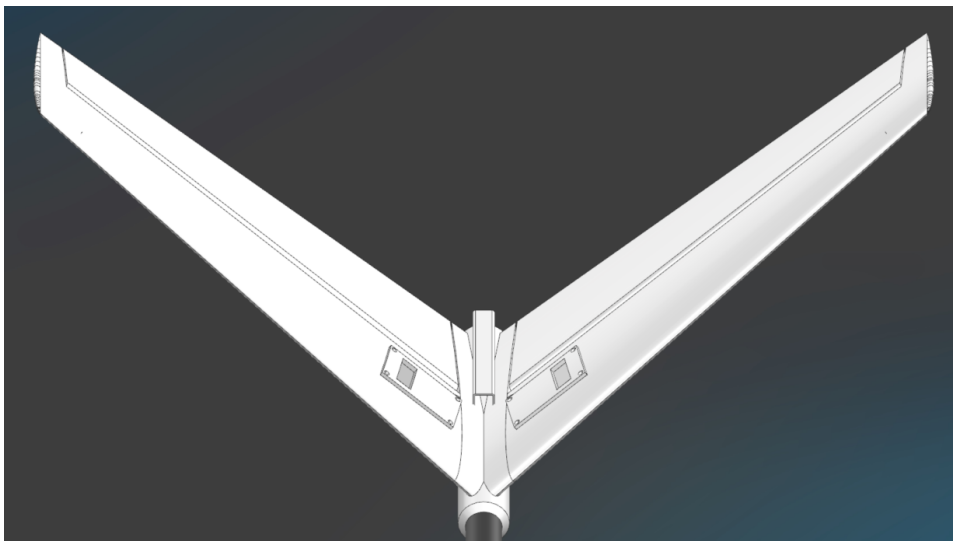


Figure 5.17: Tail Top View

into slots designed into the wing, tail, and control surfaces. Servo motors drive the control surface deflection. For a 1:1 deflection angle, a parallel four-bar is employed, such as the aileron shown in Figure 5.20. The servo motors are bolted to a cover that bolts into the servo box using heat set inserts, also in the same figure.

While detailed dynamic analysis was out of the scope of this one semester project, OpenVSP was used to analyze the moments created by the control surfaces at different deflections. Mass properties were also assigned to the aircraft to get an estimate of the moments of inertia. Table 5.4 shows the ruddervator deflection results. From here, a 120 deg/s pitch rate can be achieved in 50 ms by deflecting the ruddervators by 20 degrees. Table 5.4 shows results of the aileron deflections. Here, a 120 deg/s roll rate is achieved in 50ms using a 25 degree deflection.

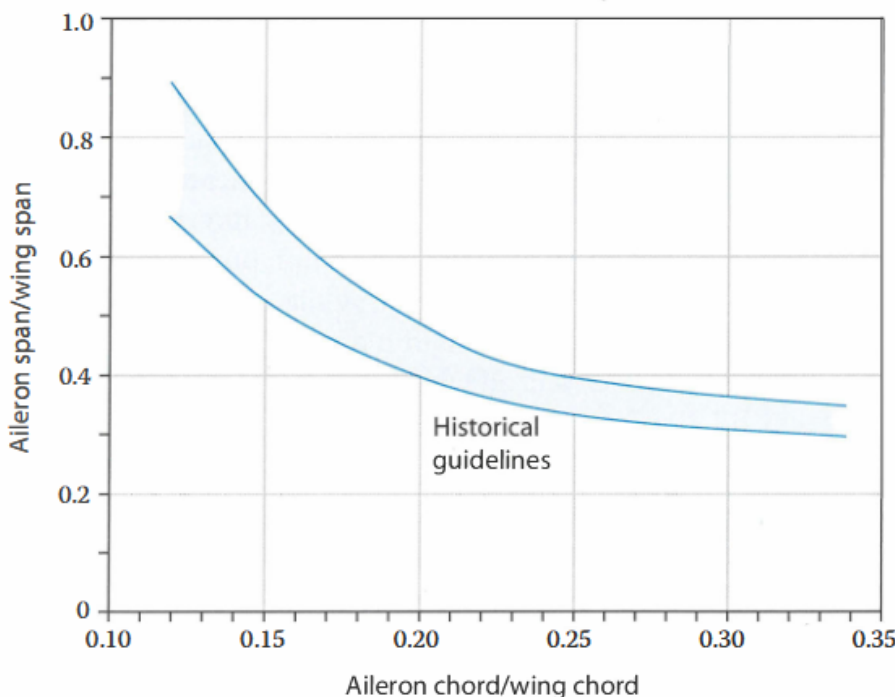


Figure 5.18: Aileron Sizing from Raymer's *Aircraft Design*, Figure 6.3 [4]

| Aircraft | Elevator C_e/C | Rudder C_r/C |
|----------------|------------------|----------------|
| Fighter/attack | 0.30* | 0.30 |
| Jet transport | 0.25† | 0.32 |
| Jet trainer | 0.35 | 0.35 |
| Biz jet | 0.32† | 0.30 |
| GA single | 0.45 | 0.40 |
| GA twin | 0.36 | 0.46 |
| Sailplane | 0.43 | 0.40 |

Figure 5.19: Tail Control Surface Sizing from Raymer's *Aircraft Design*, Table 6.3 [4]

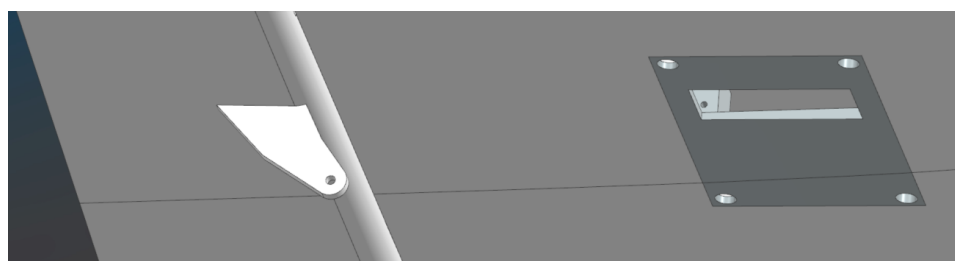


Figure 5.20: Aileron Horn and Servo Cover

5.5 Avionics

Avionics were not the primary focus of this project. The chosen components for the control of the aircraft were the SpeedyBee F405 WING APP Fixed Wing Flight Controller, the SpeedyBee BLS 60A 30x30 4-in-1 ESC, a RadioMaster

Table 5.1: Ruddervator Deflection and Resulting Pitch Angular Acceleration

| Ruddervator Deflection (deg) | C_{my} at 0 α | Moment (Nm) | $\ddot{\theta}$ (rad/s ²) |
|------------------------------|------------------------|-------------|---------------------------------------|
| 30 | 1.036 | 10.80 | 56.84 |
| 20 | 0.767 | 8.00 | 42.08 |
| 10 | 0.416 | 4.34 | 22.82 |
| 0 | 0.02 | 0.21 | 1.10 |
| -10 | -0.377 | -3.93 | -20.68 |
| -20 | -0.723 | -7.54 | -39.67 |
| -30 | -0.988 | -10.30 | -54.21 |

Table 5.2: Aileron Deflection and Resulting Roll Angular Acceleration

| Aileron Deflection | C_{mx} at 0 α | Moment (Nm) | $\ddot{\theta}$ (rad/s ²) |
|--------------------|------------------------|-------------|---------------------------------------|
| 0 | 0 | 0.00 | 0.00 |
| 10 | 0.062 | 5.48 | 39.13 |
| 20 | 0.116 | 10.25 | 73.22 |
| 30 | 0.158 | 13.96 | 99.73 |

Boxer transmitter, and RadioMaster RP3 ELRC Receiver. These components were chosen based on their ability to support modern control protocols and firmware. The flight controller is capable of running ArduPilot, which has a VTOL configuration control framework built in. The full bill of materials can be observed in Appendix A.

Chapter 6

Conclusion

In conclusion, the VTOL MK2 aircraft represents an extremely valuable learning process for the author. Compared to a previous aircraft design, this UAV represents a greater depth of analysis and a stronger engineering justification for the parameters selected. With applications ranging widely from search and rescue to reconnaissance, and more, this platform was designed to be versatile, low cost, and easy to build.

Throughout the design process, new software and skills like SUAVE, OpenAeroStruct, and XFLR enabled the author to learn more about designing a system with many design variables and a complex design space.

One point worth mentioning is the significant time dedicated to the non-linear process of what can only be described as "playing" with the aircraft parameters to get a better sense of what the design space looks like. With the tools available at hand, significant learning and understanding was gained from simply getting things to work, messing with details, and recording vast amounts of data that largely wasn't even put in the report. This project is just the beginning of my aircraft design journey, and it has enabled my excitement and passion for aircraft to transform into a productive engineering process. Many hours were dedicated each week to this project, which often took precedence over required coursework since it was fun, engaging, and felt like learning at a much faster rate than an ordinary class.

6.1 Future Work

Future work on the conventional aircraft configuration at hand would be to finish the mechanical design including the following features: battery tray for adjustable CG, electronics and avionics mounting, sectioning and joining methods for 3D printing, manufacturing, and assembly. Furthermore, dynamic stability analysis could be run using code produced for an Aircraft Dynamics class that would show the aircraft response to eigenmode perturbations from equilibrium using derivatives obtained from OpenVSP.

While the blended wing body aircraft was not the focus of this project,

it showed great potential to outperform the conventional approach taken this semester. In the next iteration of VTOL aircraft, the author plans to implement a BWB aircraft, trading ease of control and stability for increased efficiency. The concept that would satisfy the mission requirements would feature large elevons on each wing and a small vertical stabilizer. One large tractor propeller on each wing would produce thrust over the elevons and allow for hover control by thrust vectoring using the elevons. With this concept, the BWB would be a tailsitter VTOL. Figures 6.1, 6.2, 6.3, and 6.4 show the BWB concept. Note that the entire aircraft utilizes a reflexed Eppler 325 airfoil to reduce pitch-down moment at the C_L required. The fuselage was thickened to 20% chord, and it was sized to accommodate the same desired payload and battery volume as the fuselage of the conventional configuration. The fuselage in this case is a lifting body and thus raises the efficiency of the aircraft and reduces the parasitic drag. Analysis on stability has yet to be completed, but a swept wing produces greater static margin, as it shifts the neutral point rearward.

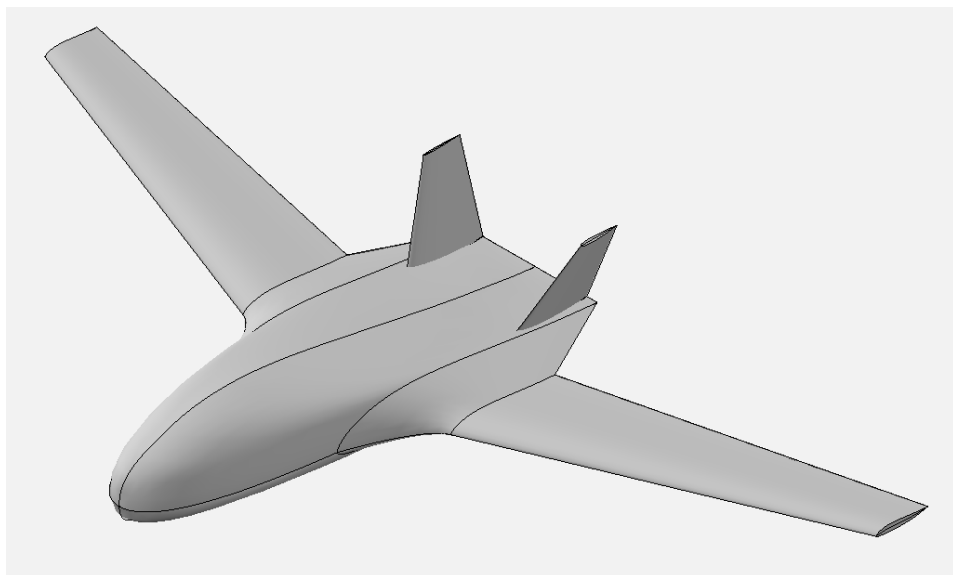


Figure 6.1: BWB Concept

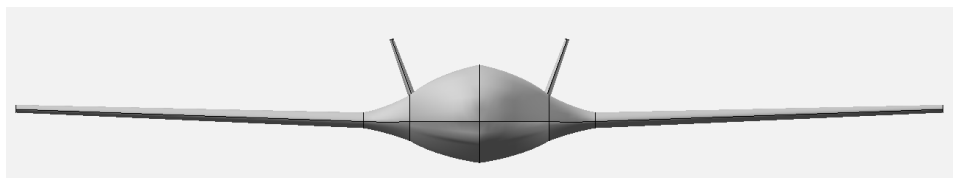


Figure 6.2: BWB Concept Front

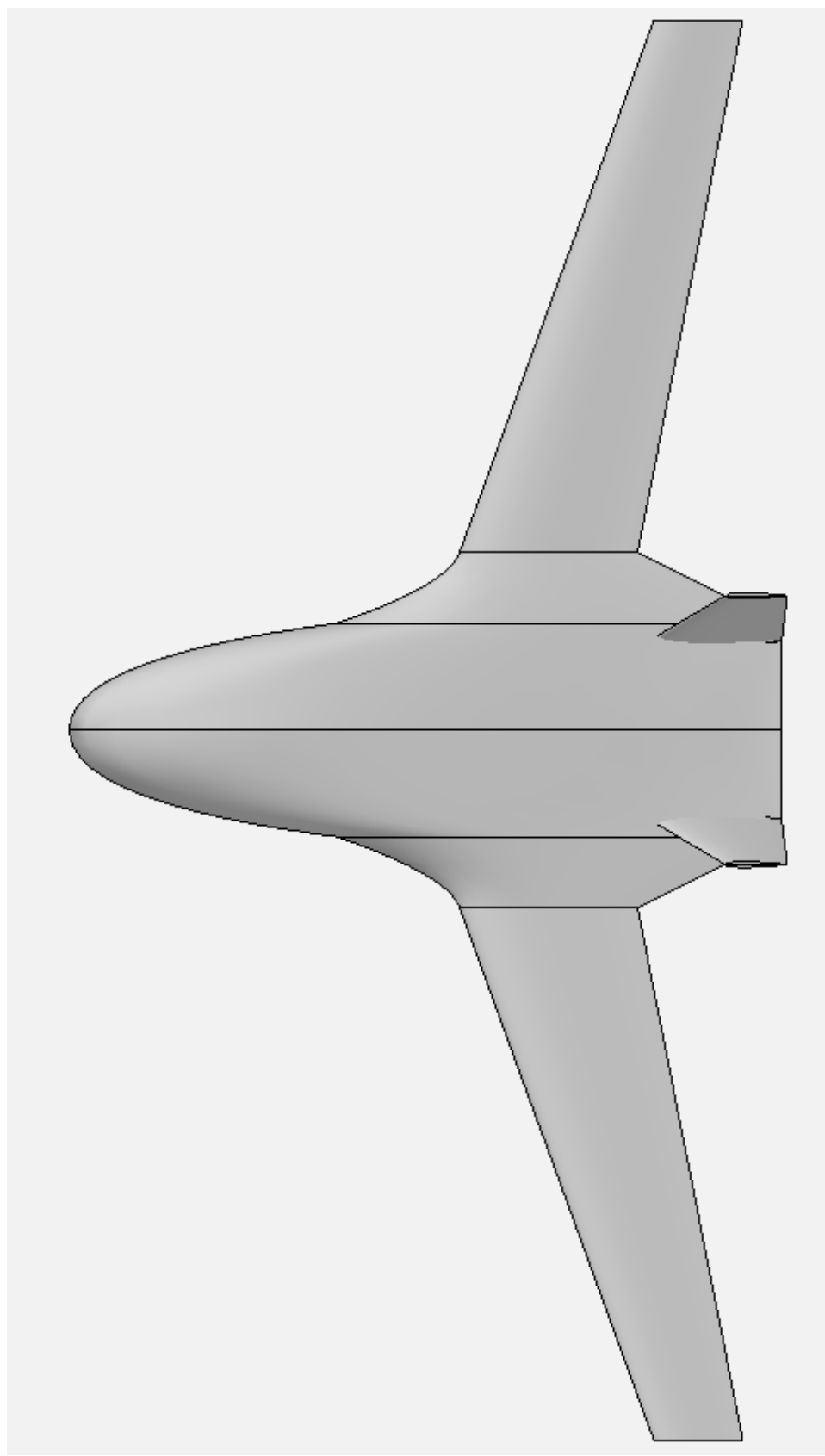


Figure 6.3: BWB Concept Top

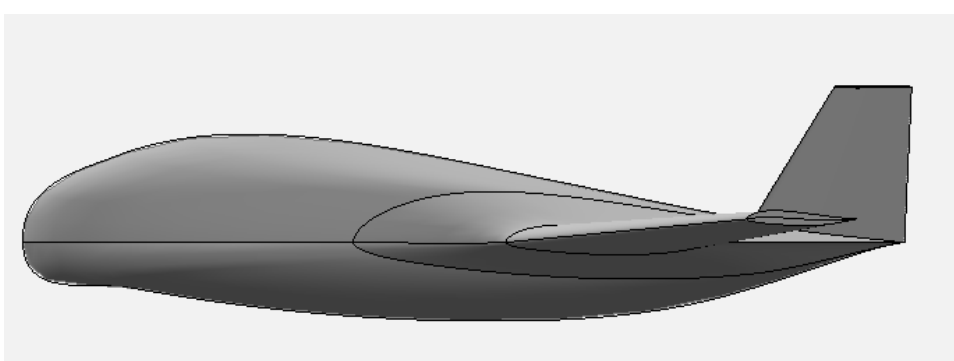


Figure 6.4: BWB Concept Side

Bibliography

- [1] Bill Drury Austin Hughes. *Electric Motors and Drives, 5th Edition.* Newnes, 2019.
- [2] G.K. Ananda O.D. Dantsker J.B. Brandt, R.W. Deters and M.S. Selig. Uiuc propeller database. Vols 1-4, University of Illinois at Urbana-Champaign, Department of Aerospace Engineering, retrieved from <https://m-selig.ae.illinois.edu/props/propDB.html.>, 2008.
- [3] Rajmohan Waghela Ryan Callahan Aaron Watson Lance W. Traub, Emilio Botero. Effect of taper ratio at low reynolds number. *Aerospace Research Central*, 52(2):734–747, 2015.
- [4] Daniel P. Raymer. *Aircraft Design: A Conceptual Approach, 6th Edition.* American Institute of Aeronautics and Astronautics, 2018.
- [5] Michael S. Selig. Low reynolds number airfoil design lecture notes. VKI Lecture Series Sponsored by NATO Research and Technology Organization, 2003.

Appendix A

Code and Models can be found in Github:

https://github.com/Buird/Liou_MAE_IW_Spr_2025

Below is the complete bill of materials for the build.

| Item Description | SPECIAL NOTES | URL | # | Unit Cost | # | Quantity | # | Item Cost | Total Cost |
|---|--------------------------|---|---|-----------|---|----------|---|-----------|------------|
| Lightweight Foaming PLA 3D printer Filament | | https://colorfabb.us/lw-pla-natural | | 36.29 | | 2 | | 72.58 | 739.19 |
| 10x10E | | https://www.apcprop.com/product/10x10e/ | | 3.64 | | 2 | | 7.28 | |
| 10x10EP | | https://www.apcprop.com/product/10x10ep/ | | 3.64 | | 1 | | 3.64 | |
| BrotherHobby Avenger 3110 730KV/900KV Motor(CW) | Select 730KV option | https://www.brotherhobbystore.com/products/brotherhobby-avenger-3110-730kv-900kv-motorcw-116 | | 33.99 | | 3 | | 101.97 | |
| 1-8S Lipo Battery Voltage Tester / Low Voltage Buzzer Alarm | | https://www.getfpv.com/1-8s-lipo-battery-voltage-tester-low-voltage-buzzer-alarm.html | | 3.99 | | 1 | | 3.99 | |
| 3.5mm Gold "Bullet" Connectors (12 Pair) | | https://www.getfpv.com/3-5mm-gold-bullet-connectors-12-pair.html | | 3.29 | | 1 | | 3.29 | |
| XT90 Lipo Pigtail Connection 10AWG (2pcs) | | https://www.getfpv.com/xt90-lipo-pigtail-connection-10awg-2pcs.html | | 5.49 | | 1 | | 5.49 | |
| RDQ Series 22.8V 6S 6500mAh 70C LiHV Battery - XT90 | | https://www.racedayquads.com/collections/6s-batteries/products/rdq-series-22-8v-6s-6500mah-70c-lihv-battery-xt90 | | 144.99 | | 1 | | 144.99 | |
| SpeedyBee BLS 60A 30x30 4-in-1 ESC | | https://www.speedybee.com/speedybee-bls-60a-30x30-4-in-1-esc/ | | 46.99 | | 1 | | 46.99 | |
| SpeedyBee F405 WING APP Fixed Wing Flight Controller | | https://www.speedybee.com/speedybee-f405-wing-app-fixed-wing-flight-controller/ | | 39.99 | | 1 | | 39.99 | |
| Tiltrotor Servos | | https://www.emax-usa.com/collections/servos/products/es3054hv-high-voltage-servo# | | 13.99 | | 2 | | 27.98 | |
| battery for transmitter | | https://www.amazon.com/PAOWANG-Rechargeable-Batteries-Flashlights-Headlamps/dp/B0CW5LFZ1J?refid=3815P20PTXL9F&dib=eyJ2ljojMSJ9.2-6uPbpeoSVcPisNw9XjVFbR3EEQJ8tfScN0MF1vATHJshqHekNe04KB1z0ZAfEJ-6G7H7JLWSe4CztGYDD46yJCDbf3ccqaHxJCgPx_Frnkzt3G79rbapsxreb_bXdMcojZmfWCnXTm0jc8LVSVKIPR2qjVnN-L6d-aJMd5aCCQJNvhfjhWcMoVlLI61V9SER22MTY7Xm-gx94zUt8xtgT0RsL3JR-goibQf0xQ5PNX5cmsShlTyz-0KuSbfBCnsLJvh7Fmm1-Ab1F906gJHWg5gHLoSboLPkaLjhA | | 9.99 | | 1 | | 9.99 | |
| Boxer Radio Transmitter | Select ELRS version, FCI | https://www.radiomasterrc.com/products/boxer-radio-controller-m2 | | 139.99 | | 1 | | 139.99 | |
| RP3 ELRS Receiver | | https://www.radiomasterrc.com/products/rp3-expresslrs-2-4ghz-nano-receiver?pr_prod_strat=jac&pr_rec_id=d7e102a61&pr_rec_pid=8195396272359&pr_ref_pid=8255588172007&pr_seq=niform | | 19.99 | | 1 | | 19.99 | |

| Item Description | SPECIAL NOTES | URL | # | Unit Cost | # | Quantity | # | Item Cost | Total Cost |
|-------------------------------------|---------------|---|---|-----------|---|----------|---|-----------|------------|
| 20x18mm rear boom carbon fiber tube | | https://www.amazon.com/KARBXON-Carbon-1000mm-Lightweight-Strength/dp/B09Q8513TH?crid=2OX8L9K4V9WCJ&idb=eyJ2ljoiMSJ9.tnyUu4pRWJpbF66FNgGRDh-LyQtvcAH8vG_uu5Z5AK00G_Miq2uMPsjC22P7o3sRcoR0lp5n-QstOromRwtLyMbVdvyM1b-Q0S4LRNCA2lmFgwSVfk1OoSHEknA7gHuoU-gghVf9ozeWqxCqMRMVyT5bzx0tDz49la0DjNEn8neeuojSytdB-PBdf5BnF7HuleAkncCYW_vleSAOBc6AyxXWLvx9bTaqlkhUs_OJp8uWbDrm-IMfepgVJ_dPfey9-UTUKsT4RP1GRyrmk&idb_tag=se&keywodws=20mm%2Bx%2B18mm%2Bx%2B750mm%2Bcarbon%2Bfiber%2Btube%2Caps%2C85&sr=8-1&th=1 | | 31.96 | | 1 | | | 31.96 |
| 12x10mm carbon fiber spar tube | | https://www.amazon.com/Abester-1000mm-Surface-Carbon-Fiber/dp/B078WRL57Q | | 10.77 | | 1 | | 10.77 | |
| Control Surface Servos | | https://emax-usa.com/collections/servos/products/es3059md-12g-digital-metal-gear-servo# | | 6.99 | | 4 | | 27.96 | |
| 6x4mm secondary carbon fiber tube | | https://www.amazon.com/KARBXON-Carbon-Pultruded-Planes-Drones-Projects/dp/B09Q88ZDY6?crid=38FNS9K8U09PW&idb=eyJ2ljoiMSJ9.35B-2kdZk3_1wgJ_X_rXRY2ZX0re8d53YX-xF8Fit_wJv8B5fla7qAEif31jB-gkawD3DryOShsISRd4Jwms5pbVs0Srnn6E04-RpsH41VVsVqauxG3laX9_YxW8MisBZBmwyUhjzwr2E4-B6_o8almK5juuntnmrqxmx60NmDEwOhJkJzqZnnirhTNbJQQTmgxKSBlsFCAOOn1np2xiQu-NBspX3pavCoZeyWSLpl_E57CKH09flkJzhf8EfWfFzizwKB85bzKz9WO44Qu_T0cs&idb_tag=se&keywodrs=8x6x1000%2Bcarbon%2Bfiber%2Btube&idb=1744147535&sprefix=8x6x1000%2Bcarbon%2Bfiber%2Btube%2Caps%2C118&sr=8-14&th=1 | | 29.96 | | 1 | | 29.96 | |
| Pushrods | | https://www.amazon.com/Adjustable-Pushrod-Connector-Airplane-Aircraft/dp/B086C4Q5RS?crid=1T9U6PHXCCEU4&idb=eyJ2ljoiMSJ9.igV2sdylhGdvUPobgJVJegSLjJAUk18coLAjxe3l_H4CG5NmzxOG-SI9Y0E0gSOAkU0mlJzrrKeWJyIKJvl ezM6cRb8OSKmtlUljiyldCjEfxr-lgefAxuyqg9-ErnceboUcMw9ZDUnm9mxiz_MV0j-cFuWjbOs7T4MeNyfIIN9ijVvoXuAS- fa4tUtSEMiMii5RAxpYicMiH0h_9_FUg7dpyK2F7Yx41Atd0b4WzqopPK9i4DNqHRxUIJuWWNBwezI980kD8e-SswlQYt5kk2zBQDQ6vqyu_wBEPJE d-1Q-JvbZ5xluyIRcakSl0k6EjtkDO_9wPyC qypD6x3eXUJ8&idb_tag=se&keywor ds=rc+aircraft+pushrod&idb=1744596615&sprefix=rc+aircraft+pushrod%2Caps%2C172&sr=8-8 | | 10.38 | | 1 | | 10.38 | |